GREEN SYNTHESIS OF REDUCED GRAPHENE OXIDE FOR EFFICIENT ADSORPTION-PHOTOCATALYSIS STUDIES IN METHYLENE BLUE DYE DEGRADATION

VALERIE SIONG LING ER

INSTITUTE FOR ADVANCED STUDIES
UNIVERSITY OF MALAYA
KUALA LUMPUR

2020

GREEN SYNTHESIS OF REDUCED GRAPHENE OXIDE FOR EFFICIENT ADSORPTION-PHOTOCATALYSIS STUDIES IN METHYLENE BLUE DYE DEGRADATION

VALERIE SIONG LING ER

DISSERTATION SUBMITTED IN FULFILMENT OF
THE REQUIREMENTS FOR THE DEGREE OF MASTER
OF PHILOSOPHY

INSTITUTE FOR ADVANCED STUDIES
UNIVERSITY OF MALAYA
KUALA LUMPUR

2020

UNIVERSITY OF MALAYA
ORIGINAL LITERARY WORK DECLARATION

Name of Candidate: Valerie Siong Ling Er

Matric No: HGA 150019

Name of Degree: Master of Philosophy

Title of Dissertation: Green Synthesis of Reduced Graphene Oxide for Efficient Adsorption-Photocatalysis Studies in Methylene Blue Dye Degradation

Field of Study: Chemistry (Analytical Chemistry)

I do solemnly and sincerely declare that:

(1) I am the sole author/writer of this Work;
(2) This Work is original;
(3) Any use of any work in which copyright exists was done by way of fair dealing and for permitted purposes and any excerpt or extract from, or reference to or reproduction of any copyright work has been disclosed expressly and sufficiently and the title of the Work and its authorship have been acknowledged in this Work;
(4) I do not have any actual knowledge nor do I ought reasonably to know that the making of this work constitutes an infringement of any copyright work;
(5) I hereby assign all and every rights in the copyright to this Work to the University of Malaya ("UM"), who henceforth shall be owner of the copyright in this Work and that any reproduction or use in any form or by any means whatsoever is prohibited without the written consent of UM having been first had and obtained;
(6) I am fully aware that if in the course of making this Work I have infringed any copyright whether intentionally or otherwise, I may be subject to legal action or any other action as may be determined by UM.

Candidate's Signature Date: 12.5.2020

Subscribed and solemnly declared before,

Witness's Signature Date: 13.5.2020

Name:

Designation:

GREEN SYNTHESIS OF REDUCED GRAPHENE OXIDE FOR EFFICIENT ADSORPTION-PHOTOCATALYSIS STUDIES IN METHYLENE BLUE DYE DEGRADATION

ABSTRACT

Dyes are one of the major components of industrial effluents. Owing to the complex structures of these toxic organic compounds, the removal of dyes from effluents possesses a great challenge in wastewater treatment. In order to tackle this issue, one of the effective methods is to remove dyes via the combination of adsorption and photocatalysis processes. In the present work, reduced graphene oxide (rGO) was fabricated from graphene oxide (GO) by using an environmentally friendly solvothermal approach, whereby ethanol was employed as a non-toxic reductant. In order to investigate the formation of rGO, the reduction of GO was carried out at different reduction temperatures and durations. It was found that GO was successfully reduced at an optimum temperature of 160 °C and an optimum duration of 2 hours. This was due to the partial restoration of sp^2 carbon network brought about by the elimination of oxygen functionalities from the surface. With an increase in surface area and a band gap reduction, the rGO-160_2 sample was able to achieve the best adsorption (29.26%) and photoactivity (32.68%) towards the removal of methylene blue (MB) dye. The effects of catalyst dosage, initial concentration of dye, light intensity, and pH of solution were also evaluated against the performance of rGO-160_2. The results demonstrated that an even higher MB removal by adsorption (87.39%) and photodegradation (98.57%) was successfully achieved when 60 mg of rGO-160_2, double 95 W UV lamp, and initial dye solution of 50 ppm at pH = 11 were implemented as the operational conditions. The MB photodegradation efficiency of rGO-160_2 was still maintained at more than 90% after five successive cycles, proving its good stability and recycling ability. This study provides a high-performance adsorbent-cum-photocatalyst for the decontamination of dyes from wastewater.

Keywords: Metal-free catalysis, dye removal, UV light irradiation, wastewater treatment

SINTESIS GRAFIN OKSIDA TERTURUN SECARA MESRA ALAM UNTUK KAJIAN PENJERAPAN-FOTOPEMANGKINAN YANG CEKAP DALAM DEGRADASI PEWARNA METILENA BIRU

ABSTRAK

Bahan-bahan pewarna merupakan salah satu komponen utama efluen perindustrian. Penyingkirannya merupakan satu cabaran yang besar dalam proses rawatan air kumbahan kerana mereka menpunyai struktur yang rumit. Bagi menangani masalah ini, salah satu cara berkesan adalah melalui gabungan proses penjerapan dan fotopemangkinan. Dalam kajian ini, grafin oksida terturun (rGO) telah diperolehi daripada grafin oksida (GO) menggunakan kaedah solvoterma mesra alam, di mana etanol digunakan sebagai agen penurunan yang tidak bertoksik. Penurunan GO telah dijalankan pada suhu dan tempoh yang berbeza untuk menyiasat pembentukan rGO. Pada suhu (160 °C) dan tempoh (2 jam) optimum, GO telah berjaya diturun. Hal ini dikaitkan dengan pemulihan separa rangkaian karbon sp^2 berikutan penyingkiran kumpulan-kumpulan berfungsi dari permukaan. Dengan peningkatan luas permukaan dan pengurangan jurang tenaga, rGO-160_2 berupaya untuk mencapai penjerapan (29.26%) dan aktiviti fotopemangkinan (32.68%) yang terbaik dalam proses penyingkiran pewarna metilena biru (MB). Selain itu, kesan-kesan dos pemangkin, kepekatan awal pewarna, keamatan cahaya, dan pH larutan terhadap prestasi rGO-160_2 juga dinilai. Hasil-hasil kajian menunjukkan bahawa penjerapan (87.39%) dan fotodegradasi (98.57%) MB yang lebih tinggi berjaya dicapai apabila rGO-160_2 sebanyak 60 mg, dua lampu UV 95 W, dan larutan pewarna awal sebanyak 50 ppm pada pH = 11 ditetapkan sebagai syarat-syarat pengoperasian. Kecekapan fotodegradasi MB masih dikekalkan pada 90% dan ke atas selepas lima kitaran berturut-turut. Hal ini telah membuktikan bahawa rGO-160_2 mempunyai kestabilan dan kebolehgunaan semula yang baik. Kajian ini menyediakan penjerap dan fotopemangkin berprestasi tinggi untuk penyingkiran bahan-bahan pewarna dari air kumbahan.

Kata kunci: Pemangkinan bebas logam, penyingkiran bahan-bahan pewarna, sinaran cahaya UV, rawatan air kumbahan

ACKNOWLEDGEMENTS

First and foremost, I would like to thank University of Malaya (UM), Institute for Advanced Studies (IAS), as well as Nanotechnology and Catalysis Research Centre (NANOCAT) for allowing me to finish my Master's study under such a conducive working environment with adequate facilities and equipment.

I would also like to express my sincere appreciation to my supervisors, Ir. Dr. Lai Chin Wei, Associate Prof. Dr. Juan Joon Ching, and Dr. Khe Cheng Seong for their great assistance, professionalism, valuable guidance, and overall supervision throughout this study. It is their immeasurable support along the process that enables me to complete this thesis successfully.

My wholehearted thanks go to Dr. Lee Kian Mun as well, who has tirelessly assisted and guided me throughout my research work, apart from providing me with brilliant technical advices. I would also like to show my gratitude towards my colleagues, especially Tai Xin Hong for contributing and sharing their valuable ideas, opinions and suggestions to me. Many thanks to Dr. Shahid Mehmood for helping me in my Raman analysis, as well as my fellow friends for giving me extra moral supports when I need them the most.

Last but not least, I would also love to express my utmost appreciation to my parents, who have constantly provided me with unfailing supports and continuous encouragements throughout this whole period of researching and writing this thesis. Also, my sincere thanks go to my sisters as well for always supporting and believing in me. Without them, I would have never been able to reach the end of my Master's journey.

TABLE OF CONTENTS

LIST OF FIGURES

LIST OF TABLES

LIST OF SYMBOLS AND ABBREVIATIONS

$\bullet O_2^-$: Superoxide radical

$\bullet OH$: Hydroxyl radical

4-CP : 4-Chlorophenol

$AgNO_3$: Silver nitrate

AOP : Advanced oxidation process

BET : Brunauer-Emmett-Teller

BJH : Barrett-Joyner-Halenda

$C=O$: Carbonyl

C_2H_5OH : Ethanol

CB : Conduction band

CeO_2 : Cerium(IV) oxide

CNT : Carbon nanotube

CO_2 : Carbon dioxide

$C-O-C$: Epoxide

$-COOH$: Carboxyl

DI : Deionized

GAC : Granular activated carbon

GO : Graphene oxide

H^+ : Hydrogen ion

H_2O_2 : Hydrogen peroxide

H_2SO_4 : Sulphuric acid

HCl : Hydrochloric acid

HOCs : Hydrophobic organic contaminants

HOO• : Hydroperoxyl radical

HOPG : Highly oriented pyrolytic graphite

INN : International Nonproprietary Name

IUPAC : International Union of Pure and Applied Chemistry

$K_2S_2O_8$: Potassium peroxodisulphate

$KMnO_4$: Potassium permanganate

KOH : Potassium hydroxide

MB : Methylene blue

Mn_2O_3 : Manganese(III) oxide

NACs : Nitroaromatic compounds

$NaIO_3$: Sodium iodate

OFG : Oxygenated functional group

OH^- : Hydroxide ion

$-OH$: Hydroxyl

P_2O_5 : di-Phosphorus pentoxide

PAHs : Polycyclic aromatic hydrocarbons

RB5 : Reactive black 5

rGO	: Reduced graphene oxide
RhB	: Rhodamine B
ROS	: Reactive oxygen species
SSA	: Specific surface area
SWCNTs	: Single-walled carbon nanotubes
TPV	: Total pore volume
UV-Vis	: Ultraviolet-visible
VB	: Valence band
WO_3	: Tungsten(VI) oxide
XRD	: X-ray diffraction
ZnO	: Zinc oxide
$ZnWO_4$	: Zinc tungstate

LIST OF APPENDICES

CHAPTER 1: INTRODUCTION

1.1 Research Background

Dyes are a major component used in the different areas of textile manufacturing industries. Nevertheless, these dyes are non-biodegradable, and are often released into the water environment without proper precautions (A. Mohamed et al., 2016). Most dyes are stable, colourant, recalcitrant, and even potentially toxic and carcinogenic, which can have deleterious effects on human health and ecosystems (S. Li et al., 2018). Owing to the intricate aromatic structures, dyes are particularly resistant towards degradation brought about by light, ozone, biological activity, and other means of natural degradation (Thakur et al., 2017). Several conventional treatment methods such as adsorption, biosorption, coagulation, filtration, incineration, sedimentation and microbial degradation have been used for the removal of dyes (Chan et al., 2011; Rao et al., 2009; Rauf & Ashraf, 2009; Seddigi, 2010). Adsorption is by far the most common approach used in industry, due to high adsorption capacity and accessibility of inexpensive adsorbents (Kyzas & Kostoglou, 2014). Recently, photocatalysis has been developed and becomes a more promising technique in tackling this environmental issue. Photocatalysis is an advanced oxidation process (AOP), whereby photoinduced hydroxyl (•OH) and superoxide ($•O_2^-$) radicals are generally accepted as the reactive oxygen species (ROS) in the oxidation of dye pollutants (Bora & Mewada, 2017; Lee et al., 2016). For both adsorption and photocatalysis processes, the elimination of dyes greatly depends on the specific surface area (SSA) of materials used (Sandoval et al., 2017).

Reduced graphene oxide (rGO) is a form of graphene that has been chemically altered. It bears a resemblance to pristine graphene, but it is more economically suitable for large-scale production (Marichy et al., 2013). rGO is commonly used as a starting material for the manufacture of graphene-based composites (Hu et al., 2013). The fabrication of rGO is attainable in various ways, including microwave, thermal, photo-thermal, chemical, photo-chemical, as well as microbial/bacterial processes (Bianco et al., 2013; Rowley-Neale et al., 2017). Chemical method appears to be advantageous due to its affordability, simplicity, and large-scale production (Q. A. Khan et al., 2017). Particularly, there are three main steps in preparing rGO via this method. The first step is the oxidation of graphite powder to graphite oxide by introducing oxygenated functional groups (OFGs) on the surface of graphene layers. Owing to the existence of OFGs like carboxyl (−COOH), hydroxyl (−OH), carbonyl (C=O) and epoxide (C−O−C) groups, graphite oxide is able to disperse in polar solvents, thereby forming stable dispersions. Then, the exfoliation of graphite oxide produces graphene oxide (GO). This can be accomplished by either sonication or mechanical stirring to create single/few-layered GO sheets. Lastly, GO is then reduced to rGO by eliminating surficial OFGs (Emiru & Ayele, 2017).

Carbon-based materials have been traditionally employed as adsorbents to eliminate organic and inorganic contaminants (Thangavel & Venugopal, 2014; Tofighy & Mohammadi, 2011; M. Zhang et al., 2014; G. Zhao et al., 2011). Activated carbon is a widely known adsorbent material (A. J. Kumar & Namasivayam, 2014). Recently, rGO has showed increasing usage in dye adsorption application (Gupta & Khatri, 2017; H. Kim et al., 2015; Mahmoodi et al., 2017; P. Sharma et al., 2013; Sun et al., 2014). Due to the existence of remaining OFGs on the surface, along with some defects in the graphitic domains, rGO is deemed efficient for the adsorptive removal of dyes (S. Cui et al., 2014). Generally, rGO interacts with dyes through π-π interaction, electrostatic interaction, hydrophobic association and structural conjugation. These interactions enable a wide range of dyes to adsorb on rGO (Minitha et al., 2017). In order to facilitate the diffusion of dye molecules and improve the dye adsorption capacity, rGO with high porosity and large SSA, which increases the number of active sites, is preferable, and this is achievable by controlling the quality of GO precursor and reduction method used (Zhu et al., 2013).

Today, the photodegradation of dyes has been used as a tool for manifesting the technological benefits of photocatalysis. Generally, when a photocatalyst absorbs photon energy from light (with equal or higher energy than its band gap), the photoexcitation of electrons happens, thereby forming electron-hole pairs. The photogenerated electrons and holes then take advantage of water and oxygen molecules in the environment to form ROS, which are responsible to break down the dye molecules (T. Liu et al., 2017). It is learnt that rGO behaves like semiconductors, and its band gap can be tuned by regulating its oxygen content (Abid et al., 2018). For this reason, there are various studies reporting the usage of rGO in the photodegradation of dyes, especially methylene blue (MB) dye, which is a common harmful contaminant found in wastewater (Chandra et al., 2012; Kaur et al., 2016; M. J. S. Mohamed & Bhat, 2017; Shaohua Xu et al., 2015; Xue & Zou, 2018; Y. Zhao et al., 2014). Nevertheless, the photoactivity of rGO was found to be relatively poor, with no complete removal of dye was observed.

Therefore, in this work, the rGO photocatalyst with excellent adsorption properties and photoactivity was manufactured via a facile and nature-friendly solvothermal approach without using any toxic reducing agents. The adsorption and photoactivity of as-fabricated rGO photocatalyst towards the removal of model cationic dye, MB, were investigated. The aim is to provide a further insight into the dye adsorption and photodegradation behaviours of rGO.

1.2 Problem Statement

Generally, dyes are classified into three categories, which are anionic, cationic and non-ionic. Among them, cationic dyes have extensive applications in dyeing industries, particularly for dyeing cotton, leather, wool, silk and paper. Despite of their wide usage, cationic dyes are more environmentally unfriendly as compared to anionic and non-ionic dyes. They possess very high tinctorial values, which greatly influence the aesthetic quality of water environments. In addition, the cationic properties allow them to interact with the negative charges on the cell surface, as well as endow them the access into the cells, leading to accumulation in the cytoplasms (Konicki et al., 2018). Among the dangerous cationic dyes, MB is widely utilized for dyeing wool, silk and cotton. It is said to cause skin irritation, cyanosis, methemoglobinemia, eye burn, dyspnea, tachycardia and convulsions. Moreover, if ingested, it can result in diarrhea, vomiting, nausea and irritation to the gastrointestinal tract (Fil et al., 2012). Hence, the decontamination of MB from waste effluents has become of great importance, and represents the main purpose of this research work in the hope to alleviate environmental issues.

All this while, the reduction of GO has been conventionally achieved by using strong reductants, especially hydrazine or sodium borohydride (Luo et al., 2011; Stobinski et al., 2014). Typically, different reducing agents result in rGO with different properties. For example, sodium borohydride partially decreases the density of −OH groups, whereas hydrazine leads to the formation of C-N bonds, which, in some circumstances, function as active sites (Jin et al., 2013; D. Kim et al., 2012). Notwithstanding the fact that higher quality of rGO can be obtained, such reductants have high chemical toxicity and are detrimental to the environment (Park et al., 2011). For this reason, the search for more environmentally friendly alternatives has become of great significance in the current era. Particularly, alcohols such as ethanol have garnered considerable attention due to their simplicity and cost effectiveness (Daniel R Dreyer et al., 2011; Soares et al., 2017). Therefore, this work desires to prepare rGO via a simple solvothermal technique by utilizing ethanol as an environmentally friendly solvent, and then determine its performance towards MB removal.

1.3 Research Objectives

In this study, the objectives are as listed below:

1. To synthesize rGO by using a facile in situ solvothermal approach without involving any toxic reducing agents.
2. To investigate the effects of various reaction temperatures and reaction durations on the reduction of GO.
3. To examine the effects of catalyst loading, initial dye concentration, light intensity, and pH of solution on the adsorption and photoactivity of rGO.

1.4 Research Outline

There are six sections in this research work: (1) selection of materials, (2) pre-treatment of graphite powder, (3) preparation of GO, (4) preparation of rGO, (5) methods of characterization, and (6) adsorption and photoactivity measurements. Firstly, materials were selected and used without further purification. Then, graphite powder was pre-treated and oxidized to GO by using modified Hummers' method. In order to obtain rGO, GO was reduced via a nature-friendly solvothermal approach. Here, the effects of reaction temperature and reaction duration on the reduction of GO were examined. After that, GO and rGO samples were characterized by the following analytical techniques: (1) Raman spectroscopy to determine the ordered and disordered structures, (2) EDX to determine the elemental compositions, (3) XRD to investigate the crystalline phases, (4) BET and BJH to measure the specific surface areas, pore sizes and total pore volumes, and (5) UV-Vis spectrophotometry to elucidate the optical properties of GO and rGO samples. Lastly, the MB adsorption and photodegradation processes were evaluated. The effects of catalyst loading, initial dye concentration, light intensity, and pH of solution on the adsorption and photoactivity of optimum rGO sample were thereafter investigated.

1.5 Thesis Organization

This thesis consists of five chapters. Chapter 1 outlines the research background, problem statement, research objectives, research outline, and thesis organization. Chapter 2 introduces the different forms of graphite, along with its basic structure and properties. Then, the fabrication techniques, as well as the photocatalytic properties of graphene and graphene derivatives are demonstrated. This chapter also briefly illustrates the fundamental principles involved in semiconductor photocatalysis. Chapter 3 describes the experimental procedures involved in this research work, which include the selection of materials, pre-treatment of graphite powder, preparation of GO and rGO, characterization methods, as well as the adsorption and photoactivity measurements. Chapter 4 discusses the effects of different reaction temperatures and reaction durations on the reduction of GO, and the effects of catalyst loading, initial dye concentration, light intensity, and pH of solution on the adsorption and photoactivity of optimum rGO sample towards MB removal. Chapter 5 summarizes the main findings of this work and suggests various approaches for future research.

CHAPTER 2: LITERATURE REVIEW

2.1 Graphite

The origin of the word ‘graphite’ was linked to the word ‘graphein’ in the language of Greek, denoting to draw or to write, as resulted from the fact that it was used to make dark marks on paper. Graphite belongs to one of the prominent crystalline allotropes of carbon. It has been utilized for numerous centuries, and even until now, it still attracts high attention of research communities. In history, graphite was employed as molds to make cannon balls. Other historical applications of graphite include crucibles, electrodes, lubricants, motor brushes, and materials processing (Raza, 2012). Among the carbon allotropes, graphite possesses the highest stability at 25 °C and 1 atm pressure (Oxtoby et al., 2015). Annually, there are approximately 1.1 million tons of graphite mined throughout the world (Aliofkhazraei et al., 2016). There are two major groups of graphite, which are natural graphite and synthetic graphite. The former one can be further classified as amorphous, vein, and flake graphite based on their unique geological environments.

2.1.1 Natural and Synthetic Graphite Materials

The term ‘amorphous graphite’ is considered as a misnomer because all graphite materials are by right crystalline carbon materials with honeycomb lattice. Nevertheless, this term is used because this particular form of natural graphite has lumps with irregular shapes. Amorphous graphite is usually present in metamorphic rocks such as coal, slate, and shale deposits, or it can be found in beds. It exists in the form of minute crystalline particles. Seams of amorphous graphite originate from the geologic metamorphism of anthracite coal deposits. Among the three forms of natural graphite, amorphous graphite is the most abundant yet the least graphitic form due to its microcrystalline structure and the absence of long-range crystalline order. It is known that this type of graphite is hard to refine because it is intimately associated with the mineral matter. Amorphous graphite is extensively used in paints, polishes, greases, and lubricants (Dante, 2015).

Vein graphite is the natural graphite in its rarest form due to its origin and formation process. It occurs in the metamorphic rocks of granulite facies, and is believed to derive from the underground layer of unrefined liquid petroleum, which after some time under high temperatures and pressures is transformed to graphite. Typical veins of graphite can range from centimeters to meters wide. However, the purest graphite is only present in the middle of the vein furthest from the rock in which it resides. Vein graphite merely accounts for 1% of global graphite production. It can only be mined underground in Sri Lanka, where it happens to be the only nation in the world to export commercially-viable vein graphite. Since vein graphite is directly deposited from the liquid state at high temperatures, its crystallinity is superbly high, thus providing it with excellent electrical and thermal conductivity. Generally, the usage of vein graphite is relatively broad, especially in the manufacturing of greases, abrasive materials, batteries, and metal parts (Kumarasinghe et al., 2013; Luque et al., 2014).

Flake graphite is less common in nature and has higher quality than amorphous graphite. It is mostly of an organic origin rather that inorganic. Flake graphite can be found in certain metamorphic rocks like gneiss, limestone, and schist. It often appears as segregated plate-like particles with uniform surfaces and sharp-cornered edges. Flake graphite is either equally dispersed throughout the ore body, or in concentrated, lens-shaped pockets. It can be refined by using conventional ore-processing methods, which mainly involve crushing, grinding, and flotation processes. In comparison to amorphous graphite, flake graphite is more highly-priced. Flake graphite is widely employed in high-value applications such as coatings, friction moderators, fuel-cell bipolar plates, batteries, electrically conductive materials, gaskets, lubricants, pencils, refractories, powder metallurgy, and thermal materials (Mukhopadhyay & Gupta, 2012).

Synthetic graphite is a man-made material. It is often obtained from fossil fuels such as petroleum and coal by heat-treating them under high temperatures inside an inert atmosphere. A high temperature is necessary to achieve the solid-state phase transition, thereby resulting in the formation of a three-dimensionally arranged crystalline carbon. The raw materials used for constructing graphite are extremely selective because not all carbons are suitable. Generally, calcined petroleum coke is utilized as raw material, while coal-tar pitch is employed as matrix binder. The purity of synthetic graphite greatly relies on the purity of the starting petroleum coke used. This kind of graphite is highly conductive and is commonly used in metallurgy to produce graphite electrodes. Highly oriented pyrolytic graphite (HOPG) is known to be the highest-quality synthetic graphite (Moradi & Botte, 2016; Nasir et al., 2015).

2.1.2 Properties and Structure of Graphite Materials

Graphite is a giant molecular structure, which contains numerous carbon layers that are arranged in a parallel direction. A single atomic layer, which is known as graphene, has a hexagonal lattice, and the carbon atoms are separated from each other by a distance of 1.42 Å. Several graphene layers are then stacked together in an ABABAB configuration, which shows a gap of 3.35 Å in between the layers. The graphite structure belongs to the nonsymmorphic space group $P6_3/mmc$ (D_{6h}^{4}), with unit-cell dimensions of $a = b = 2.46$ Å and $c = 6.69$ Å (Delhaès, 2000). In graphite, the carbon atoms are sp^2-hybridized, which means that each carbon atom merely contributes three of its valence electrons for the formation of σ bonds. The last valence electron, which is responsible for the formation of π bond, then moves freely in the layered planes, creating strong bonding forces. However, the π electrons in one sheet do not directly interact with those in the neighbouring sheets. Instead, the delocalization of π electrons leads to the formation of weak van der Waals forces, which are then used to hold the carbon layers together (Jingang Wang et al., 2019; Wu, 2017), as showed in Figure 2.1.

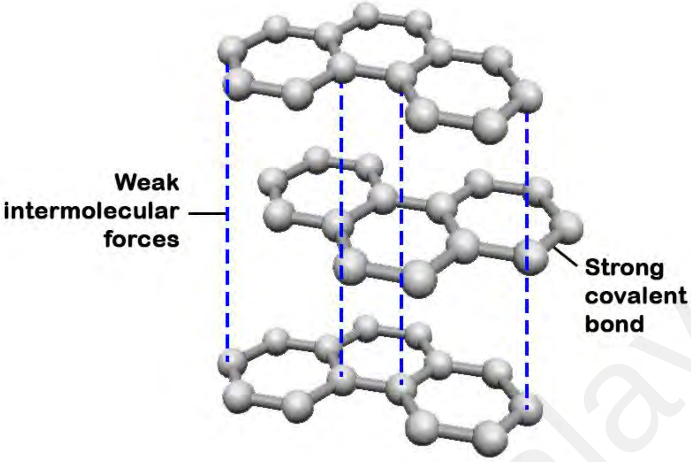

Figure 2.1. The atomic structure of graphite.

Graphite is black to dark gray in colour, opaque, and very soft. It has a glossy black streak, metallic sheen and a distinctive greasy feeling. Graphite has a density of 2.26 g·cm^{-3} and a high melting point of 3927 °C. The strong covalent bonds must be broken in order to melt graphite. Graphite is not able to dissolve in water and organic solvents because there is almost no interaction between them, which makes it impossible to break the strong covalent bonds in this carbon allotrope. Graphite has the ability to conduct electricity efficiently because of the presence of delocalized π electrons, which are free to move throughout the sheets. The conductivity is greater when it is parallel to the carbon sheets, rather than perpendicular to the carbon sheets. Graphite has a high thermal stability in vacuum or inert surroundings. However, when atmospheric oxygen is present in the environment, it readily undergoes oxidation at temperatures above 700 °C to form carbon dioxide (CO_2). Graphite is a highly anisotropic material. In fact, anisotropy is an exceptional characteristic of individual graphite crystals. Graphite is considered to be chemically unreactive due to its inertness towards most acids, alkalis, and harmful gases.

That being said, even the most reactive element, fluorine, can only react with graphite at temperatures above 400 °C (Kharisov & Kharissova, 2019).

2.2 Graphene

Graphene can be described as a layer of carbon atoms, which has the thickness of a single atom, that are assembled in a two-dimensional hexagonal lattice. Being the hardest, finest, and toughest material on earth, it is currently the most widely investigated substance among researchers. Graphene is the fundamental unit of all kinds of graphitic structures, including zero-dimensional fullerenes, one-dimensional carbon nanotubes, and three-dimensional graphite (A. Tiwari et al., 2017), as illustrated in Figure 2.2.

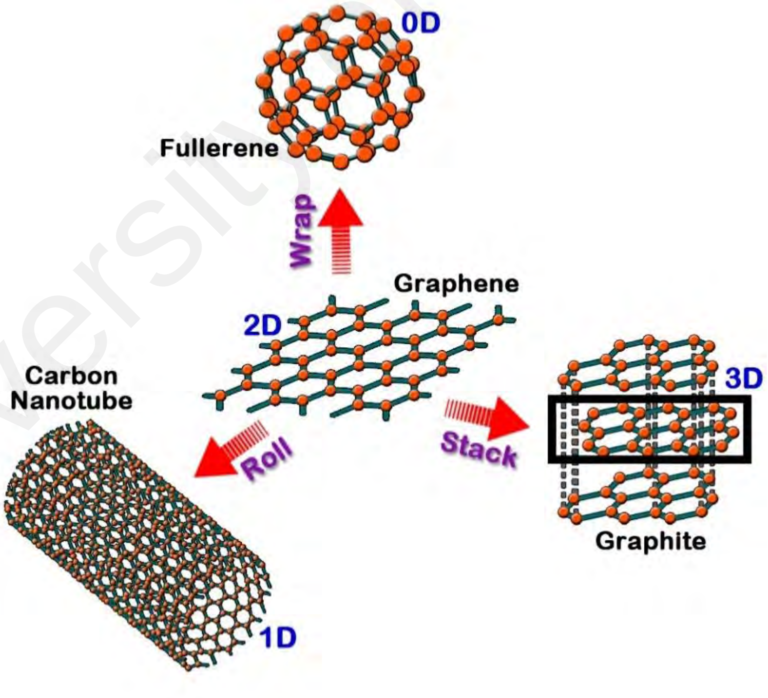

Figure 2.2. Graphene is the basic building block of all graphitic forms.

It is learnt that the properties of graphene differ based on the amount of graphene sheets stacked. Generally, graphene has various excellent properties, which include high optical transmittance (~97%), outstanding Young’s modulus (~1.0 TPa), large theoretical SSA

(~2630 $m^2 \cdot g^{-1}$), superb thermal conductivity (~5000 $W \cdot m^{-1} \cdot K^{-1}$), and remarkable intrinsic mobility (~200,000 $cm^2 \cdot V^{-1} \cdot s^{-1}$) (Aliofkhazraei et al., 2016; Hansora & Mishra, 2018). Due to these excellent properties, graphene has become an ideal substance for use in many applications, for example catalysis, energy storage, polymer composites, degradation of dyes and volatile organic compounds, CO_2 reduction, hydrogen evolution, nanoelectronics, chemical and biochemical sensing, photovoltaics, supercapacitors, and so on. Pure graphene has a zero gap in between its valence band (VB) and conduction band (CB). For this reason, it cannot participate in the charge separation step of photocatalysis. Nevertheless, it can still assist in better charge separation on its interface owing to its exceptional charge carrier mobility and large SSA (A. Tiwari & Syväjärvi, 2016).

2.2.1 Synthesis of Graphene and Graphene Derivatives

Natural graphite, which is essentially made up of layers of graphene stacked together, is an abundant and economical source for acquiring graphene sheets (Hack et al., 2018). Initially, tiny flakes of graphene, which were about a few microns in size, were mechanically exfoliated from graphite by using scotch tape. Nevertheless, this method of preparation is inappropriate for the fabrication of a large amount of graphene, as well as for the composition of graphene with other materials (Bhuyan et al., 2016). Since then, the manufacture of graphene has been achieved by other more reliable techniques, such as chemical vapour deposition process, epitaxial growth process, and chemical method. In chemical vapour deposition, large area of single- to few-layered graphene films can be produced. However, high temperatures are involved in this process, as well as the requirement of using hydrocarbons and pure hydrogen as precursor and carrier gas, respectively, which greatly restricts its range of applications. Epitaxial growth is also another technique used to produce defect-free graphene. Despite the fact that superlative properties can be obtained, the resulting graphene sheets are small, which makes it hard to assemble them into films. Moreover, the high energy requirement also limits its application for mass production. Among these mechanisms, chemical method is the most well-known approach used for graphene synthesis because a large amount of graphene can be produced. In this sense, graphene is widely known as rGO. Generally, this method involves three main steps: (1) oxidation of graphite powder to graphite oxide, (2) exfoliation of graphite oxide either by sonication or mechanical stirring to construct single- or few-layered GO, and (3) reduction of GO to rGO by removing surficial OFGs (Emiru & Ayele, 2017; Lin et al., 2018). The structure of monolayer graphene, GO and rGO are represented in Figure 2.3.

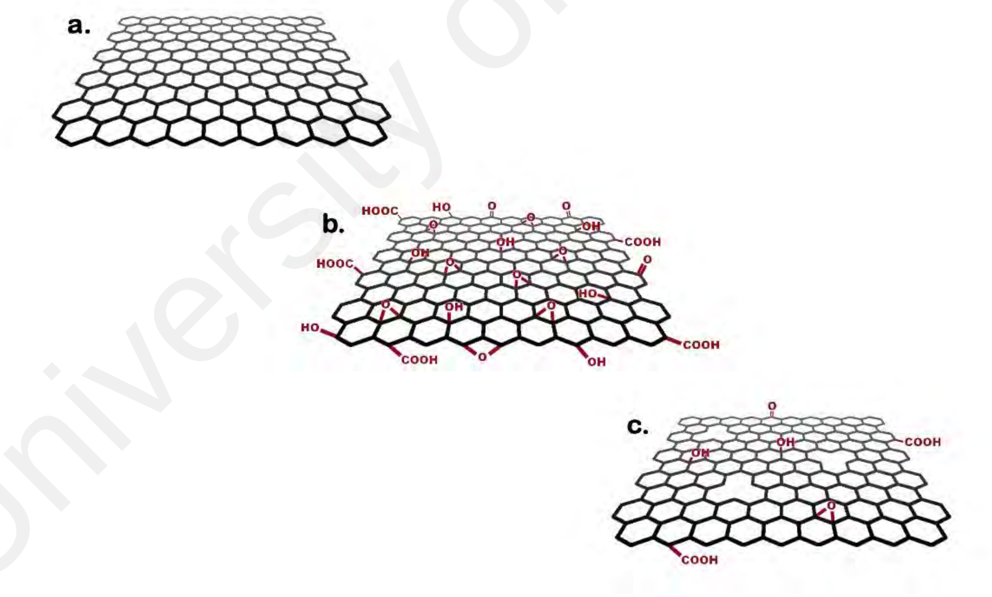

Figure 2.3. Structure of (a) graphene, (b) GO, and (c) rGO.

One of the main derivatives of graphene is GO, which exists as a functionalized graphene sheet that contains −OH, C=O and C−O−C groups on each side of the sheet, as well as some −COOH groups at the borders. These functionalities provide GO a strong hydrophilic character, making it capable of dispersing in polar solvents, especially water more easily. In addition, the presence of sp^2- and sp^3-hybridized carbon atoms also leads to more kinds of surficial interactions to take place. In spite of these advantages, the presence of such oxidized regions in GO greatly disturb the long-range conjugated carbon network and π-electron cloud of the graphene sheet, thereby obstructing the free movement of electrons. On the other hand, rGO is also a widely studied derivative of graphene (B. Li et al., 2016). Although rGO highly resembles graphene, it contains some defects in its structure, and remaining OFGs on its surface. In comparison to GO, rGO demonstrates a relatively higher electrical conductivity due to the partial recovery of π-conjugation. As pristine graphene has a hydrophobic nature, the presence of residual OFGs on rGO sheets facilitates the embedment process of metal nanoparticles and/or semiconductors in rGO, as well as the formation of macroscopic structures, both of which are advantageous for constructing photocatalysts with high performance (Báez et al., 2017). Despite the fact that rGO conducts electricity more poorly than pristine graphene, it can still be benefited in various ways, including its large SSA, high yield of reaction, excellent biocompatibility, high potential for functionalization, and inexpensive production (Daniel R. Dreyer et al., 2010).

2.2.2 Adsorption Properties of Graphene and Graphene Derivatives

Generally, there are three adsorption sites on a graphene surface, which are the open-up surface, longitudinal surface, and interstitial channels (Ersan et al., 2017). Owing to the hydrophobic nature of pure graphene, the adsorptive removal of organic pollutants in wastewater is more effectively achieved by using GO and rGO (Nupearachchi et al., 2017). The adsorption of organic contaminants varies with the physicochemical properties of GO and rGO, including SSA, pore size distribution, OFGs, and surface charge. In addition, the presence of defects, folds, and wrinkles in GO and rGO also play important roles in the elimination of organic pollutants (Jun Wang et al., 2016; J. Wang et al., 2014).

One of the most important aspects that influences the adsorption of organic contaminants is the SSA of adsorbents. However, in some cases, SSA is not the sole determining factor for adsorption process. For instance, Y. Li et al. (2013) revealed that although GO exhibited a smaller SSA than carbon nanotube (CNT), the MB adsorption over GO was higher than that accomplished with CNT. This was due to the distinctive single-atom-layered structure of GO. Zhou et al. (2015) depicted that even after SSA normalization, rGO still exhibited a lower adsorption capacity towards aliphatic synthetic organic compounds as compared to both single-walled carbon nanotubes (SWCNTs) and granular activated carbon (GAC).

Furthermore, the pore size distribution in adsorbents also affects the adsorptive removal of organic pollutants. The pore size distribution analysis is important to find out the fraction of total pore volume (TPV) which is accessible to organic contaminants (Apul et al., 2013). In the presence of very small-sized pores, the adsorption of organic pollutants is restricted. Nevertheless, organic contaminants with low molecular weights tend to adsorb on the micropore sites of porous adsorbents (Bandosz, 2006). Micropores are normally adsorption sites with high binding energies. As the size of organic pollutant gets nearer to that of the adsorbent, the interaction between them becomes stronger (Ersan et al., 2017).

Besides that, the adsorption of organic contaminants also relies on the presence of OFGs in GO and rGO. For GO, the presence of surficial OFGs increases its polarity, which then improves its dispersibility in water, and increases its adsorption capacity towards organic pollutants. However, it is also possible that OFGs become the adsorption sites for water molecules, thereby creating water clusters around them, and obstructing organic contaminants from occupying the adsorption sites (Ersan et al., 2016; Zhou et al., 2015). Due to low surface polarity, rGO is expected to obtain a higher adsorption capacity for organic contaminants as compared to GO (F. Wang et al., 2014).

Apart from that, the surface charge of adsorbents also plays an important role in the elimination of organic pollutants by adsorption. Generally, more adsorption sites were made available when a positive or negative charge was created on the surface of adsorbent (F. Wang et al., 2014). Ramesha et al. (2011) mentioned that by increasing the negative charge density on the surface of exfoliated GO, the adsorption of cationic dyes was subsequently enhanced via electrostatic interactions. Despite the fact that rGO demonstrated a lower negative charge density than exfoliated GO, the −COOH functionalities were still present on the surface, thereby allowing it to interact with cationic dyes.

Other morphological factors of adsorbents like defects, folds, and wrinkles also contribute to the adsorptive removal of organic contaminants. J. Wang et al. (2014) unveiled that the wrinkles on the surface of rGO were responsible for creating high-energy adsorption sites on the groove regions, which, together with the presence of π-π interactions, improved the adsorption affinity of rGO towards polycyclic aromatic hydrocarbons (PAHs). As for GO, the adsorption of PAHs was taken over by the −COOH functionalities attached to its edges. This was attributed to the restriction of π-π interactions on polar surfaces, and also the disappearance of groove fractions. Chen & Chen (2015) reported that a better adsorption capacity for nitroaromatic compounds (NACs) was achieved when additional adsorption sites were provided by the defects in rGO. (Jun Wang et al., 2016) showed that more wrinkles and folds were generated when the surface of rGO was thermally treated with potassium hydroxide (KOH). As a result, more adsorption sites were produced, thereby improving the adsorption of hydrophobic organic contaminants (HOCs).

2.2.3 Photocatalytic Properties of Graphene and Graphene Derivatives

Photoactive semiconductor materials with suitable band gaps are often used as photocatalysts (Kang et al., 2019; Tong et al., 2012). As there is zero gap in between the VB and CB, pristine graphene is unfit for use as a photocatalyst (G. Lu et al., 2013). However, when graphene undergoes oxidation, a band gap is created, which endows GO with semiconductor properties. The band gap of GO is directly associated to the oxidation and reduction processes. Upon oxidation, OFGs are introduced onto the surface of graphene layers. Following the conversion of sp^2 bonds of carbon atoms to sp^3 bonds, the number of sp^3-hybridized domains then increases, which results in the opening of a band gap in GO. When GO is reduced to rGO, some of the surficial OFGs are eliminated, thereby converting the sp^3 carbon atoms back to sp^2 carbon atoms. As the sp^2 carbon network is partially restored, the band gap is subsequently reduced. Hence, the band gaps of GO and rGO are tunable over a wide range of values by managing the quantity of surficial OFGs via oxidation and reduction processes (Loh et al., 2010; S. Wang et al., 2017). Historically, graphene derivatives were often served as support materials in semiconductor photocatalysis (Abid et al., 2018; Xiang et al., 2012). Up to now, there are only a few studies investigating the usage of graphene derivatives as standalone photocatalysts in some applications such as degradation of contaminants, water splitting, and formation of methanol from CO_2, as summarized in Table 2.1. More research is thus needed to have a better understanding and explore the potential of these materials as efficient semiconductor photocatalysts.

Table 2.1. Photocatalytic applications of graphene derivatives.

Photocatalyst	Bandgap (eV)	Application	Performance	Reference
Graphite oxide	Direct: 3.3-4.3 Indirect: 2.4-3.0	Production of H_2 from water	17,000 µmol in 6 hr	(T. F. Yeh et al., 2010)
GO	Direct: 3.26	Reduction of resazurin into resorufin	44.10% in 40 min	(Krishnamoorthy et al., 2011)
GO	Direct: 2.8	Production of H_2 from water	0.013 µmol h^{-1}	(Matsumoto et al., 2011)
Graphite oxide	Direct: 3.2-4.2 Indirect: 2.3-2.8	Production of H_2 from water	11,000 µmol in 6 hr	(T.-F. Yeh et al., 2011)
Graphite oxide	Direct: 3.8-4.6 Indirect: 2.7-3.6	Production of O_2 from water	28 µmol in 8 hr	(T.-F. Yeh et al., 2011)
GO	N/A	Photodegradation of rhodamine B	95% in 4 hr	(Guardia et al., 2012)
GO	Direct: 3.2-4.4	Reduction of CO_2 to methanol	0.172 mmol g cat^{-1} h^{-1}	(Hsu et al., 2013)
GO	Direct: 4.04 Indirect: 1.87	Photodegradation of phenol in water	38.62% in 2 hr	(Bustos-Ramirez et al., 2015)
GO	Direct: 4.0 Indirect: 1.8	Photodegradation of 4-chlorophenol	97% in 2 hr	(Bustos-Ramírez et al., 2015)
rGO	N/A	Photodegradation of reactive black 5	49% in 60 min	(Wong et al., 2015)

In previous years, researchers have been exploring the photoactivity of graphene derivatives towards the degradation of contaminants. Guardia et al. (2012) studied the decomposition of rhodamine B (RhB) dye over GO sheets at ambient temperature under UV irradiation. As the GO sheets were illuminated with intense UV light, a high-temperature and reactive environment was induced at and around the GO sheets suspended in aqueous medium, thereby facilitating the photodegradation reaction. The decomposition rate of dye obtained with the presence of GO sheets was found to be analogous to that achieved with titania. Bustos-Ramirez et al. (2015) investigated the photoactivity of GO on the removal of phenol in water. The GO photocatalyst was fabricated through the modification of duration of graphite oxidation, as well as the ultrasonic degassing of graphite oxide. Due to the presence of OFGs and a certain roughness in GO sheet, the as-prepared photocatalyst was able to achieve up to 38% of removal efficiency of phenol solution under the irradiation of UV light. Bustos-Ramírez et al. (2015) also examined the photodegradation of 4-chlorophenol (4-CP) in water by using GO. The results showed that in the presence of UV light, approximately 97% of 4-CP was removed and mineralized. The remaining by-products, which in this case were carboxylic acids and aromatic intermediates, were found to be in lower concentrations as compared to that obtained in photolysis. Wong et al. (2015) studied the usage of rGO photocatalyst for the elimination of reactive black 5 (RB5) dye in aqueous solution. The reduction of GO was achieved via an advanced chemical reduction approach. Under UV illumination, a 49% removal efficiency of RB5 dye was obtained. This was due to the superlative electronic conductivity of rGO, thereby hindering the recombination of electrons and holes.

Besides that, the photocatalytic potential of graphene derivatives for water splitting was also reported. T. F. Yeh et al. (2010) demonstrated a stable production of H_2 from both water and methanol solution when graphite oxide photocatalyst, which was fabricated through a modified Hummer's method, was illuminated with either UV or visible light. The presence of cocatalysts was not needed because the dispersibility of graphite oxide in water is extremely high. Although the photocatalytic reaction led to a reduction in band gap of graphite oxide, it did not influence the stable evolution of H_2 over the photocatalyst. Matsumoto et al. (2011) showed that in the presence of UV light, an aqueous suspension of GO nanosheets was capable of undergoing photoreactions to produce H_2 and CO_2. This resulted in the formation of rGO nanosheets with many defects and holes. When GO nanosheets were subjected to photoelectrochemical tests, the generation of CO_2 led to the production of a large anodic photocurrent, while the reduction of surficial OFGs, along with the generation of H_2 created a small cathodic photocurrent. T.-F. Yeh et al. (2011) also revealed that with a suitable band gap, GO could be used as a photocatalyst to induce both the oxidation and reduction processes of water under light irradiation. The band gap of GO was mostly regulated by VB edge instead of CB edge. As a result, a large and stable amount of H_2 was obtained from methanol solution, while only a very little amount of oxygen was generated from silver nitrate ($AgNO_3$) solution during the photocatalytic reaction. By employing sodium iodate ($NaIO_3$) solution as a sacrificial reagent, the photocatalytic reduction of GO was suppressed, thereby improving the production of oxygen.

Apart from that, there are also studies depicting the role of graphene derivatives, especially GO, as promising materials for other photocatalytic applications. According to Hsu et al. (2013), the conversion of CO_2 to methanol could be achieved at a rate of 0.172 mmol g cat^{-1} h^{-1} when GO photocatalyst, which was acquired through a modified Hummer's method, was irradiated with visible light. The methanol conversion rate of GO was found to be six times higher than that of P-25. In addition, Krishnamoorthy et al. (2011) also studied the photocatalytic performance of GO nanostructures towards the reduction of resazurin into resorufin. The formation of GO photocatalyst was realized via a modified Hummer's method. Upon UV light irradiation, the colour of aqueous solution changed from blue to pink. This was attributed to the presence of photoinduced electrons at the surface of GO, which was responsible for the occurrence of photocatalytic reaction.

2.3 Semiconductor Photocatalysis

In recent years, rapid industrialization has contributed so much to unsustainable pollution levels. AOPs are a nature-friendly technique meant to eliminate most types of contaminants, including water pollutants such as aromatics, dyes, insecticides, pesticides, volatile organic compounds, and so on. AOPs are based on the production of ROS like $\bullet OH$ and $\bullet O_2^-$ radicals. Each of these radicals has one unpaired valence electron, which enables them to actively react with a series of other chemical molecules that are otherwise difficult to break down. In contrast to conventional methods, AOPs are relatively better due to the production of thermodynamically stable and harmless end products, such as CO_2, water, and biodegradable organic compounds. Among the AOPs, the photocatalysis process has received much attention due to its superior performance in degrading various organic contaminants (T. Zhang et al., 2014).

Photocatalysis is a phenomenon where light energy is employed to excite semiconductors for the generation of electron-hole pairs. According to the band theory, a semiconductor is a material that has its VB separated from its CB by an energy gap. The VB is the highest occupied energy state that is nearly filled with electrons, while the CB, which is situated above the VB, is the lowest unoccupied energy state with almost no electron in it. Based on the physical states of reactants, the photocatalytic reactions can be classified as either homogeneous or heterogeneous photocatalysis (Ameta & Ameta, 2018). In the field of wastewater treatment, the heterogeneous photocatalysis appears to be more advantageous because it involves low operating costs, as well as ambient operating temperature and pressure. In addition to that, it also promotes the complete removal of parent compounds and their intermediate byproducts, leaving no traces of secondary pollution (C.-C. Wang et al., 2014). The basic mechanism of heterogeneous photocatalysis is depicted in Figure 2.4.

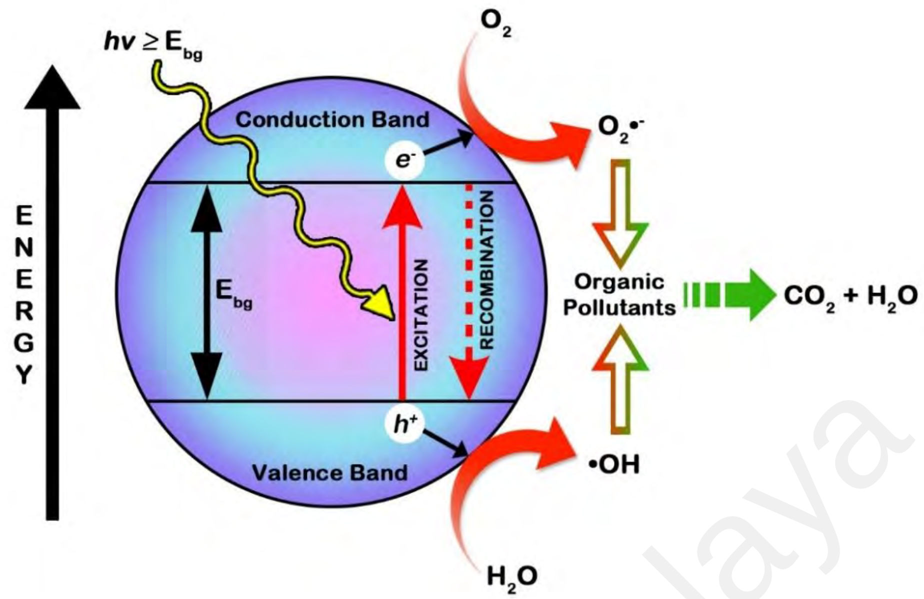

Figure 2.4. Basic mechanism of heterogeneous photocatalysis.

2.3.1 Mechanism of Semiconductor Photocatalysis

When a semiconductor is exposed to light of equal or higher energy than its own band gap, the energy of photons is absorbed by the electrons in VB. The electrons are then excited to CB, thereby creating holes in VB. This process leads to the formation of electron-hole pairs. Generally, the hole reacts with water molecules to produce •OH radicals, which are responsible for the oxidation of organic pollutants. It is also capable of achieving the direct oxidation of organic contaminants adsorbed on the surface of photocatalyst. In contrast to that, the electron reacts with oxygen molecules to form $•O_2^-$ radicals. At circumneutral pH, the $•O_2^-$ radicals are likely to exist as hydroperoxyl (HOO•) radicals, which, in conjunction with the oxygen molecules act as electron scavengers for the electrons in CB. The HOO• radicals can also undergo disproportionation to form hydrogen peroxide, which further reacts with either $•O_2^-$ radicals or CB electrons to produce more •OH radicals for the oxidation of organic pollutants. It is both •OH and $•O_2^-$ radicals that contribute to the partial or complete mineralization of organic contaminants (Bora & Mewada, 2017; Lee et al., 2016). The reaction mechanism is demonstrated as below:

$$\text{Photocatalyst} + h\nu \rightarrow h^{+}_{VB} + e^{-}_{CB} \quad \textbf{(2.1)}$$

$$h^{+}_{VB} + OH^{-} \rightarrow \bullet OH \quad \textbf{(2.2)}$$

$$\bullet OH + R{-}H \rightarrow \bullet R' + H_2O \quad \textbf{(2.3)}$$

$$h^{+}_{VB} + R \rightarrow \bullet R^{+} \rightarrow \text{Intermediates} \quad \textbf{(2.4)}$$

$$e^{-}_{CB} + O_2 \rightarrow \bullet O_2^{-} \quad \textbf{(2.5)}$$

$$\bullet O_2^{-} + H^{+} \rightarrow HOO\bullet \quad \textbf{(2.6)}$$

$$2HOO\bullet \rightarrow H_2O_2 + O_2 \quad \textbf{(2.7)}$$

$$H_2O_2 + \bullet O_2^{-} \rightarrow \bullet OH + OH^{-} + O_2 \quad \textbf{(2.8)}$$

$$H_2O_2 + e^{-}_{CB} \rightarrow \bullet OH + OH^{-} \quad \textbf{(2.9)}$$

The formation of ROS depends on the redox potentials of substrates, as well as the VB and CB edges of semiconductors (W. He et al., 2018). Generally, the reduction of a substrate only takes place when the redox potential of substrate is at a lower energy level than the CB edge. If the redox potential of $O_2/\bullet O_2^{-}$ is −0.16 V, the CB edge must be positioned at a comparatively higher energy level than the value in order to reduce oxygen molecules to $\bullet O_2^{-}$ radicals. On the other hand, the oxidation of a substrate is initiated when the redox potential of substrate is at a higher energy level than the VB edge. If the redox potential of $\bullet OH/H_2O$ is 2.38 V, the VB edge has to be placed at a rather lower energy level than the value so that •OH radicals can be generated. Therefore, in order for both reactions to occur simultaneously, it is necessary for a semiconductor to own a CB edge with energy level higher than −0.16 V, as well as a VB edge with energy level lower than 2.38 V (Basith et al., 2018).

2.3.2 Recombination of Electrons and Holes

When a photocatalyst absorbs light of equal or higher energy than its own band gap, the electrons are excited from VB to CB, thereby creating holes in VB. Nevertheless, these electrons tend to fall back to VB and return to their ground state, which results in the annihilation of electrons and holes. This phenomenon is known as recombination process. Generally, the recombination events can be classified into two categories: radiative and non-radiative recombination processes. Radiative recombination process occurs when the recombination mechanism involves the emission of light, whereas non-radiative recombination process takes place when heat energy is emitted instead (M. M. Khan et al., 2017), as illustrated below:

Radiative recombination:

$$h^{+}_{\mathrm{vb}} + e^{-}_{\mathrm{cb}} \rightarrow \text{photon (light)} \qquad \textbf{(2.10)}$$

Non-radiative recombination:

$$h^{+}_{\mathrm{vb}} + e^{-}_{\mathrm{cb}} \rightarrow \text{phonon (heat)} \qquad \textbf{(2.11)}$$

Both of these recombination processes are then further divided into three types based on their mechanisms: band-to-band recombination, Shockley-Read-Hall recombination, and Auger recombination processes, as demonstrated in Figure 2.5.

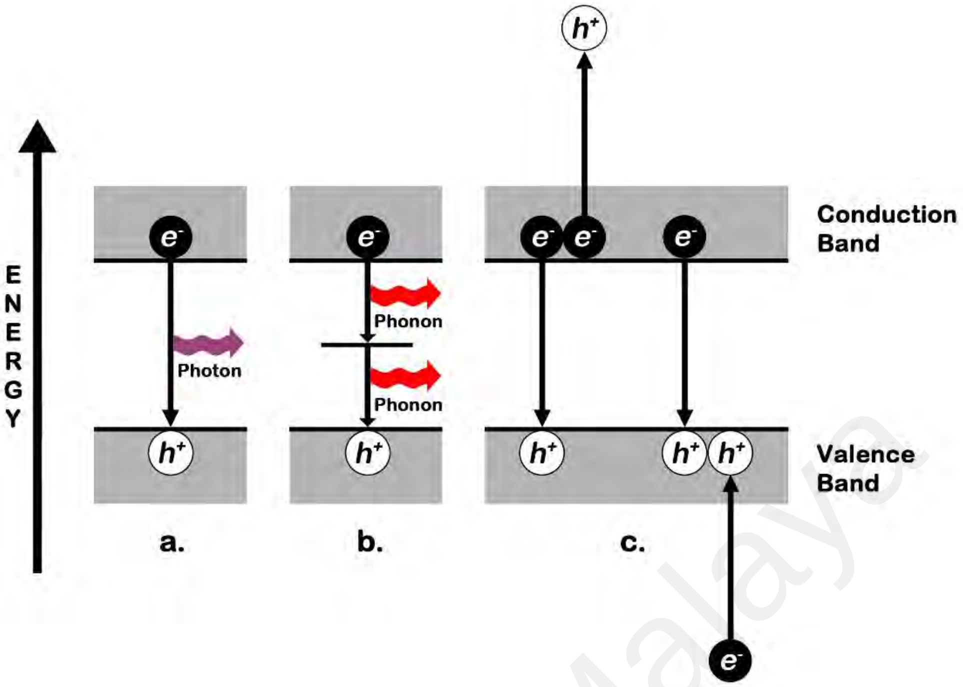

Figure 2.5. A schematic diagram of (a) band-to-band recombination, (b) Shockley-Read-Hall recombination, and (c) Auger recombination processes in semiconductors. The arrows describe the transition of electrons.

Band-to-band recombination process primarily belongs to radiative recombination process. In this mechanism, the excited electrons lose their energy and fall back into VB, thereby emitting photons. Shockley-Read-Hall recombination process, which is also termed as trap-assisted recombination process, is a non-radiative process. The presence of trap states in band gap of semiconductors allows trapping of electrons from CB and/or holes from VB. After being trapped, a carrier may again be released to the band where it is originated from, or it may subsequently recombine at the same trap state with another carrier of the opposite sign. Auger recombination process is also non-radiative, and it involves three carriers. When an electron-hole pair recombines through a band-to-band transition, the energy released is transferred to a third carrier instead, which is then excited to a higher energy state within the same band (De Laurentis & Irace, 2014; Kitai, 2018).

2.4 Methylene Blue (MB) Dye

MB (C.I. 52015) is a cationic dye belonging to phenothiazine group (Fradj et al., 2014). It is assigned with the name of 3,7-bis(dimethylamino)-phenothiazin-5-ium chloride by International Union of Pure and Applied Chemistry (IUPAC) nomenclature system. In addition, it is also known by International Nonproprietary Name (INN) nomenclature system as methylthionium chloride. MB is a heterocyclic aromatic chemical compound that has a molecular formula of $C_{16}H_{18}ClN_3S$ and a molar mass of 319.85 $g{\cdot}mol^{-1}$. At ambient temperature, it exists in the form of a solid powder, which is inodorous and dark green in colour, along with a metallic bronze sheen. MB can dissolve in water as well as other organic solvents (such as ethanol, methoxyethanol, and ethylene glycol) to produce a blue coloured solution. It has a melting point of about 100-110 °C, after which it starts to decompose when the melting point is reached (Dutta et al., 2011; Eskizeybek et al., 2012). The chemical structure of MB is showed in Figure 2.6.

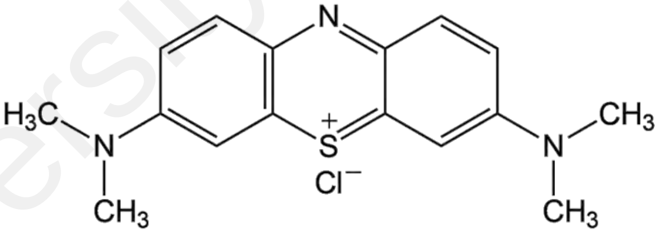

Figure 2.6. Chemical structure of MB dye.

2.4.1 Uses and Effects of MB Dye

Generally, the application of MB as a colourant can be found in a broad range of industries, such as acrylic, cotton, jute, leather, paint, paper, plastic, printing ink, silk, textile, and wool industries (Nasuha et al., 2010; Saha, 2010). Apart from that, it also possesses various applications in the fields of biology, chemistry, and medicine (Edison et al., 2016). In biology, MB is usually employed in staining techniques such as Jenner's and Wright's stains. Moreover, it is also useful for visualizing DNA in gel electrophoresis (Nejdl et al., 2018). In chemistry, MB is often used as a redox indicator, nootropic, and peroxide generator. Besides that, it has also found its application in water testing and sulfide analysis (Y.-B. Kim & Ahn, 2014). Due to strong antioxidant and antibiotic properties, MB is widely applied in the field of medicine as well (Ahn et al., 2017). Typically, it is used to treat several acute and chronic conditions, which include malaria, septic shock, methemoglobinemia, cardiopulmonary bypass, urinary tract infection, and carbon monoxide poisoning. In addition to that, MB is also a potential cure for Alzheimer's disease and mitochondrial dysfunction (Oz et al., 2009; Schirmer et al., 2011).

MB represents one of the most common organic pollutants found in water environment. Particularly, it is detected in groundwater and surface water such as lakes, rivers, and streams (Elango & Roopan, 2016). As MB is highly resistant to natural degradation, its existence in water environment substantially disturbs the stability of ecosystems (Sheng et al., 2009). MB prevents the light from penetrating into water, which retards the photosynthetic process of submerged plants, and hinders the growth of aquatic biota. In addition, its ability to chelate with metal ions also produces microtoxicity to aquatic life (J. N. Tiwari et al., 2013). On the other hand, MB possesses significant threats to human health as well. Some of its adverse effects include fever, nausea, diarrhea, cyanosis, delirium, dizziness, vomiting, headache, tachycardia, hypertension, hyperhidrosis, tissue necrosis, hemolytic anemia, and fecal discolouration (S. Chowdhury & Saha, 2012; Mitrogiannis et al., 2015). MB is able to cause burning eyes, which may result in permanent eye damage if left untreated. It can also lead to dyspnea, which is the shortness of breath, upon inhalation. Furthermore, if ingested, MB is capable of creating a burning sensation in the mouth (Rafatullah et al., 2010). Therefore, its elimination is of great importance to reduce its negative impacts on water environment and human health.

2.4.2 MB Adsorption and Photodegradation by rGO

Since the existence of MB in water environment is unfavourable, the removal of MB is absolutely necessary in wastewater treatment. It is learnt that both adsorption and photocatalysis processes are among the most effective and reliable techniques used to eliminate MB (Kant et al., 2014). Recently, the employment of rGO for adsorptive removal and photodegradation of MB has gained increasing interest among researchers, as depicted in Table 2.2. In spite of the fact that these studies have investigated the MB removal process in the presence of rGO, the photocatalytic performance of rGO has yet to be improved. For this reason, this work has been carried out for the first time in the attempt to optimize the MB photodegradation process using rGO, thereby increasing its potential as a standalone photocatalyst with excellent adsorption properties and photocatalytic performance for environmental remediation.

Table 2.2. MB adsorption and photodegradation by rGO.

Synthesis Method	Experimental conditions	Performance	Residual [MB] (ppm)	Reference
Chemical reduction with hydrazine	rGO: 1 mg [MB]: 1.3 ppm Light: 100 W Hg lamp	10% adsorbed and degraded at the same time in 90 min	1.2	(Chandra et al., 2012)
Electrochemical exfoliation from graphite electrode	rGO: 60 mg [MB]: 350 ppm Light: 15 W UV lamp	40% degraded in 90 min after adsorption in 4 hr	N/A	(Y. Zhao et al., 2014)
Chemical reduction with hydrazine	rGO: 50 mg [MB]: 15000 ppm Light: 100 W UV lamp	7% degraded in 100 min after adsorption of 12% in 20 min	12276	(Shaohua Xu et al., 2015)
Chemical reduction with hydrazine	rGO: 20 mg [MB]: 3.2 ppm Light: Sunlight	8% degraded in 180 min after adsorption of 50% in 60 min	1.5	(Kaur et al., 2016)
Microwave irradiation	rGO: 10 mg [MB]: 10 ppm Light: 250 W Hg lamp	19% degraded in 150 min after adsorption of 1% in 30 min	8	(M. J. S. Mohamed & Bhat, 2017)
Carbonization with apple juice	GO: N/A [MB]: 150 ppm Light: 125 W Xe lamp	33% in 60 min after adsorption in 40 min	N/A	(Kumbhakar et al., 2018)
Carbonization with apple juice	GO: N/A [MB]: 150 ppm Light: 6 W UV lamp	12% in 60 min after adsorption in 40 min	N/A	(Kumbhakar et al., 2018)
Photochemical reduction	rGO: 10 mg [MB]: 10 ppm Light: UV lamp	35% adsorbed and degraded at the same time in 120 min	6.5	(Xue & Zou, 2018)
Photochemical reduction	rGO: 10 mg [MB]: 10 ppm Light: 300 W Xe lamp	30% adsorbed and degraded at the same time in 120 min	7	(Xue & Zou, 2018)
Green reduction without toxic reductant	rGO: 60 mg [MB]: 50 ppm Light: 95 W UV lamp (x 2)	99% degraded in 6 hr after adsorption of 87% in 4 hr	0.1	This work

Chandra et al. (2012) demonstrated the use of rGO/Mn_2O_3 nanocomposite for direct removal of MB through photocatalysis. The photocatalytic performance of rGO towards elimination of MB was also examined under UV light illumination. It was revealed that the dye adsorption process on the surface of rGO might be the reason for causing a slight reduction in MB concentration.

Y. Zhao et al. (2014) fabricated rGO/WO_3 nanocomposite for the elimination of MB. The MB removal process was also conducted by using bare rGO sheets, which was electrochemically exfoliated from graphite electrode. The results showed that rGO was able to degrade about 40% of MB after adsorption when it was irradiated with UV light.

Shaohua Xu et al. (2015) employed rGO/ZnO composite to eliminate MB. As a control, rGO was also evaluated for its performance over MB adsorption and photodegradation reactions. Due to the large SSA of rGO, as well as its π-π conjugation with dye molecules, the MB adsorption process was able to occur. The concentration of dye was barely decreased after UV illumination.

Kaur et al. (2016) studied the MB removal process by using rGO/CeO_2 nanocomposite. The adsorption and photoactivity of rGO towards elimination of MB were also investigated. It was suggested that the π-π interactions between rGO and dye molecules might be the reason for the occurrence of dye adsorption process. When rGO was irradiated with sunlight, an insignificant degradation of MB was observed.

M. J. S. Mohamed & Bhat (2017) synthesized rGO/$ZnWO_4$ nanocomposite for MB adsorption and photodegradation reactions. The elimination of dye was also carried out by using rGO, which was used as a control sample. It was believed that the slight negative charge on the surface of rGO was the main reason for dye adsorption reaction. Under UV light, rGO could only degrade about 19% of MB.

Xue & Zou (2018) utilized rGO/ZnO nanocomposite to directly remove MB through photocatalysis. The photoactivity of bare rGO towards elimination of MB was also investigated. Under the irradiation of UV or visible light, MB was barely degraded by rGO. The slight removal of MB was said to be caused by the strong adsorption of MB on rGO sheets.

Kumbhakar et al. (2018) examined the MB adsorption and photodegradation reactions by using rGO/ZnO nanocomposite. The use of GO instead of rGO as a control in the experiment was also evaluated. After the adsorption process, it was found that GO could only degrade a small amount of MB under UV or visible light, which might be due to the rapid recombination of electrons and holes in GO.

CHAPTER 3: METHODOLOGY

3.1 Materials

Graphite powder (< 20.0 µm, synthetic), potassium peroxodisulphate ($K_2S_2O_8$, ≥ 99%), di-phosphorus pentoxide (P_2O_5, ≥ 99%), and ethanol (C_2H_5OH, ≥ 99.9%) were acquired from Merck. Sulphuric acid (H_2SO_4, ≥ 95-97%), potassium permanganate ($KMnO_4$, ≥ 99%), methylene blue (MB, C.I. 52015, ≥ 99%), hydrogen peroxide (H_2O_2, ≥ 30%), and hydrochloric acid (HCl, ≥ 37%) were purchased from Friendemann Schmidt. In all experiments, deionized water (DI water, 18.2 MΩ·cm) was utilized.

3.2 Pre-treatment of Graphite Powder

Pre-treatment of graphite powder was carried out to achieve a more efficient oxidation in later stage. In a typical process, 3 g of synthetic graphite powder was added into a solution of 12 mL of H_2SO_4, 2.5 g of P_2O_5, and 2.5 g of $K_2S_2O_8$ (C. Zhao et al., 2016). The mixture was stirred in an oil bath at 80 °C for 4.5 hours. Then, the mixture was removed from oil bath and gradually cooled to ambient temperature. The mixture was diluted slowly with 500 mL of DI water and left overnight. Subsequently, the mixture was filtered, washed with DI water to remove residual chemical substances, followed by drying in oven to obtain pre-treated graphite.

3.3 Preparation of Graphene Oxide (GO)

GO was fabricated from pre-treated graphite based on modified Hummers' method (Cheng et al., 2017). The pre-treated graphite powder was added into 120 mL of pure H_2SO_4 under vigorous stirring in an ice bath. Then, 15 g of $KMnO_4$ was gradually added into the mixture and the temperature was maintained at 35 °C for 2 hours. The mixture was stirred for another 2 hours with the addition of 250 mL of DI water. Subsequently, 500 mL of DI water was added into the mixture, followed by 20 mL of 30% H_2O_2 solution to terminate the reaction. The mixture was centrifuged and washed with 10% (v/v) HCl solution, followed by DI water to remove residual chemical substances. After that, GO was subjected to drying and grinding procedures to obtain graphite oxide.

3.4 Preparation of Reduced Graphene Oxide (rGO)

rGO was obtained from reduction of GO by using an eco-friendly solvothermal method. In a typical process, 200 mg of graphite oxide powder was added into 20 mL of C_2H_5OH and 10 mL of DI water. The mixture was thoroughly sonicated for 30 minutes to produce stable GO dispersion. Subsequently, the homogeneous mixture of GO was transferred into an 80 mL Teflon-lined stainless steel autoclave and heated in oven according to the synthesis conditions as described in 3.4.1 and 3.4.2. The autoclaved mixture was then subjected to vacuum filtration, and the resulting rGO was rinsed with DI water to remove remaining ethanol and impurities. Finally, rGO was dried in oven prior to use.

3.4.1 Effect of Reaction Temperature

GO was subjected to different heating temperatures (80, 120, 160 and 180 °C) at a constant duration of 2 hours to investigate the effect of reaction temperature on GO reduction. The rGO samples were denoted as rGO-80, rGO-120, rGO-160 and rGO-180.

3.4.2 Effect of Reaction Duration

GO was subjected to different heating durations (1, 2, 4 and 8 hours) at an isothermal condition of x °C to determine the effect of reaction duration on GO reduction. The x

represents the optimum temperature obtained in 3.4.1, and the rGO samples were indicated as rGO-x_1, rGO-x_2, rGO-x_4 and rGO-x_8.

3.5 Methods of Characterization

GO and rGO were characterized by using various analytical techniques. Raman spectroscopy was carried out to determine their ordered and disordered structures. Energy dispersive X-ray (EDX) spectroscopy was performed to find out their elemental compositions. X-ray diffraction (XRD) was conducted to investigate their crystalline phases. Brunauer-Emmett-Teller (BET) and Barrett-Joyner-Halenda (BJH) analyses were carried out to measure their SSAs, pore sizes, and TPVs. Ultraviolet-visible (UV-Vis) spectrophotometry was performed to reveal their optical properties.

3.5.1 Raman Spectroscopy

Raman spectroscopy is a fast, non-destructive, and high-resolution tool for characterization of carbon materials and their structural disorders. Generally, the analysis of samples is carried out in their original states without involving any specific preparation steps. In this case, a small amount of as-prepared GO/rGO sample was deposited on a glass microscope slide and put under microscope. Then, the analysis was performed by using Renishaw inVia Raman Microscope (Gloucestershire, UK) over a scan range of 100-3200 cm^{-1}. The laser excitation source used was 514 nm Ar-ion laser. In Raman spectroscopy, the instrumentation primarily consists of a laser source, light collection optics, a wavelength selector and a detector. When a monochromatic laser beam hits the sample and interacts with the molecules of sample, a scattered light is produced. Usually, the scattered light comprises mostly of Rayleigh scattering, whereas only a small fraction of it is made up of Raman scattering. The Raman scattered photons are then collected by light collection optics and filtered by wavelength selector, before being read by detector and showed as a spectrum on computer (Vandenabeele, 2013).

3.5.2 Energy Dispersive X-Ray (EDX) Spectroscopy

EDX is an analytical technique used to determine the elemental compositions of solid materials. In this study, as-synthesized GO/rGO sample was sprinkled lightly with a spatula on top of a sample stub attached with a double-sided carbon tape to mount the sample. Then, the sample stub was turned upside down and tapped to remove the unmounted sample, before being transferred into the sample chamber of FEI Quanta FEG 650 Environmental Scanning Electron Microscope (Oregon, USA) combined with an Oxford Instruments INCA EDX Spectrometer (Oxford, UK) for elemental composition analysis. The EDX measurement was conducted at an accelerating voltage of 20 kV and a spot size of 4 under high vacuum mode. Generally, EDX is composed of three basic components: a detector, a pulse processor and a multi-channel analyzer. When an electron beam excites an electron in the lower-energy inner shell of a sample, the electron is ejected from the shell, creating a vacancy. Then, an electron from a higher-energy outer shell falls to fill the vacancy. The difference in energy between the outer and inner shells is emitted in the form of an X-ray, which is then converted into a voltage signal of proportional size. Lastly, the pulse processor measures the signal and passes it onto a multi-channel analyzer for data display and analysis (Goldstein et al., 2017).

3.5.3 X-Ray Diffraction (XRD)

XRD is a useful and non-destructive method for analyzing the structures, phases, sizes, orientations, degree of crystallinity, and lattice defects of crystalline materials. In this study, as-fabricated GO/rGO sample was ground into fine powder and packed into a sample holder. Then, the sample holder was placed in the sample stage of PANalytical Empyrean X-ray Diffractometer (Almelo, Netherlands) equipped with Cu Kα ($\lambda = 1.5406$ Å) radiation to begin analysis. The XRD measurement was carried out at a scan rate of $0.02°\cdot s^{-1}$ over a 2θ range of 10-70° under 40 kV/30 mA. In XRD, the basic elements include an X-ray tube, a sample holder and a detector. Upon heating the filament in an X-ray tube, electrons are induced and accelerated towards a target material (Cu, Fe, Mo, Cr) by applying a voltage. When the target material is bombarded by electrons with sufficient energy, the inner-shell electrons of target material are dislodged. The outer-shell electrons then lose energy by emitting X-rays to fill the vacancies. The X-rays are filtered by a crystal monochromator or foils to produce monochromatic X-rays, which are then aligned and directed onto the sample. Subsequently, the intensity of reflected X-rays is recorded, processed and converted to a count rate by a detector, before being outputted to monitor as a diffractogram (N. Kumar & Kumbhat, 2016).

3.5.4 Surface Area and Porosity Analysis

BET and BJH analyses are widely employed to determine the SSA and pore size distribution of porous materials, respectively. In this study, Micromeritics ASAP 2020 Surface Area and Porosity Analyzer (Georgia, USA) was used to conduct such analyses. Basically, the instrument has two main ports: a degas port and an analysis port. Prior to analysis, as-manufactured GO/rGO sample was first filled into a sample tube, sealed with a seal frit, and attached to a degas port for degassing. The sample was heated at 150 ºC for 24 hours under vacuum condition to remove moisture and other contaminants from the surface. Subsequently, the sample tube was removed from the degas port and transferred to an analysis port. During the transfer, the seal frit was not removed from sample tube to avoid sample contamination. Then, the analysis began by gradually introducing N_2 at a constant temperature of 77 K up to its saturation pressure, followed by slowly removing it with vacuum to measure the quantity of N_2 adsorbed. The data obtained were then utilized by BET and BJH models to calculate the SSA and pore size distribution of sample, respectively (Thommes et al., 2015).

3.5.5 Ultraviolet-Visible (UV-Vis) Spectroscopy

UV-Vis spectroscopy is a non-destructive technique used to characterize the optical properties of materials. In this study, a small amount of as-synthesized GO/rGO sample was first dispersed completely in DI water via ultrasonication bath. Then, the sample dispersion was added to a cuvette, and placed in a cuvette holder of Perkin Elmer Lambda 35 UV/Vis Spectrophotometer (Massachusetts, USA) to begin analysis. The UV-Vis measurement was conducted over an absorption range of 200-800 nm. In UV-Vis, the major components include a light source, a monochromator, a sample compartment and a detector. Generally, a deuterium lamp is used as the light source for ultraviolet region, whereas for visible region, a tungsten filament lamp is utilized instead. When a light passes through a monochromator, it is split into two equal beams that take parallel but separate paths through a sample compartment. There are two cuvette holders in the sample compartment, one to hold the blank and another one to simultaneously hold the sample being measured. The beam that passes through the blank is known as “reference beam”, whereas the other beam that passes through the sample is called “sample beam”. A detector then measures the intensity of transmitted light, which is subsequently processed and presented as a spectrum on computer screen (Pavia et al., 2014). The band gap of sample was determined by using the Tauc’s relation as given below:

$$\alpha hv = \mathrm{A}\left(hv - \mathrm{E_g}\right)^{\gamma} \qquad \textbf{(3.1)}$$

where α is adsorption coefficient, hv is photon energy, A is constant, Eg is band gap energy and γ = ½. The x-axis intersection point of linear fit of the Tauc plot gives an estimate of the band gap of sample.

3.6 Adsorption and Photoactivity Measurements

GO and rGO were evaluated for MB adsorption and photodegradation processes. In a typical process, an appropriate amount of GO/rGO was added into a 100 mL of MB solution, aerated and stirred at a speed of 700 rpm in the dark until adsorption-desorption equilibrium was achieved. Then, the mixture was irradiated with 95 W UV-C light in a custom-made photoreactor at 25 °C to initiate the photodegradation reaction, as depicted in Figure 3.1. At regular time intervals, an aliquot was withdrawn and filtered to separate GO/rGO from the aliquot. The filtrates were then subjected to UV-Vis analysis to determine the remaining MB concentration. The MB adsorption percentage and photodegradation efficiency were calculated accordingly by using the formulae given below:

$$\%\ \text{Adsorbed} = \frac{\mathrm{C}_{initial} - \mathrm{C}_0}{\mathrm{C}_{initial}} \times 100\% \qquad \textbf{(3.2)}$$

$$\%\ \text{Degraded} = \frac{\mathrm{C}_0 - \mathrm{C}_t}{\mathrm{C}_0} \times 100\%\ , 0 \leq t \leq 6 \qquad \textbf{(3.3)}$$

where $\mathrm{C}_{initial}$, C_0 and C_t are respective MB concentrations at initial, after reaching adsorption-desorption equilibrium, and at time, *t*. Subsequently, kinetic study was conducted to determine the order of MB photodegradation reaction. Typically, pseudo-first-order kinetics is the most widely employed kinetic model to describe the kinetics of heterogeneous photocatalysis (Ma et al., 2013). Such kinetics is commonly expressed as below:

$$ln\left(\frac{C_0}{C_t}\right) = kt\,, 0 \leq t \leq 6 \qquad \textbf{(3.4)}$$

where k (h^{-1}) denotes the apparent reaction rate constant and is equal to the slope of fitting line.

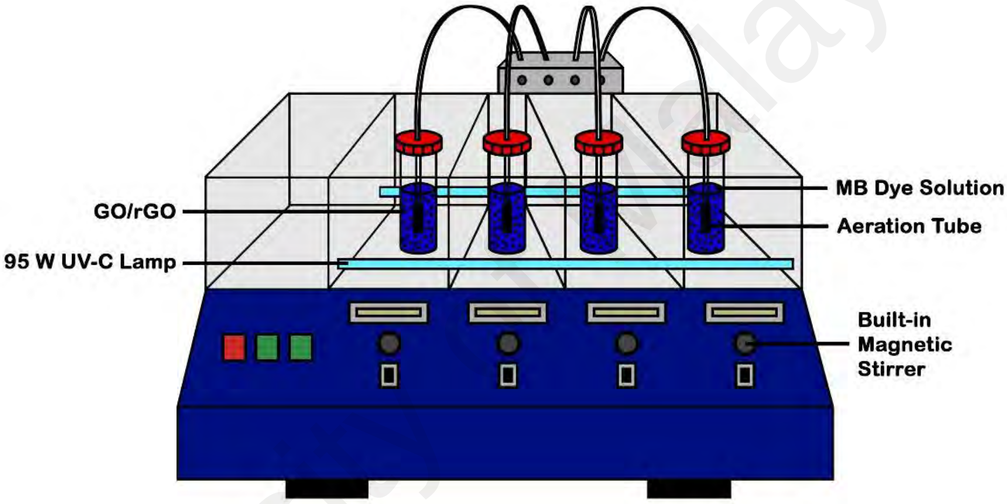

Figure 3.1. A schematic diagram of a custom-made UV photocatalytic reactor.

3.6.1 Effect of Catalyst Loading

In order to avoid wastage of catalyst and also to ensure maximum absorption of photons emitted from UV light source, different loadings (10, 20, 30, 40, 50, 60 and 70 mg) of optimum rGO sample were investigated, while initial dye concentration, light intensity, and pH of solution were kept constant throughout the experiment.

3.6.2 Effect of Initial Dye Concentration

It is known that initial dye concentration plays an important role on dye adsorption and photodegradation rate. Thus, different initial dye concentrations (50, 75, 100 and 125 ppm) were examined. The optimum catalyst dosage (from 3.6.1), light intensity, and initial pH of dye solution were remained constant at all time.

3.6.3 Effect of Light Intensity

It is worth to mention that photodegradation rate is highly affected by light intensity. In this study, the light intensity depends on the quantity of 95 W UV lamps used. Hence, the usage of single (30 $W{\cdot}m^{-2}$) and double (60 $W{\cdot}m^{-2}$) 95 W UV lamps was investigated, while the optimum catalyst loading (from 3.6.1), optimum initial dye concentration (from 3.6.2), and pH of solution were remained constant throughout the experiment.

3.6.4 Effect of pH

The initial pH of dye solution is also one of the most important factors influencing dye adsorption and photodegradation rate. In this study, the original dye solution had a pH = 6. Then, the value was either adjusted to pH = 3 by adding an appropriate amount of 0.01 M HCl to create a more acidic condition, or pH = 11 by adding a suitable amount of 0.01 M NaOH to form a more alkaline condition. Subsequently, the three different initial pH values (pH = 3, 6, 11) of dye solution were investigated for their effects on the performance of optimum rGO sample. The optimum catalyst dosage (from 3.6.1), optimum initial dye concentration (from 3.6.2), and optimum light intensity (from 3.6.3) were kept constant at all time.

3.6.5 Recyclability Test

The recyclability of a photocatalyst is deemed as a crucial factor from perspective of practical applications. Under optimum operational conditions, the stability and reusability of optimum rGO sample towards MB photodegradation process were determined by repeating the reaction for up to five cycles.

CHAPTER 4: RESULTS AND DISCUSSION

4.1 Effect of Reaction Temperature

4.1.1 Characterization Results

Raman analysis was carried out to examine the effect of reaction temperature on the ordered and disordered structures of GO and rGO samples. Figure 4.1 depicts the Raman spectra of GO and different rGO samples obtained at various reduction temperatures. Two prominent characteristic peaks of graphene, namely D (~1353 cm^{-1}) and G (~1591 cm^{-1}) bands were observed in all samples. D band is related to the A_{1g} breathing mode of graphitic aromatic rings (Georgakilas et al., 2015). It was occurred when structural defects were introduced into the samples (Morais et al., 2016). Besides that, D band was gradually red-shifted with increasing reduction temperature, which might be due to the average size reduction of in-plane sp^2 domains brought about by removal of OFGs from the surface (Dave et al., 2015). G band reflects the hexagonal structure associated with E_{2g} vibration mode of sp^2 carbon atoms (C. Liu et al., 2015). The intensity of G band was higher than that of D band, which suggested that the samples were not entirely exfoliated (Ali et al., 2017). The intensity ratio of these bands, I_D/I_G, measures the degree of disorder in the samples (Fan et al., 2010). Table 4.1 summarizes the I_D/I_G values of GO and rGO samples. The I_D/I_G ratio of GO is the lowest as compared to the rGO samples. As the reduction temperature increased from 80 °C to 180 °C, the I_D/I_G ratio was also increased, which signified an increasing trend of reduction degree (Tan et al., 2014). During the reduction process, the surficial OFGs were gradually being removed, thereby creating more defects (Tai et al., 2019). Apart from D and G bands, the other two bands with lower intensities, which are associated with 2D (~2684 cm^{-1}) and S3 (~2935 cm^{-1}) bands, were also observed. 2D band, with its frequency nearly double that of D band, is related to the second-order Raman scattering process that involves two phonons with opposite momentum, whereas S3 band corresponds to the imperfect activated grouping of phonons

(Z. Li et al., 2016). It was found that the intensities of the two bands were slightly increased with increasing reduction temperature, indicating a better graphitization degree (P. Cui et al., 2011).

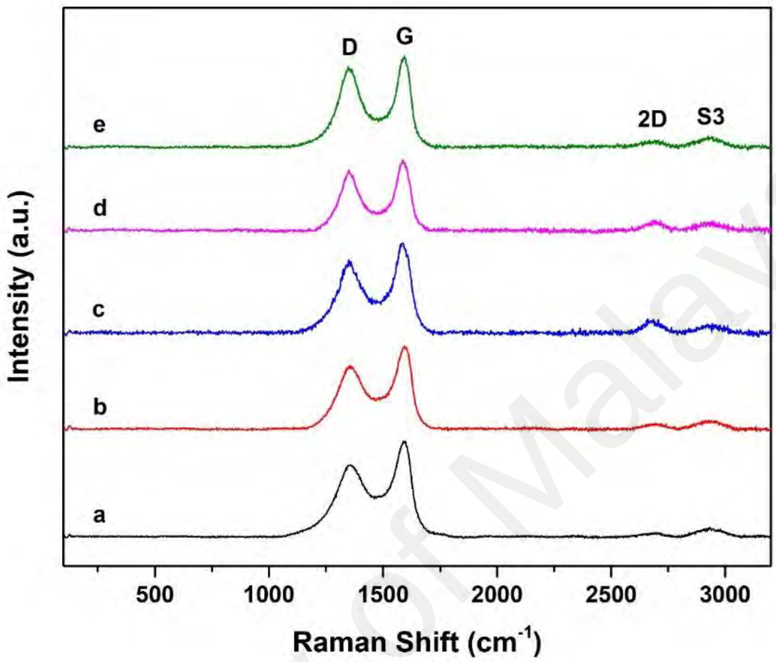

Figure 4.1. Raman spectra of (a) GO, (b) rGO-80, (c) rGO-120, (d) rGO-160, and (e) rGO-180.

Table 4.1. I_D/I_G values of GO, rGO-80, rGO-120, rGO-160 and rGO-180.

Sample	D band (cm^{-1})	G band (cm^{-1})	I_D/I_G
GO	1357	1598	0.7514
rGO-80	1355	1593	0.7678
rGO-120	1350	1587	0.8100
rGO-160	1350	1587	0.8523
rGO-180	1348	1593	0.8791

EDX analysis was conducted to investigate the effect of reaction temperature on the elemental compositions of GO and rGO samples. Figure 4.2 shows the SEM images and corresponding EDX spectra of GO and representative rGO-160 samples. In general view, the SEM images revealed the transition of GO to rGO when GO was reduced at 160 °C. The elemental compositions of GO and rGO-160 samples are depicted in Table 4.2. For both samples, only C and O elements were detected. As compared to rGO-160, the C/O atomic ratio of GO was lower at 1.79, which implied that higher oxygen content was present in GO. The value is comparable to the findings obtained in previous GO studies (AlShammari et al., 2019; Phukan et al., 2019). After GO was solvothermally reduced at a higher temperature of 160 °C, the C/O atomic ratio was found to increase tremendously, owing to its reduced oxygen content (AlShammari et al., 2019; Phukan et al., 2019). The EDX results were in agreement with the Raman data presented, whereby higher reduction temperature led to higher degree of GO reduction.

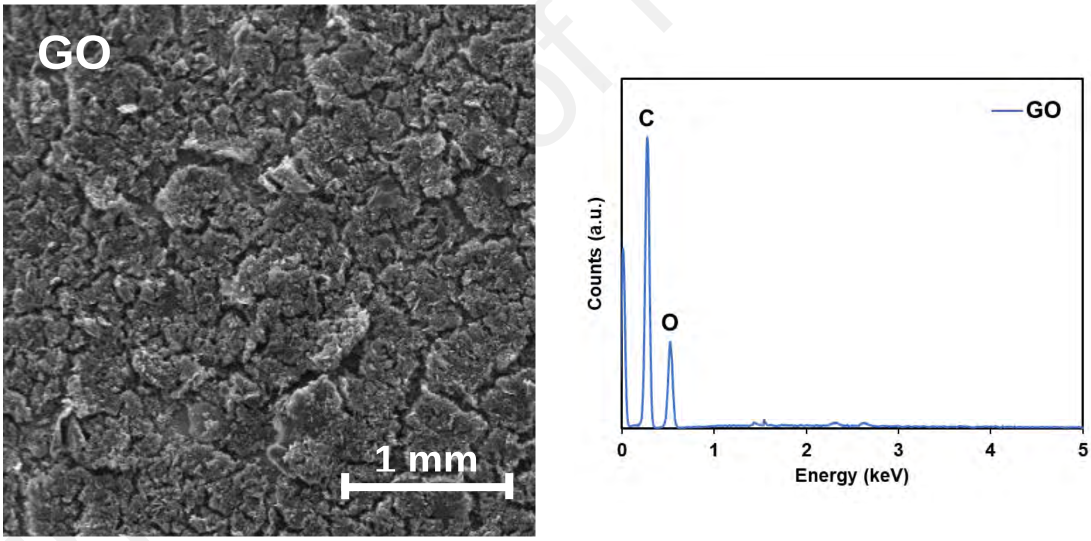

(A)

Figure 4.2, continued

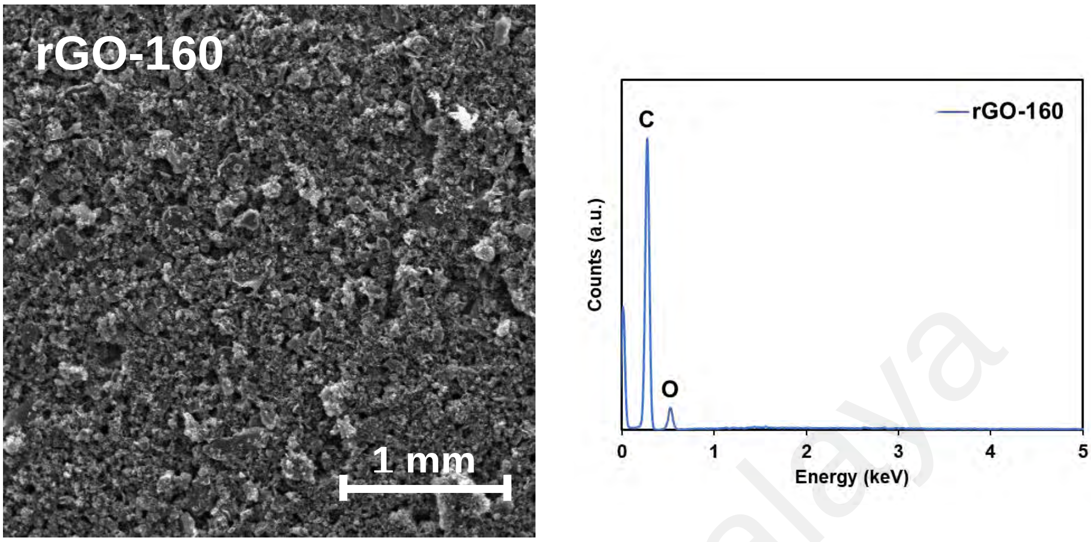

(B)

Figure 4.2. (A) SEM image and corresponding EDX spectrum of GO, **(B)** SEM image and corresponding EDX spectrum of rGO-160.

Table 4.2. Elemental compositions of GO and rGO-160.

Sample	C (Atomic %)	O (Atomic %)	C/O
GO	64.22	35.78	1.79
rGO-160	80.24	19.76	4.06

XRD analysis was carried out to examine the effect of reaction temperature on the crystalline phases of GO and rGO samples. Figure 4.3 illustrates the XRD patterns of graphite, GO and different rGO samples obtained at various reduction temperatures. Graphite showed a strong and sharp (002) peak at $2\theta = 26.57°$, and a very small (101) peak at $2\theta = 54.70°$. Both peaks confirmed the graphitic structure and are in agreement with the data showed in JCPDS card of 41-1487 (Fathy et al., 2016). Upon oxidation, the (002) peak was shifted to $2\theta = 11.03°$, which was attributed to the intercalation of OFGs and water molecules into the carbon layer structure (Loryuenyong et al., 2013).

Nevertheless, the (002) peak of GO was still visible after GO was reduced at 80 °C and 120 °C, possibly due to lower reduction temperatures, which mildly reduced GO to rGO. As the reduction temperature increased, the (002) peak of GO started to disappear while a new broader (002) peak of rGO began to emerge at $2\theta = 24.89°$ for rGO-160 and $2\theta = 23.85°$ for rGO-180. The shifting of (002) peak signified the partial restoration of graphitic structure (Pavoski et al., 2017). When comparing rGO-160 and rGO-180 with graphite, both rGO samples exhibited broader and weaker (002) peaks due to incomplete stacking of graphene sheets (He & Fang, 2016). For GO, (100) peak was observed at $2\theta = 42.63°$. However, the same peak was also detected at around the same location for rGO samples, which reflected the turbostratic band of disordered carbon materials (Emiru & Ayele, 2017).

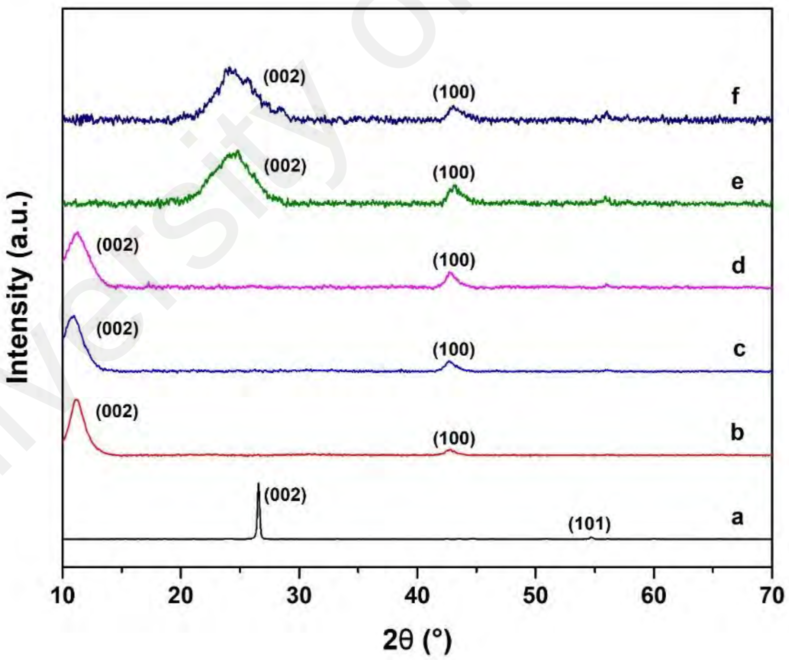

Figure 4.3. XRD patterns of (a) Graphite, (b) GO, (c) rGO-80, (d) rGO-120, (e) rGO-160, and (f) rGO-180.

The nitrogen adsorption-desorption isotherms of GO and different rGO samples obtained at various reduction temperatures are showed in Figure 4.4A. According to the latest IUPAC classification that was adapted by Thommes et al. (2015), all samples were found to follow a type II curve for their nitrogen adsorption-desorption isotherms, along with a hysteresis loop of type H3. At lower relative pressures ($P/P_0 < 0.1$), there was a gradual increase in the amount of N_2 adsorbed, denoting the occurrence of micropore filling for all samples. The adsorption of N_2 then increased following a rise in relative pressure, which indicated the transition of monolayer to multilayer adsorption process in all samples except for GO, rGO-80 and rGO-120, which contained mesopores that were poorly developed. At higher relative pressures ($P/P_0 > 0.9$), a considerable amount of N_2 was adsorbed on all samples as macropores were present in them. A slope was detected in the desorption curve of each loop, which was attributed to the tensile strength effect originated from the instability of meniscus during capillary condensation process (ALOthman, 2012). The hysteresis loops of GO, rGO-80 and rGO-120 were completely closed, however, the hysteresis loops of rGO-160 and rGO-180 were partially closed and stopped at around $P/P_0 = 0.45$, which could be attributed to the presence of a larger amount of micropores in the samples (Moussa et al., 2016).

The corresponding pore size distribution curves and textural parameters of GO and rGO samples are displayed in Figure 4.4B and Table 4.3, respectively. When GO was reduced from 80 °C to 120 °C, the TPV decreased from 0.085 to 0.037 $cm^3 \cdot g^{-1}$, thus leading to a reduction of SSA. This was probably due to the agglomeration effect of GO upon reduction (I. Chowdhury et al., 2015; Su et al., 2018). A pronounced increment of SSA was then observed for rGO-160 at higher reduction temperature, owing to the significant removal of OFGs, causing the generation of higher TPV (Srinivas et al., 2012; B. Zhao et al., 2012). However, when the reduction temperature was increased to 180 °C, the rGO sheets tended to stack together via π-π interactions, resulting in decreased SSA of rGO-180 (Morimoto et al., 2016). Both rGO-160 and rGO-180 exhibited much smaller pore sizes and higher TPVs as compared to other samples. The measured SSAs of both rGO-160 and rGO-180 were far below than the theoretical value (2630 $m^2 \cdot g^{-1}$) of fully exfoliated pristine graphene, possibly due to incomplete exfoliation (Yu et al., 2018).

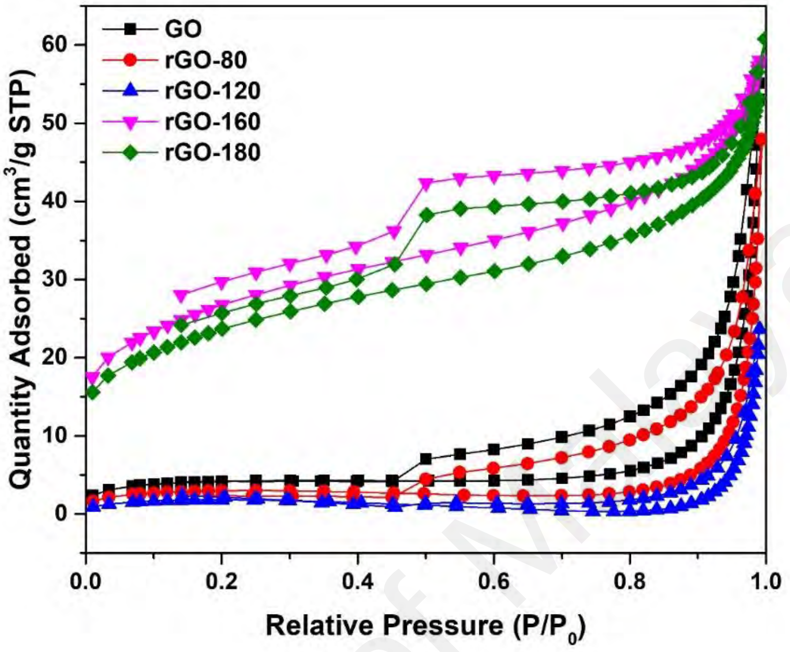

(A)

Figure 4.4, continued

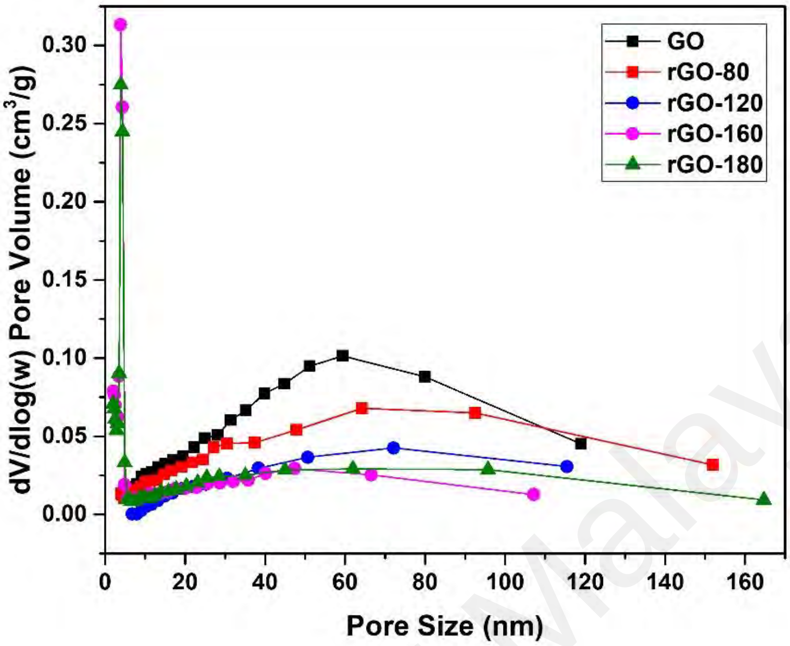

(B)

Figure 4.4. (A) Nitrogen adsorption-desorption isotherms of GO, rGO-80, rGO-120, rGO-160, and rGO-180, **(B)** pore size distributions of GO, rGO-80, rGO-120, rGO-160, and rGO-180.

Table 4.3. BET/BJH textural parameters of GO, rGO-80, rGO-120, rGO-160 and rGO-180.

Sample	Surface area ($m^2 \cdot g^{-1}$)	Pore size (nm)	Pore volume ($cm^3 \cdot g^{-1}$)
GO	15.03	59.42	0.085
rGO-80	10.76	64.19	0.074
rGO-120	6.67	72.18	0.037
rGO-160	94.81	3.89	0.118
rGO-180	83.81	3.90	0.094

UV-Vis analysis was accomplished to elucidate the optical properties of GO and rGO samples. Figure 4.5A depicts the UV-Vis absorption spectra of GO and different rGO samples obtained at various reduction temperatures. GO displayed a maximum absorption peak at 231 nm, which was attributed to the π-π* electronic transition of aromatic C=C bonds (Pham et al., 2010; Shengjie Xu et al., 2013). When GO was reduced from 80 °C to 180 °C, it was observed that the peak position slowly shifted to 268 nm. The red shift of absorption peak signified the partial restoration of sp^2 conjugation, thereby reducing band gap of GO (Saxena et al., 2011). The optical band gaps of GO and rGO samples were then determined from linear fits of the Tauc plots, as showed in Figure 4.5B and Table 4.4. The band gap of GO was estimated to be 3.00 eV, which is in good agreement with existing literature reports (Hsu et al., 2013; P. Kumar et al., 2014; Zhang et al., 2013). The band gap then decreased to about 2.82 eV when GO was reduced up to 160 °C. Generally, the band gap of GO is proportional to amount of oxygen atoms present (F. Li et al., 2015; Lian et al., 2013). Hence, the removal of surficial OFGs contributed to band gap reduction of GO. Nevertheless, the value was slightly increased to around 2.87 eV when the reduction temperature increased to 180 °C, possibly due to higher density of structural defects and restacking of rGO sheets (Ameer et al., 2015; De et al., 2014; Some et al., 2013).

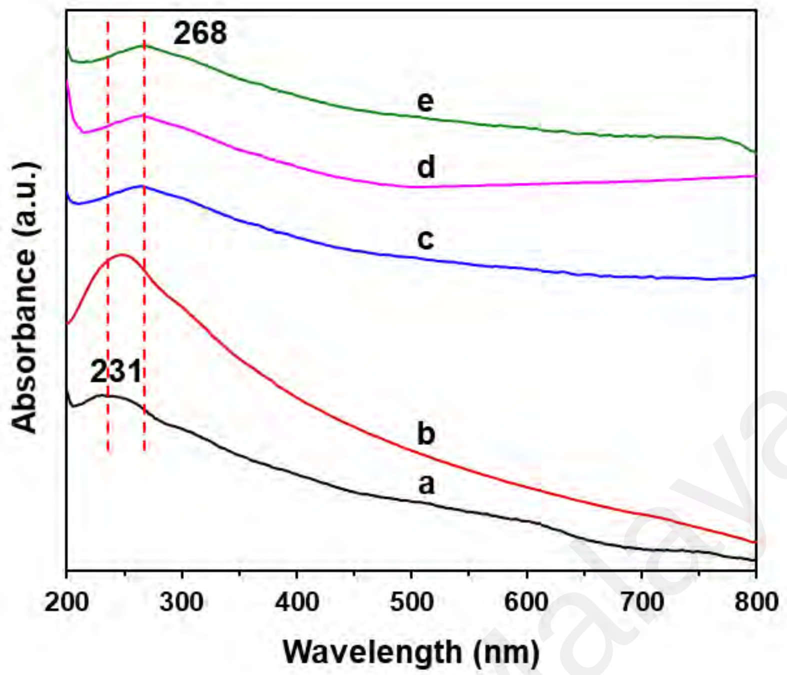

(A)

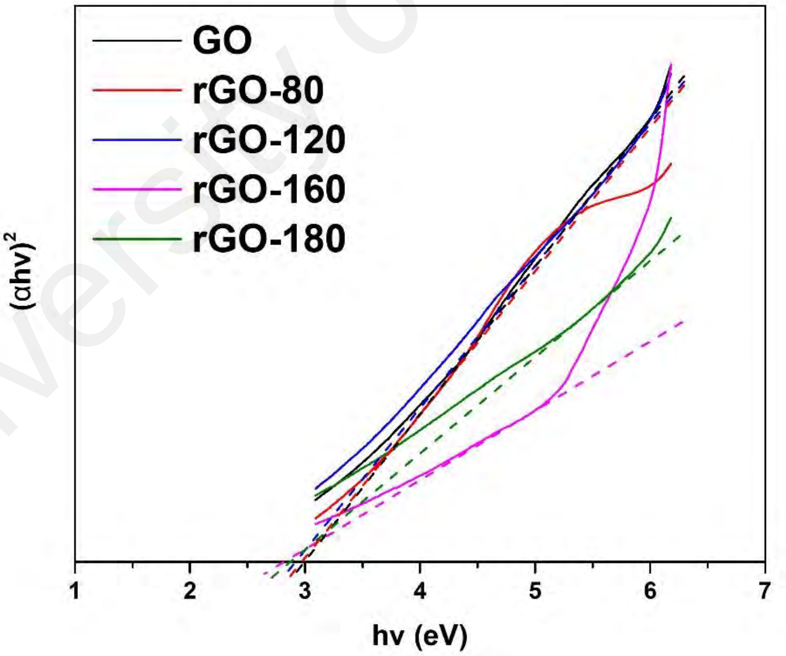

(B)

Figure 4.5. (A) UV-Vis absorption spectra of (a) GO, (b) rGO-80, (c) rGO-120, (d) rGO-160, and (e) rGO-180, **(B)** Tauc plots of GO, rGO-80, rGO-120, rGO-160, and rGO-180.

Table 4.4. Optical band gaps of GO, rGO-80, rGO-120, rGO-160, and rGO-180.

Sample	Band gap (eV)
GO	3.00
rGO-80	2.97
rGO-120	2.92
rGO-160	2.82
rGO-180	2.87

4.1.2 Adsorption and Photoactivity Measurements

Figure 4.6 illustrates the MB removal process by photolysis. The experimental conditions were fixed at 50 ppm (initial dye concentration), double 95 W UV lamp (light intensity), and pH = 6 (initial pH of dye solution). In the absence of rGO photocatalysts, it was found that only 7.9% of MB was removed. The slight removal of dye was due to photolysis effect, whereby similar results were also reported in previous studies (Akin & Oner, 2013; Mansur et al., 2014).

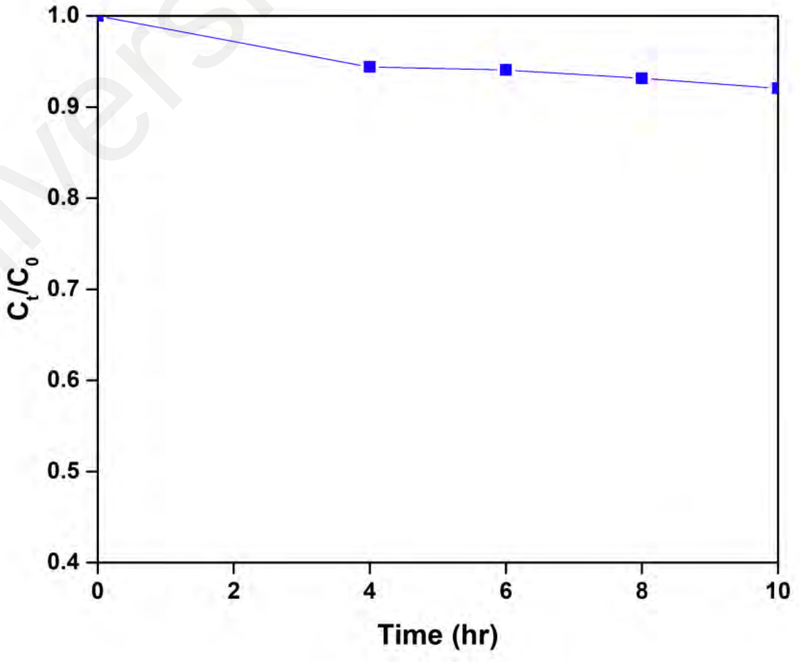

Figure 4.6. MB removal by photolysis.

In order to determine the optimum temperature for GO reduction, the MB adsorption and photodegradation of rGO photocatalysts were evaluated. Throughout the experiments, the experimental conditions were fixed at 20 mg (catalyst loading), 50 ppm (initial dye concentration), double 95 W UV lamp (light intensity), and pH = 6 (initial pH of dye solution). Figure 4.7A shows the plot of $C_t/C_{initial}$ versus time for GO and different rGO samples obtained at various reduction temperatures, and the corresponding results are summarized in Table 4.5. During the adsorption period, declining trends were observed, indicating that dye molecules had adsorbed on the surface of samples. The appropriate adsorption-desorption equilibrium between dye molecules and samples was established after stirring for 4 hours under dark condition (Appendix A). Since lower reduction temperatures were insufficient for GO reduction, both rGO-80 and rGO-120 behaved more or less like GO in dye adsorption reaction as compared to other rGO samples. Although the SSA of GO was higher than that of rGO-80 and rGO-120, the lower percentage of MB adsorption over GO could possibly be caused by weaker π-π interactions of dye molecules and unoxidized aromatic regions of GO (J. Wang et al., 2014). With a large SSA, rGO-160 was able to attain the highest percentage of MB adsorption. When the reduction temperature was increased to 180 °C, there was a slight decrease in adsorption efficiency due to SSA reduction. During the photocatalysis period, every sample also revealed a decreasing trend, suggesting that MB photodegradation process had taken place. As the energy of light irradiated was higher than the band gaps of GO and rGO samples, electron-hole pairs were able to be generated, thereby providing ROS to break down dye molecules. Similar to GO, both rGO-80 and rGO-120 also demonstrated lower photodegradation efficiencies than other rGO samples. The highest MB photodegradation efficiency was then achieved by rGO-160. It was suggested that the dye molecules could interact better with ROS when they were adsorbed on catalyst surface rather than moving freely in aqueous solution (S. He et al., 2018). Hence, the more dye molecules adsorbed on surface, the greater interaction with ROS, and the higher photodegradation efficiency. As rGO-180 exhibited smaller SSA than rGO-160, the available contact area for photodegradation reaction was also decreased.

Figure 4.7B demonstrates the linear relationships of ln(C_0/C_t) versus irradiation time. Since all samples exhibited high correlation coefficients of $R^2 \geq 0.95$ except rGO-80, the photodegradation reactions were said to obey pseudo-first-order kinetics. Based on Table 4.5, the highest rate constant was achieved by rGO-160, which is well agreed with the highest photodegradation efficiency reported. Hence, rGO-160 was selected to study the effect of reaction duration on MB adsorption and photodegradation reactions.

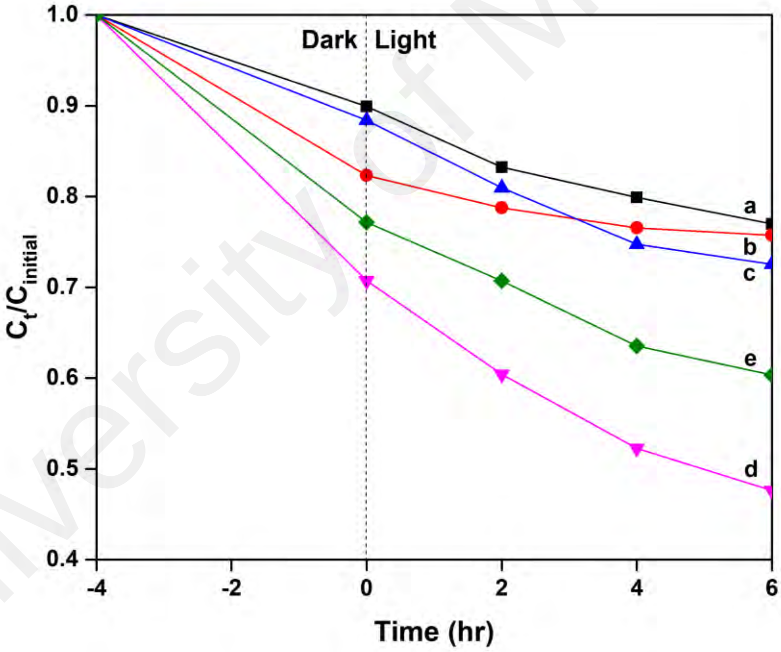

(A)

Figure 4.7, continued

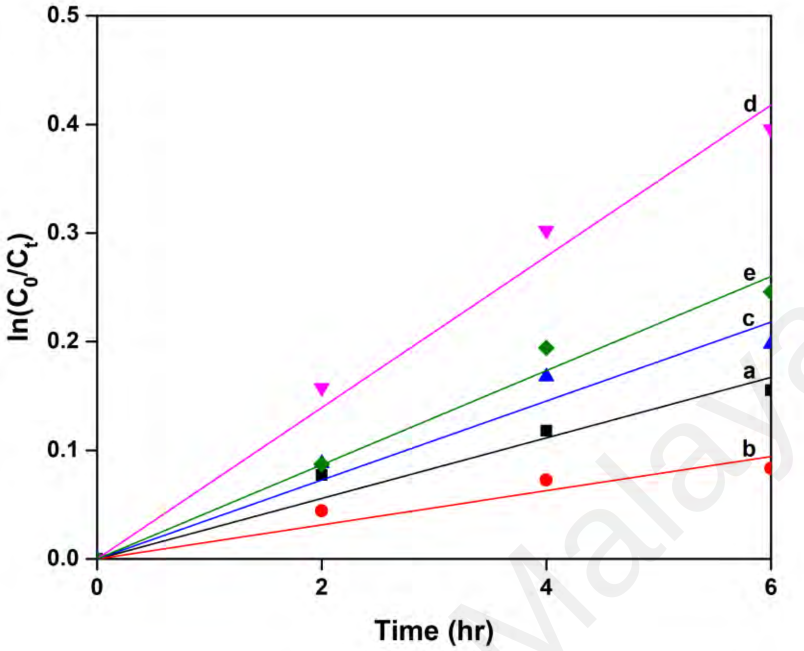

(B)

Figure 4.7. (A) MB adsorption and photodegradation of (a) GO, (b) rGO-80, (c) rGO-120, (d) rGO-160, and (e) rGO-180, **(B)** a linear plot of MB photodegradation in the presence of (a) GO, (b) rGO-80, (c) rGO-120, (d) rGO-160, and (e) rGO-180.

Table 4.5. Effect of reaction temperature on adsorption percentage, photodegradation efficiency, and photodegradation rate of MB dye.

Sample	Adsorption Percentage (%)	Photodegradation Efficiency (%)	k (h^{-1})	R^2
GO	10.07	14.41	0.028	0.9517
rGO-80	17.67	8.00	0.016	0.9075
rGO-120	11.60	17.96	0.036	0.9516
rGO-160	29.26	32.68	0.070	0.9844
rGO-180	22.83	21.80	0.043	0.9823

4.2 Effect of Reaction Duration

4.2.1 Characterization Results

Raman analysis was conducted to examine the effect of reaction duration on the ordered and disordered structures of GO and rGO samples. Figure 4.8 shows the Raman spectra of GO and different rGO samples obtained at various reduction times. In all samples, both D (~1352 cm^{-1}) and G (~1590 cm^{-1}) bands were observed. The intensity of G band was slightly higher when comparing to that of D band, which signified the incomplete exfoliation of graphitic layers (Ali et al., 2017). The I_D/I_G values of GO and rGO samples are then tabulated in Table 4.6. Among all samples, GO depicted the lowest I_D/I_G ratio. The I_D/I_G ratio increased when the reduction time was extended from 1 hour to 8 hours, signifying an increase in degree of reduction (J. Wang et al., 2017). Furthermore, 2D (~2693 cm^{-1}) and S3 (~2936 cm^{-1}) bands were also detected in the Raman spectra of all samples, but with relatively weak intensities. As the reduction time was increased, the intensities of both bands also increased, indicating a better degree of graphitization (Moon et al., 2010).

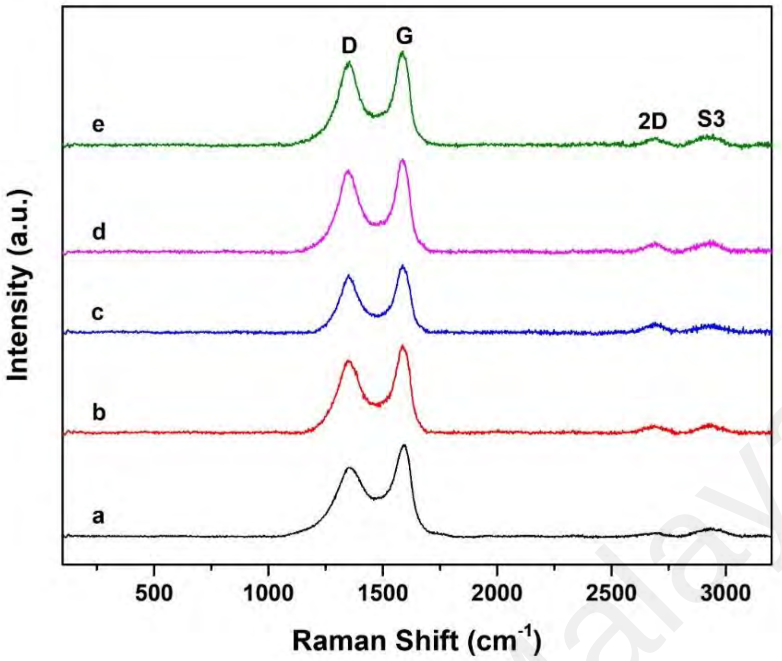

Figure 4.8. Raman spectra of (a) GO, (b) rGO-160$_1$, (c) rGO-160$_2$, (d) rGO-160$_4$, and (e) rGO-160$_8$.

Table 4.6. I_D/I_G ratios of GO, rGO-160$_1$, rGO-160$_2$, rGO-160$_4$, and rGO-160$_8$.

Sample	D band (cm^{-1})	G band (cm^{-1})	I_D/I_G
GO	1357	1598	0.7514
rGO-160$_1$	1348	1587	0.8270
rGO-160$_2$	1350	1587	0.8523
rGO-160$_4$	1353	1587	0.8681
rGO-160$_8$	1350	1591	0.8767

XRD analysis was performed to study the effect of reaction duration on the crystalline phases of GO and rGO samples. Figure 4.9 depicts the XRD patterns of graphite, GO and different rGO samples obtained at various reduction times. After an hour of GO reduction, a broad and diffuse (002) peak of rGO dominated the spectrum as it appeared at around 2θ = 24.79°, which indicated that reduction process had occurred. Nevertheless, it could be noticed that the (002) peak of GO was still present in diffraction pattern of rGO-160$_1$.

The peak became wider and less intense as compared to the (002) peak in diffraction pattern of GO due to the partial breakdown of long-range order in GO sample (H.-H. Huang et al., 2018). In addition to that, the peak also shifted towards a higher 2θ value of 11.30°. The simultaneous appearance of both peaks in diffraction pattern of rGO-160_1 denoted the incomplete reduction of GO to rGO. After 2 hours of GO reduction, the (002) peak of GO disappeared and only the (002) peak of rGO was detected in diffraction pattern of rGO-160_2. The peak, which was centered at $2\theta = 24.89°$, appeared to be taller and narrower as compared to the (002) peak of rGO in diffraction pattern of rGO-160_1, suggesting the partial restoration of sp^2 carbon structure (Hou et al., 2018). As the reduction time was extended to 4 hours and 8 hours, the (002) peak of rGO remained almost at the same angle position, indicating the maintenance of crystalline phase of rGO-160_2. On the other hand, the (100) peak of GO, which was located near $2\theta = 42.63°$, was also present in all rGO samples. The coexistence of both (002) and (100) peaks of rGO confirmed the rGO structure with reference to the data found in JCPDS card of 75-1621 (Shanmugam et al., 2015).

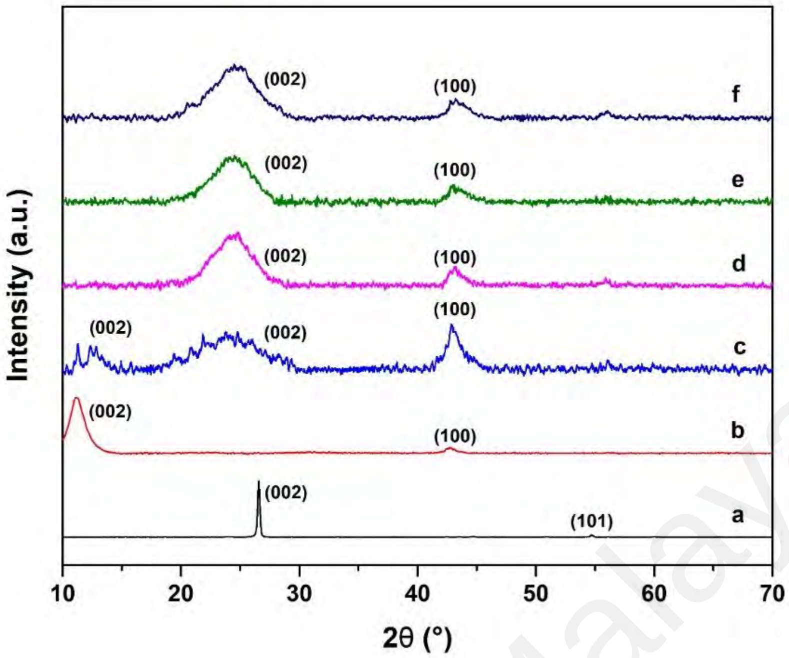

Figure 4.9. XRD patterns of (a) Graphite, (b) GO, (c) rGO-160_1, (d) rGO-160_2, (e) rGO-160_4, and (f) rGO-160_8.

Figure 4.10A illustrates the nitrogen adsorption-desorption isotherms of GO and different rGO samples obtained at various reduction times. Based on the most recent IUPAC classification by Thommes et al. (2015), the nitrogen adsorption-desorption isotherms of all samples belonged to type II, while their hysteresis loops revealed type H3. The adsorption of N_2 increased gradually for all samples at lower relative pressures ($P/P_0 < 0.1$), which indicated filling of micropores. As the relative pressure increased, the amount of N_2 adsorbed also increased, suggesting conversion of monolayer to multilayer adsorption process for all samples except for GO and rGO-160_1, which had poorly-developed mesopores. The adsorption of N_2 then increased tremendously for all samples at higher relative pressures ($P/P_0 > 0.9$), owing to the presence of macropores. In contrast to GO and rGO-160_1, the hysteresis loops of rGO-160_2, rGO-160_4, and rGO-160_8 were almost closed at about P/P_0 = 0.45, which was possibly due to larger quantity of micropores that were present in the samples (Moussa et al., 2016).

The pore size distribution curves and corresponding textural parameters of GO and rGO samples are showed in Figure 4.10B and Table 4.7, respectively. After GO was subjected to an hour of reduction, the TPV decreased from 0.085 to 0.029 cm^3·g^{-1}, thereby causing SSA to decrease. This was possibly due to agglomeration effect of GO upon reduction (I. Chowdhury et al., 2015; Su et al., 2018). Nevertheless, the SSA increased tremendously when the reduction time was prolonged for another hour. This was attributed to the significant removal of OFGs, which resulted in higher TPV (Srinivas et al., 2012; B. Zhao et al., 2012). When the reduction time was extended to 8 hours, the SSA gradually decreased, which could be explained by the partial overlapping of rGO sheets after prolonged period of reduction (Ossonon & Bélanger, 2017). As compared to GO and rGO-160$_1$, the pore sizes and TPVs of rGO-160$_2$, rGO-160$_4$, and rGO-160$_8$ were much smaller and higher, respectively. The measured SSAs of rGO-160$_2$, rGO-160$_4$, and rGO-160$_8$ were far below than the theoretical value (2630 m^2·g^{-1}) of fully exfoliated pristine graphene, probably due to incomplete exfoliation (Yu et al., 2018).

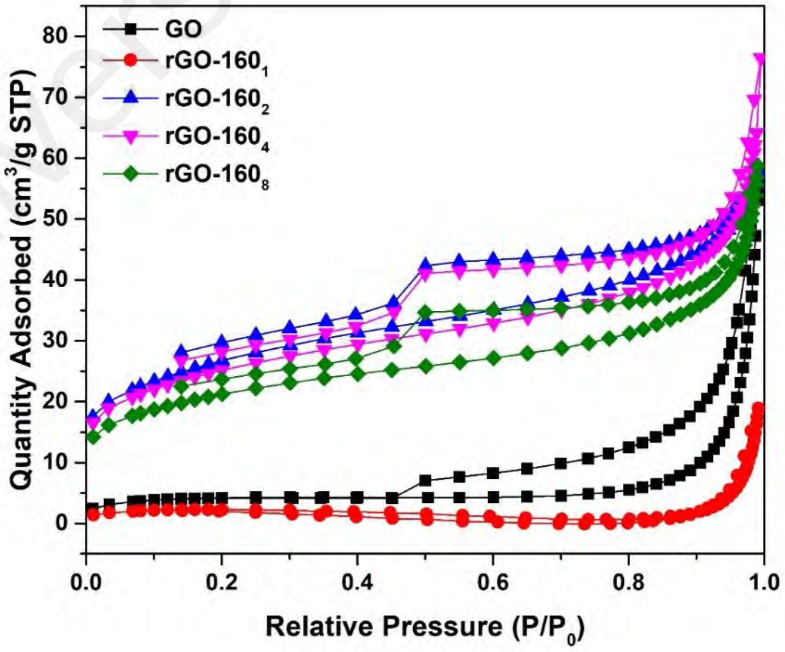

(A)

Figure 4.10, continued

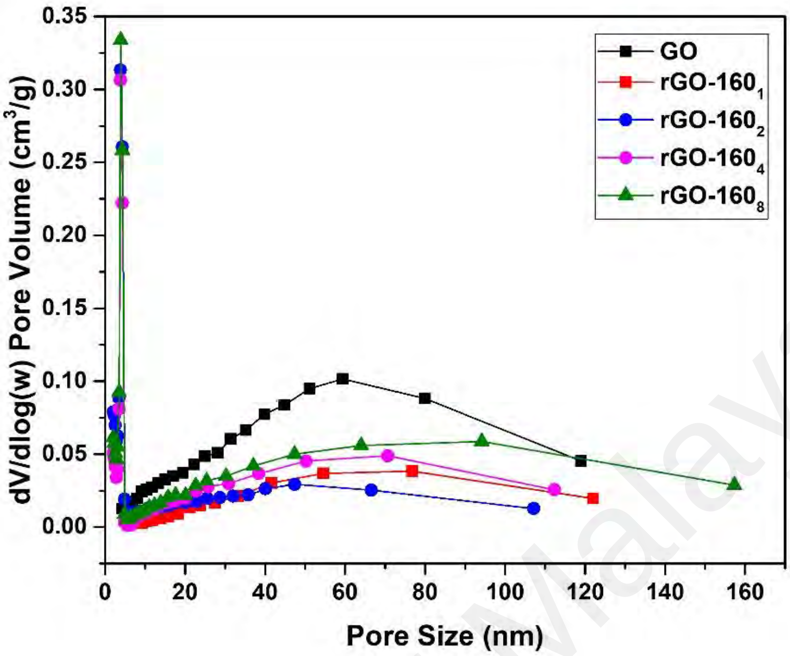

(B)

Figure 4.10. (A) Nitrogen adsorption-desorption isotherms of GO, rGO-160_1, rGO-160_2, rGO-160_4, and rGO-160_8, **(B)** pore size distributions of GO, rGO-160_1, rGO-160_2, rGO-160_4, and rGO-160_8.

Table 4.7. BET/BJH textural parameters of GO, rGO-160_1, rGO-160_2, rGO-160_4 and rGO-160_8.

Sample	Surface area ($m^2 \cdot g^{-1}$)	Pore size (nm)	Pore volume ($cm^3 \cdot g^{-1}$)
GO	15.03	59.42	0.085
rGO-160_1	8.20	76.86	0.029
rGO-160_2	94.81	3.89	0.118
rGO-160_4	89.13	3.89	0.101
rGO-160_8	75.20	3.90	0.090

UV-Vis analysis was conducted to reveal the optical properties of GO and rGO samples. The UV-Vis absorption spectra of GO and different rGO samples obtained at various reduction times are demonstrated in Figure 4.11A. Upon GO reduction from 1 hour to 8 hours, the maximum absorption peak of GO at 231 nm was gradually shifted to 266 nm, indicating the partial restoration of conjugated sp^2 network (Eda et al., 2010; Zheng et al., 2015). As lower energy was required to excite the electrons, the band gap of rGO was expected to be smaller. The optical band gaps of GO and rGO samples were then acquired from linear fits of the Tauc plots, as depicted in Figure 4.11B and Table 4.8. It was observed that the band gap of GO decreased from around 3.00 eV to 2.80 eV when GO was reduced for up to 8 hours. Since band gap of GO is proportional to the number of oxygen atoms present on surface, the band gap reduction was therefore attributed to removal of surficial OFGs. Besides that, it was also perceived that the decrease in band gap became insignificant after 2 hours of reduction, suggesting that OFGs were harder to be removed when the reaction temperature was maintained at 160 °C.

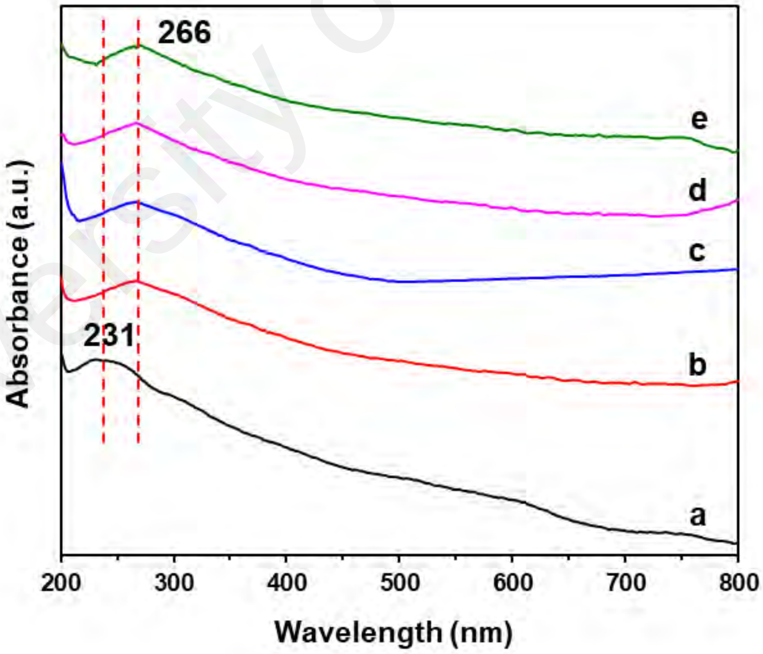

(A)

Figure 4.11, continued

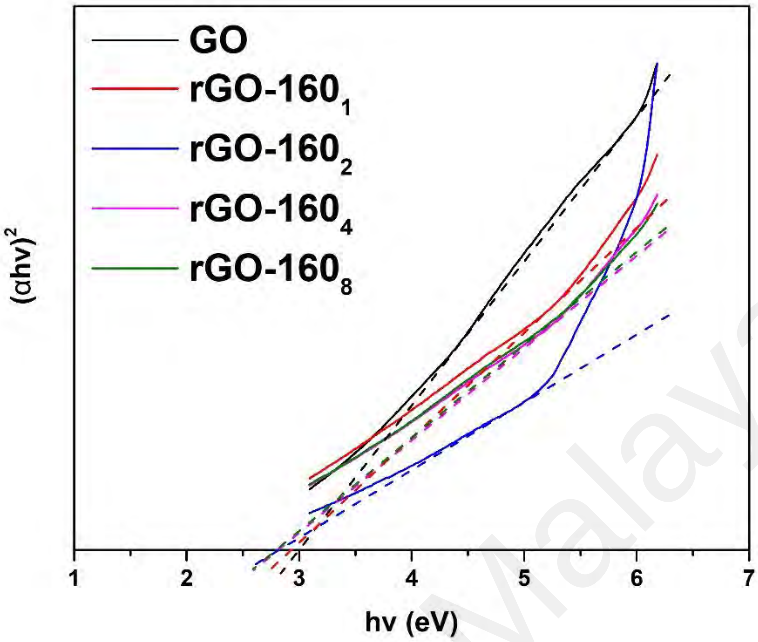

(B)

Figure 4.11. (A) UV-Vis absorption spectra of (a) GO, (b) rGO-160$_1$, (c) rGO-160$_2$, (d) rGO-160$_4$, and (e) rGO-160$_8$, **(B)** Tauc plots of GO, rGO-160$_1$, rGO-160$_2$, rGO-160$_4$, and rGO-160$_8$.

Table 4.8. Optical band gaps of GO, rGO-160$_1$, rGO-160$_2$, rGO-160$_4$, and rGO-160$_8$.

Sample	Band gap (eV)
GO	3.00
rGO-160$_1$	2.93
rGO-160$_2$	2.82
rGO-160$_4$	2.81
rGO-160$_8$	2.80

4.2.2 Adsorption and Photoactivity Measurements

The optimum reaction duration for GO reduction was determined by evaluating the MB adsorption and photodegradation of rGO photocatalysts. Throughout the experiments, the experimental conditions were fixed at 20 mg (catalyst loading), 50 ppm (initial dye concentration), double 95 W UV lamp (light intensity), and pH = 6 (initial pH of dye solution). Figure 4.12A illustrates the plot of $C_t/C_{initial}$ versus time for GO and different rGO samples obtained at various reduction times, and the corresponding results are depicted in Table 4.9. During the adsorption period, decreasing trends were noticed for all samples, implying that adsorption of dye molecules had taken place. The adsorption-desorption equilibrium between dye molecules and samples was reached after 4 hours of stirring in the dark (Appendix B). It was observed that the percentages of MB adsorption of both GO and rGO-160_1 were relatively close to each other, indicating that reduction of GO to rGO was not achieved within 1 hour. Among all samples, rGO-160_1 displayed the lowest dye adsorption efficiency, possibly due to its smallest SSA, while the highest dye adsorption efficiency was attained by rGO-160_2 with the largest SSA. The slight reduction in dye adsorption efficiencies of rGO-160_4 and rGO-160_8 could be related to the removal of more surficial OFGs after a longer reduction time (M.-j. Li et al., 2014). During the photocatalysis period, declining trends were also observed for all samples, which suggested that MB photodegradation reaction had occurred. Due to insufficient reduction time, rGO-160_1 also behaved like GO, whereby both of them displayed lower photodegradation efficiencies as compared to other rGO samples. The highest MB photodegradation efficiency was acquired by rGO-160_2, followed by rGO-160_4 and rGO-160_8. As the reduction time was prolonged from 2 hours to 8 hours, the SSA became smaller, thereby decreasing the interfacial contact areas between samples and dye molecules.

The linear plot of $\ln(C_0/C_t)$ versus irradiation time is illustrated in Figure 4.12B. It was suggested that the dye degradation processes followed pseudo-first-order reaction, as high correlation coefficients of $R^2 \geq 0.95$ were obtained. According to Table 4.9, rGO-160_2 displayed the highest rate constant, which is in good agreement with the highest photodegradation efficiency reported. Since rGO-160$_2$ was the best-performing photocatalyst as compared to other rGO samples, it was then selected to study the effects of catalyst loading, initial dye concentration, light intensity, and pH of solution on MB adsorption and photodegradation processes.

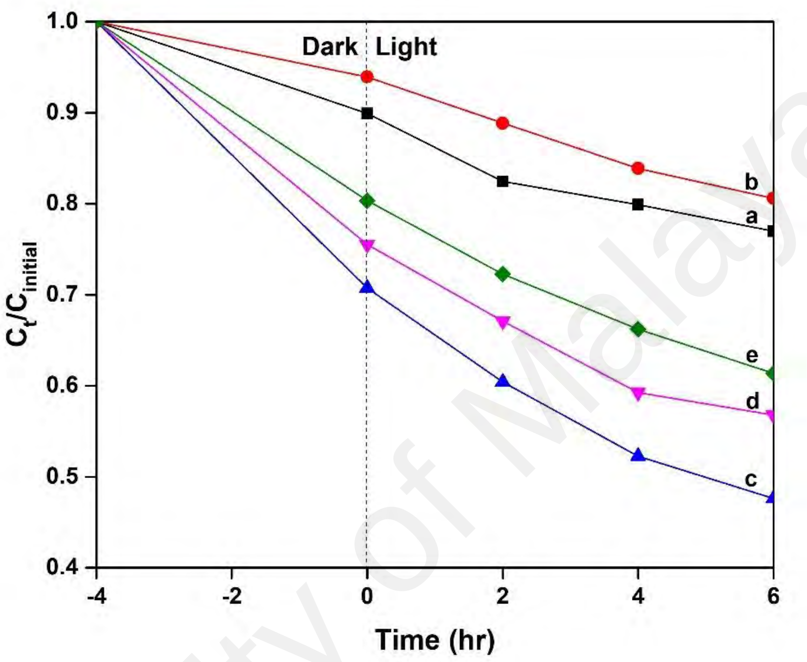

(A)

Figure 4.12, continued

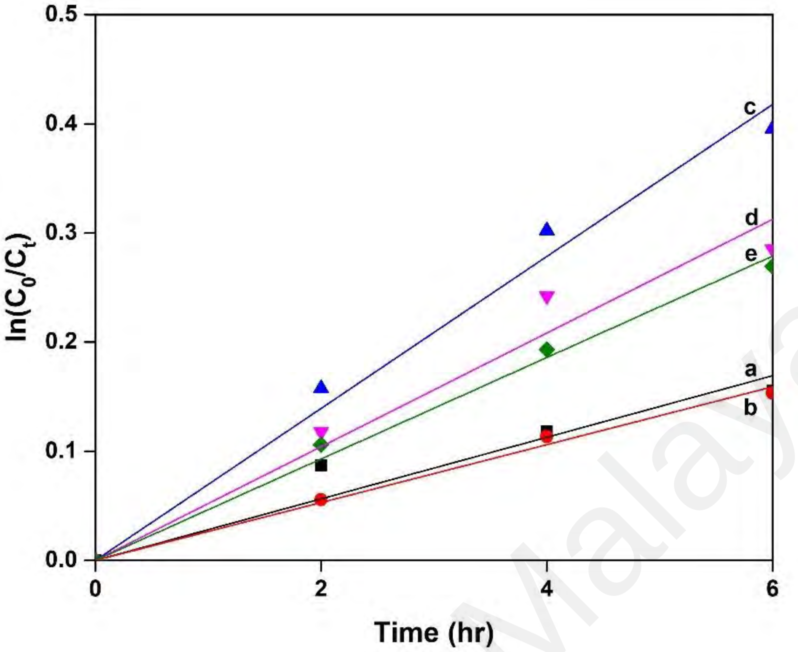

(B)

Figure 4.12. (A) MB adsorption and photodegradation of (a) GO, (b) rGO-160_1, (c) rGO-160_2, (d) rGO-160_4, and (e) rGO-160_8, **(B)** a linear plot of MB photodegradation in the presence of (a) GO, (b) rGO-160_1, (c) rGO-160_2, (d) rGO-160_4, and (e) rGO-160_8.

Table 4.9. Effect of reaction duration on adsorption percentage, photodegradation efficiency, and photodegradation rate of MB dye.

Sample	Adsorption Percentage (%)	Photodegradation Efficiency (%)	k (h^{-1})	R^2
GO	10.07	14.41	0.028	0.9517
rGO-160_1	6.06	14.22	0.027	0.9932
rGO-160_2	29.26	32.68	0.070	0.9844
rGO-160_4	24.49	24.81	0.052	0.9579
rGO-160_8	19.65	23.64	0.047	0.9924

4.3 Effect of Catalyst Loading

In order to avoid wastage of catalyst and also to ensure maximum absorption of photons emitted from UV light source, a series of experiments was performed by varying the amount of rGO-160_2 from 10 mg to 70 mg. It should be noted that initial dye concentration (50 ppm), light intensity (double 95 W UV lamp), and pH of solution (pH = 6) were kept constant throughout the experiments. Figure 4.13A depicts the effect of different catalyst loadings on MB adsorption and photodegradation reactions, and the corresponding results are tabulated in Table 4.10. The appropriate adsorption-desorption equilibrium between dye molecules and samples was established after stirring for 4 hours under dark condition (Appendix C). In the adsorption process, the percentage of MB adsorption was proportional to amount of rGO-160_2 used. When the dosage of photocatalyst was increased, the total SSA of photocatalyst became larger. Subsequently, the available active sites for adsorption of dye molecules also increased, which in turn increased the efficiency of dye adsorption (Auta & Hameed, 2013; Karaer & Uzun, 2013; Naeem et al., 2018). In the photocatalysis process, the MB photodegradation efficiency was also proportional to amount of rGO-160_2 used. With an increase in photocatalyst dosage, the total number of photocatalyst particles also increased, which then enhanced the absorption of photons for generation of electrons and holes, and improved the rate of formation of ROS for degradation of dye molecules (Benhebal et al., 2013; Rajamanickam & Shanthi, 2016; Rauf et al., 2011). When 70 mg of rGO-160_2 was used, the remaining MB concentration became very low after dark adsorption, possibly giving rise to inconsistency in photodegradation results. Therefore, 60 mg was considered as the optimum catalyst loading for this study.

Figure 4.13B shows the linear plot of $\ln(C_0/C_t)$ versus irradiation time. It was found that the photodegradation mechanisms fitted well with pseudo-first-order kinetic model as compared to pseudo-second-order kinetic model, as higher correlation coefficients of

$R^2 \geq 0.95$ were acquired. Based on Table 4.10, the rate constant increased with increasing amount of rGO-160$_2$ used, which indicated a proportional relationship between them.

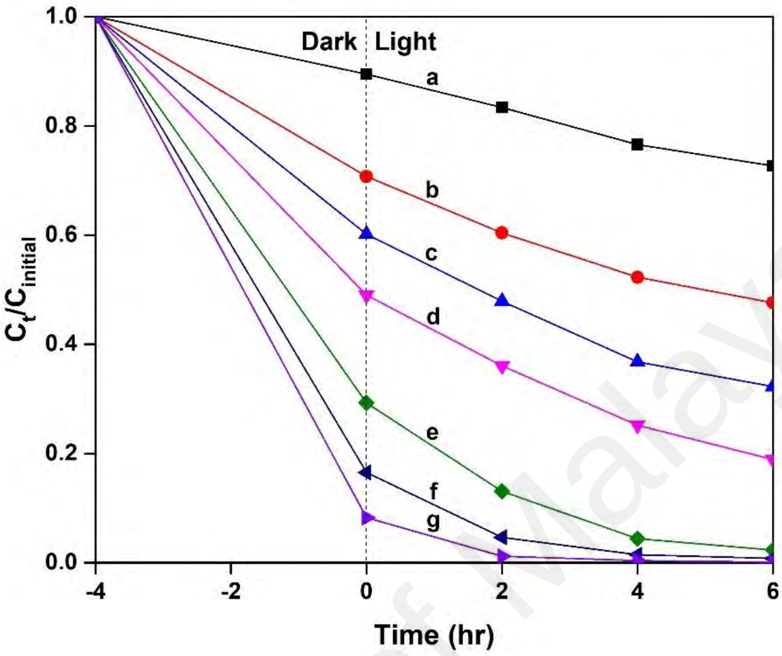

(A)

Figure 4.13, continued

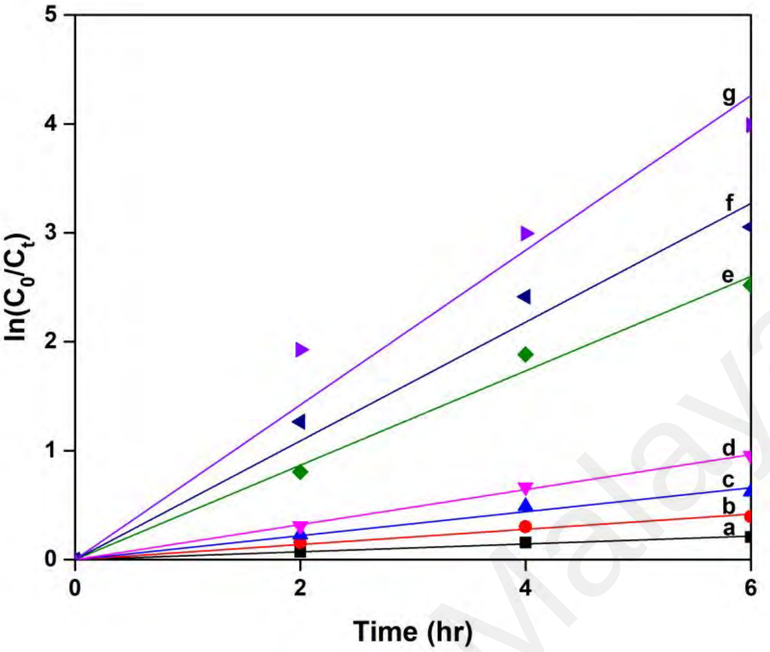

(B)

Figure 4.13. (A) Effect of (a) 10 mg, (b) 20 mg, (c) 30 mg, (d) 40 mg, (e) 50 mg, (f) 60 mg, and (g) 70 mg of rGO-160$_2$ on MB adsorption and photodegradation, **(B)** pseudo-first-order kinetic plot of MB photodegradation in the presence of (a) 10 mg, (b) 20 mg, (c) 30 mg, (d) 40 mg, (e) 50 mg, (f) 60 mg, and (g) 70 mg of rGO-160$_2$.

Table 4.10. Effect of catalyst loading on adsorption percentage, photodegradation efficiency, and photodegradation rate of MB dye.

Weight (mg)	Adsorption Percentage (%)	Photodegradation Efficiency (%)	k (h^{-1})	R^2
10	10.50	18.82	0.036	0.9919
20	29.26	32.68	0.070	0.9844
30	39.81	46.35	0.110	0.9822
40	50.96	61.46	0.161	0.9983
50	70.72	91.95	0.433	0.9914
60	83.45	95.29	0.545	0.9756
70	91.74	98.15	0.710	0.9594

4.4 Effect of Initial Dye Concentration

It is known that initial dye concentration has a significant effect on dye adsorption and photodegradation rate. Therefore, a series of experiments was carried out to evaluate the effect of initial dye concentration, ranging from 50 ppm to 125 ppm, on MB adsorption and photodegradation reactions, as illustrated in Figure 4.14A. The corresponding results are then summarized in Table 4.11. Throughout the experiments, catalyst loading (60 mg), light intensity (double 95 W UV lamp), and pH of solution (pH = 6) were kept constant. The adsorption-desorption equilibrium between dye molecules and samples was reached after 4 hours of stirring in the dark (Appendix D). In the adsorption process, the percentage of MB adsorption was inversely proportional to initial dye concentration used. As the initial dye concentration was increased, more dye molecules accumulated on surface of photocatalyst. Eventually, the available adsorption sites became saturated and insufficient to accommodate the increasing amount of dye molecules present in solution, thereby reducing dye removal efficiency (Dawood et al., 2016; Sahraei et al., 2016). In the photocatalysis process, the MB photodegradation efficiency was also inversely proportional to initial dye concentration used. Since the active sites were saturated with dye molecules, the production of ROS responsible for photocatalytic dye degradation reaction became limited (Gao et al., 2019; R. Sharma et al., 2015). The findings could also be explained by Beer-Lambert law, stating that as the initial dye concentration was increased, the path length of photons entering solution decreased, thereby resulting in lower rate of reaction (C.-S. Lu et al., 2013).

The plot of $\ln(C_0/C_t)$ as a function of irradiation time is depicted in Figure 4.14B. The photodegradation reactions followed pseudo-first-order rate law, as high correlation coefficients of $R^2 \geq 0.95$ were obtained. According to Table 4.11, an increase in initial dye concentration led to a decrease in rate constant, thereby revealing their inversely proportional relationship.

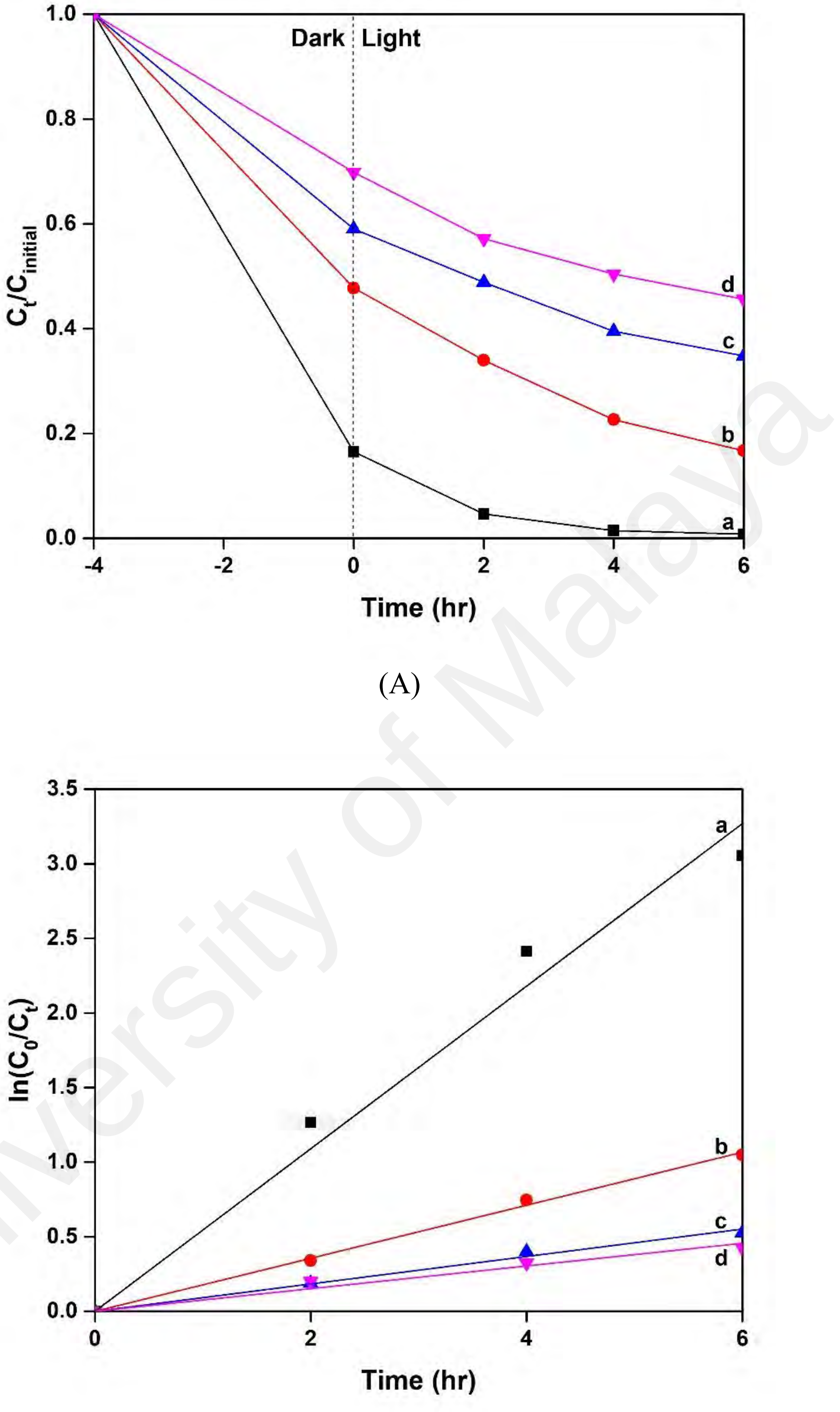

(A)

(B)

Figure 4.14. (A) Effect of (a) 50 ppm, (b) 75 ppm, (c) 100 ppm, and (d) 125 ppm on MB adsorption and photodegradation, **(B)** pseudo-first-order kinetic plot of MB photodegradation at (a) 50 ppm, (b) 75 ppm, (c) 100 ppm, and (d) 125 ppm of MB concentration.

Table 4.11. Effect of initial dye concentration on adsorption percentage, photodegradation efficiency, and photodegradation rate of MB dye.

Concentration (ppm)	Adsorption Percentage (%)	Photodegradation Efficiency (%)	*k* (h^{-1})	R^2
50	83.45	95.29	0.545	0.9756
75	52.25	64.97	0.178	0.9972
100	40.98	40.99	0.092	0.9893
125	30.14	34.71	0.076	0.9638

4.5 Effect of Light Intensity

It is worth to mention that photodegradation rate is highly affected by light intensity. Hence, a series of experiments was conducted by employing a single (30 $W\cdot m^{-2}$) or double (60 $W\cdot m^{-2}$) 95 W UV lamp as UV light source to investigate the effect of light intensity on MB photodegradation process. It should be noted that catalyst loading (60 mg), initial dye concentration (50 ppm), and pH of solution (pH = 6) were kept constant throughout the experiments. Figure 4.15A reveals the plot of C_t/C_0 versus time for MB photodegradation reaction, and the corresponding results are showed in Table 4.12. The efficiency of dye degradation was proportional to light intensity. This could be explained by the fact that when the light intensity was increased, there were more photons generated and absorbed by photocatalyst. As a result, more electrons were readily excited, leading to the formation of more electrons and holes, and the generation of more ROS to degrade dye molecules (Anku et al., 2016; Samsudin et al., 2015).

Figure 4.15B demonstrates the linear plot of $\ln(C_0/C_t)$ versus irradiation time. The dye degradation processes obeyed pseudo-first-order kinetics, as high correlation coefficients of $R^2 \geq 0.95$ were acquired. Based on Table 4.12, when the light intensity was increased, the apparent reaction rate constant also increased, implying a proportional relationship between them.

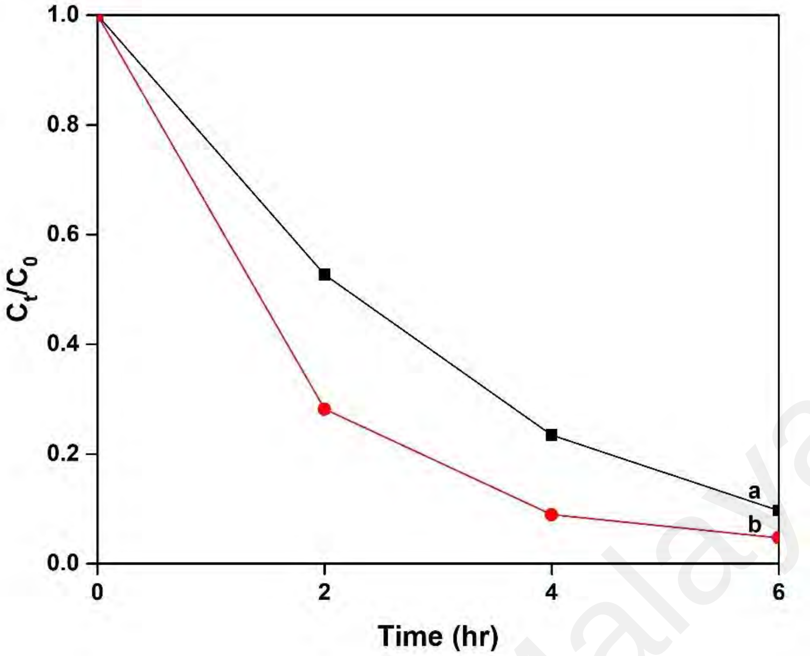

(A)

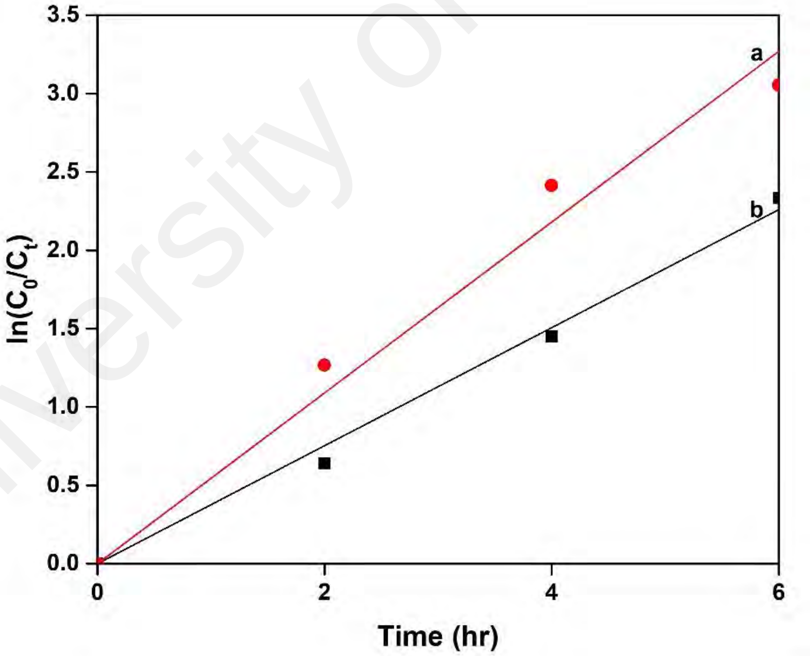

(B)

Figure 4.15. (A) Effect of a (a) single 95 W UV lamp, and a (b) double 95 W UV lamp on MB photodegradation, **(B)** pseudo-first-order kinetic plot of MB photodegradation in the presence of a (a) single 95 W UV lamp, and a (b) double 95 W UV lamp.

Table 4.12. Effect of light intensity on photodegradation efficiency and photodegradation rate of MB dye.

95 W UV Lamp	Photodegradation Efficiency (%)	*k* (h^{-1})	R^2
Single (30 $W{\cdot}m^{-2}$)	90.31	0.377	0.9931
Double (60 $W{\cdot}m^{-2}$)	95.29	0.545	0.9756

4.6 Effect of pH

The initial pH of dye solution is also one of the most important factors influencing dye adsorption and photodegradation rate. Therefore, a series of experiments was performed to examine the effect of different initial pH values (pH = 3, 6, 11) of dye solution on MB adsorption and photodegradation processes (Figure 4.16A). The corresponding results are then summarized in Table 4.13. Throughout the experiments, catalyst loading (60 mg), initial dye concentration (50 ppm), and light intensity (double 95 W UV lamp) were kept constant. The appropriate adsorption-desorption equilibrium between dye molecules and samples was established after stirring for 4 hours under dark condition (Appendix E). In overall, MB removal by adsorption and photodegradation reactions was proportional to initial pH of dye solution used. Under acidic condition, there were more hydrogen ions (H^+) present in dye solution. The dye molecules and H^+ then competed for the adsorption sites on photocatalyst. As a result, a lower efficiency of dye adsorption was observed, which then led to reduction in MB photodegradation efficiency (T. Huang et al., 2019; Koohi et al., 2019). For this reason, the photocatalyst displayed no remarkable contrast in overall dye removal efficiency at pH values of 3 and 6. When the dye solution was turned to basic at a higher pH of 11, a better overall removal of dye molecules was achieved. It was reported that MB adsorption in basic medium is greater than that in acidic medium due to cationic nature of dye molecules (Zarrabi et al., 2019). Moreover, the presence of excess hydroxide (OH^{-}) ions in dye solution also facilitated the formation of •OH, which in turn increased the photodegradation rate (Chiang & Lin, 2013).

The plot of $\ln(C_0/C_t)$ as a function of irradiation time is exhibited in Figure 4.16B. The dye degradation mechanisms were determined to be of pseudo-first-order reaction, as high correlation coefficients of $R^2 \geq 0.95$ were obtained. According to Table 4.13, an increase in initial pH of dye solution caused an increase in rate constant, thereby revealing their proportional relationship.

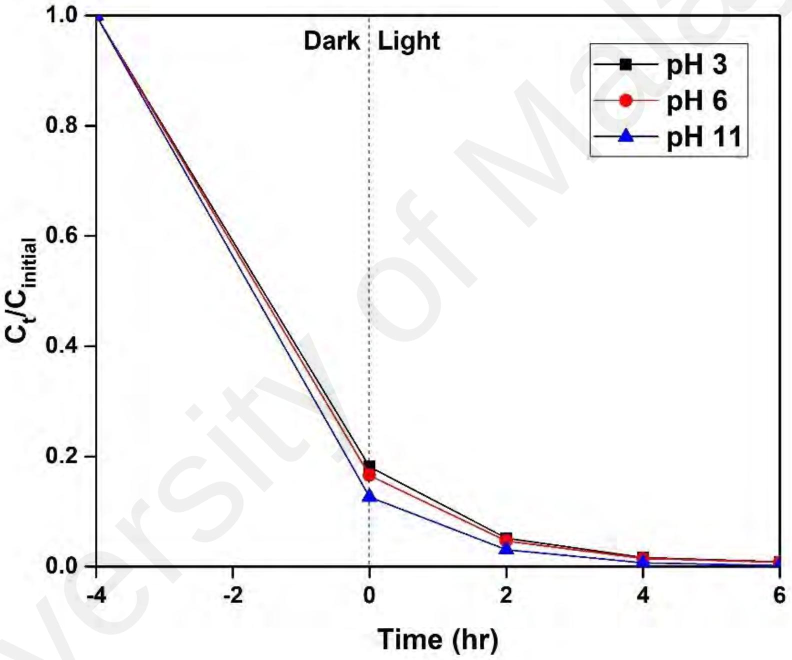

(A)

Figure 4.16, continued

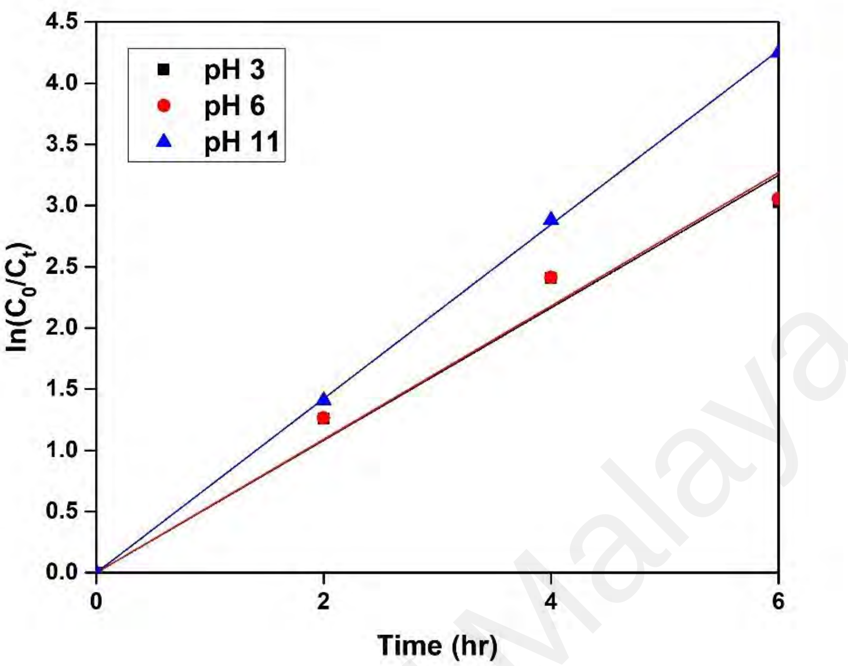

(B)

Figure 4.16. (A) Effect of initial pH of 3, 6, and 11 of dye solution on MB adsorption and photodegradation, **(B)** pseudo-first-order kinetic plot of MB photodegradation at an initial pH of 3, 6, and 11 of dye solution.

Table 4.13. Effect of pH on adsorption percentage, photodegradation efficiency, and photodegradation rate of MB dye.

pH	Adsorption Percentage (%)	Photodegradation Efficiency (%)	k (h^{-1})	R^2
3	81.85	95.14	0.541	0.9737
6	83.45	95.29	0.545	0.9756
11	87.39	98.57	0.711	0.9998

4.7 Recyclability Test

From perspective of practical applications, the recyclability of a photocatalyst is considered as a crucial factor. Figure 4.17 shows the stability test of rGO-160$_2$ for five consecutive cycles towards MB photodegradation process. It should be noted that catalyst loading (60 mg), initial dye concentration (50 ppm), light intensity (double 95 W UV lamp), and pH of solution (pH = 11) were kept constant throughout the experiments. After five cycles, the MB removal efficiency over rGO-160$_2$ was still greater than 90%, which indicated that rGO-160$_2$ exhibited high stability and good reusability.

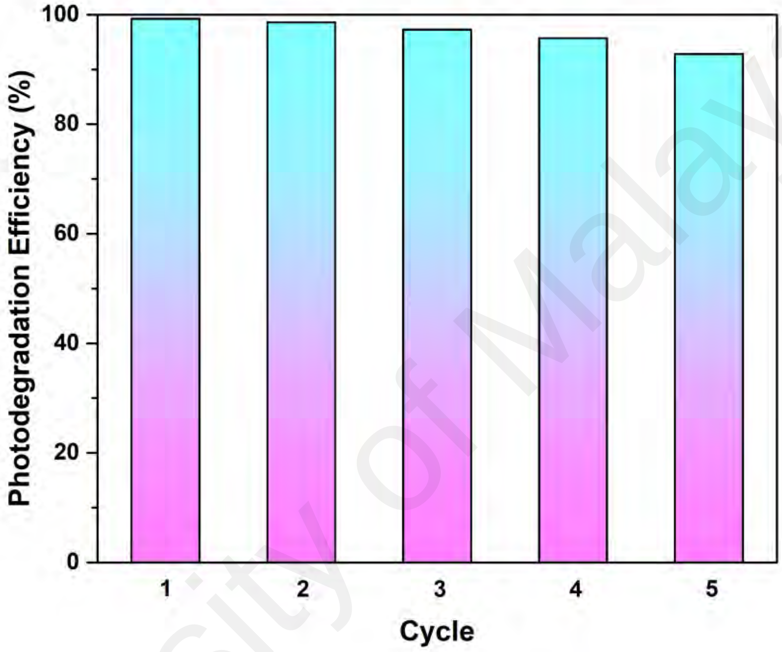

Figure 4.17. Recycling tests of rGO-160$_2$ for MB photodegradation.

CHAPTER 5: CONCLUSION

5.1 Conclusion

In conclusion, all three objectives were met. Initially, rGO was successfully synthesized through an environmentally benign solvothermal reduction approach without the employment of toxic reducing agents. Then, the effect of reaction temperature on reduction of GO was investigated. The results showed that 160 °C was the most appropriate reduction temperature to reduce GO, as lower reduction temperatures were unable to reduce GO to rGO. In addition, a higher reaction temperature was also deemed unsuitable for the synthesis of rGO as it would cause a reduction in SSA, thereby influencing the performance of rGO in MB adsorption and photodegradation reactions.

Apart from that, the effect of reaction duration on reduction of GO was also evaluated. Based on the results, it was found that 1 hour of reduction was not enough to reduce GO to rGO. Nevertheless, when the reduction time was increased to 2 hours, GO was subsequently reduced to rGO. Any further increase in the reduction time then resulted in a decrease in SSA, which was undesirable in dye adsorption and photodegradation processes. Under optimum reaction conditions of 160 °C and 2 hours for GO reduction, the rGO-160_2 formed was capable of attaining the highest MB removal by adsorption (29.26%) and photodegradation (32.68%) as compared to other samples.

Subsequently, the performance of rGO-160_2 was further improved under optimized conditions. The results demonstrated that overall removal of dye was proportional to catalyst loading, light intensity, and pH of solution, but inversely proportional to initial dye concentration. Hence, as 60 mg of rGO-160_2 was added into 50 ppm of MB solution at a basic pH of 11 under irradiation of UV light from a double 95 W lamp, a greater MB removal by adsorption (87.39%) and photodegradation (98.57%) was achieved. After repeating the dye degradation reaction for up to five times, there was still more than 90%

of MB photodegradation efficiency observed, indicating that $rGO\text{-}160_2$ was highly stable and reusable.

5.2 Recommendations for Future Research

In order to make this technology a reality in future, there are a few recommendations worth to consider as follows:

1. In this work, the operational parameters were investigated via one-factor-at-a-time approach. It is suggested that full factorial experiments are conducted in future to determine the most effective parameters influencing MB adsorption and photodegradation reactions, and the interactions between the parameters.
2. Throughout this work, the MB photodegradation reaction was performed under irradiation of UV light. Nevertheless, it is known that UV light merely covers about 5% of total solar radiation. Hence, future studies are encouraged to research more on using visible light, which makes up nearly 40% of sunlight, as the irradiation source instead.
3. Since rGO demonstrated excellent results in MB adsorption and photodegradation reactions, it is recommended to explore the performance of rGO towards a wider range of pollutants, such as pesticides and pharmaceutical drugs in order to maximize the potential of rGO as a metal-free catalyst for environmental remediation.
4. There have been a lot of researches focusing on the role of rGO as a support in formation of composite materials. However, the application of rGO as a co-catalyst in these materials has not been comprehensively investigated. Therefore, future research can be conducted to obtain a deeper understanding regarding this matter.

REFERENCES

Abid, Sehrawat, P., Islam, S., Mishra, P., & Ahmad, S. (2018). Reduced graphene oxide (rGO) based wideband optical sensor and the role of temperature, defect states and quantum efficiency. *Scientific Reports, 8*, 3537.

Ahn, H., Kang, S. G., Yoon, S.-i., Ko, H.-J., Kim, P.-H., Hong, E.-J., An, B.-S., Lee, E., & Lee, G.-S. (2017). Methylene blue inhibits NLRP3, NLRC4, AIM2, and non-canonical inflammasome activation. *Scientific Reports, 7*, 12409.

Akin, M. B., & Oner, M. (2013). Photodegradation of methylene blue with sphere-like ZnO particles prepared via aqueous solution. *Ceramics International, 39*(8), 9759-9762.

Ali, G., Mehmood, A., Ha, H. Y., Kim, J., & Chung, K. Y. (2017). Reduced graphene oxide as a stable and high-capacity cathode material for Na-ion batteries. *Scientific Reports, 7*, 40910.

Aliofkhazraei, M., Ali, N., Milne, W. I., Ozkan, C. S., Mitura, S., & Gervasoni, J. L. (2016). *Graphene Science Handbook: Applications and Industrialization*. Boca Raton: CRC Press.

ALOthman, Z. A. (2012). A review: Fundamental aspects of silicate mesoporous materials. *Materials, 5*(12), 2874-2902.

AlShammari, A., Halim, M. M., Yam, F. K., Al-Hardan, N. H., Kaus, N. H. M., Umar, K., Qahtan, T. F., & Ibrahim, M. N. M. (2019). The effect of substrate temperatures on the structural and conversion of thin films of reduced graphene oxide. *Physica B: Condensed Matter, 572*, 296-301.

Ameer, S., Gul, I. H., Mahmood, N., & Mujahid, M. (2015). Synthesis, characterization and optical properties of in situ $ZnFe_2O_4$ functionalized rGO nano hybrids through modified solvothermal approach. *Optical Materials, 45*, 69-75.

Ameta, S., & Ameta, R. (2018). *Advanced Oxidation Processes for Wastewater Treatment: Emerging Green Chemical Technology*. London: Academic Press.

Anku, W., Oppong, S. O.-B., Shukla, S. K., & Govender, P. P. (2016). Comparative photocatalytic degradation of monoazo and diazo dyes under simulated visible light using Fe^{3+}/C/S doped-TiO_2 nanoparticles. *Acta Chimica Slovenica, 63*(2), 380-391.

Apul, O. G., Wang, Q., Zhou, Y., & Karanfil, T. (2013). Adsorption of aromatic organic contaminants by graphene nanosheets: Comparison with carbon nanotubes and activated carbon. *Water Research, 47*(4), 1648-1654.

Auta, M., & Hameed, B. (2013). Acid modified local clay beads as effective low-cost adsorbent for dynamic adsorption of methylene blue. *Journal of Industrial and Engineering Chemistry, 19*(4), 1153-1161.

Báez, D. F., Pardo, H., Laborda, I., Marco, J. F., Yáñez, C., & Bollo, S. (2017). Reduced graphene oxides: Influence of the reduction method on the electrocatalytic effect towards nucleic acid oxidation. *Nanomaterials, 7*(7), 168.

Bandosz, T. J. (2006). *Activated Carbon Surfaces in Environmental Remediation* (Vol. 7). San Diego: Academic Press.

Basith, M., Ahsan, R., Zarin, I., & Jalil, M. (2018). Enhanced photocatalytic dye degradation and hydrogen production ability of $Bi_{25}FeO_{40}$-rGO nanocomposite and mechanism insight. *Scientific Reports, 8*, 11090.

Benhebal, H., Chaib, M., Salmon, T., Geens, J., Leonard, A., Lambert, S. D., Crine, M., & Heinrichs, B. (2013). Photocatalytic degradation of phenol and benzoic acid using zinc oxide powders prepared by the sol–gel process. *Alexandria Engineering Journal, 52*(3), 517-523.

Bhuyan, M. S. A., Uddin, M. N., Islam, M. M., Bipasha, F. A., & Hossain, S. S. (2016). Synthesis of graphene. *International Nano Letters, 6*(2), 65-83.

Bianco, A., Cheng, H.-M., Enoki, T., Gogotsi, Y., Hurt, R. H., Koratkar, N., Kyotani, T., Monthioux, M., Park, C. R., & Tascon, J. M. (2013). All in the graphene family–A recommended nomenclature for two-dimensional carbon materials. *Carbon, 65*, 1-6.

Bora, L. V., & Mewada, R. K. (2017). Visible/solar light active photocatalysts for organic effluent treatment: Fundamentals, mechanisms and parametric review. *Renewable and Sustainable Energy Reviews, 76*, 1393-1421.

Bustos-Ramírez, K., Barrera-Díaz, C. E., De Icaza-Herrera, M., Martínez-Hernández, A. L., Natividad-Rangel, R., & Velasco-Santos, C. (2015). 4-chlorophenol removal from water using graphite and graphene oxides as photocatalysts. *Journal of Environmental Health Science and Engineering, 13*, 33.

Bustos-Ramirez, K., Barrera-Diaz, C. E., De Icaza, M., Martínez-Hernández, A. L., & Velasco-Santos, C. (2015). Photocatalytic activity in phenol removal of water from graphite and graphene oxides: Effect of degassing and chemical oxidation in the synthesis process. *Journal of Chemistry, 2015*, 254631.

Chan, S. H. S., Yeong Wu, T., Juan, J. C., & Teh, C. Y. (2011). Recent developments of metal oxide semiconductors as photocatalysts in advanced oxidation processes (AOPs) for treatment of dye waste-water. *Journal of Chemical Technology & Biotechnology, 86*(9), 1130-1158.

Chandra, S., Das, P., Bag, S., Bhar, R., & Pramanik, P. (2012). Mn_2O_3 decorated graphene nanosheet: An advanced material for the photocatalytic degradation of organic dyes. *Materials Science and Engineering: B, 177*(11), 855-861.

Chen, X., & Chen, B. (2015). Macroscopic and spectroscopic investigations of the adsorption of nitroaromatic compounds on graphene oxide, reduced graphene oxide, and graphene nanosheets. *Environmental Science & Technology, 49*(10), 6181-6189.

Cheng, J., Zhong, R., Lin, J., Zhu, J., Wan, W., & Chen, X. (2017). Linear graphene nanocomposite synthesis and an analytical application for the amino acid detection of *Camellia nitidissima* chi seeds. *Materials, 10*(4), 443.

Chiang, Y.-J., & Lin, C.-C. (2013). Photocatalytic decolorization of methylene blue in aqueous solutions using coupled ZnO/SnO_2 photocatalysts. *Powder Technology, 246*, 137-143.

Chowdhury, I., Mansukhani, N. D., Guiney, L. M., Hersam, M. C., & Bouchard, D. (2015). Aggregation and stability of reduced graphene oxide: Complex roles of divalent cations, pH, and natural organic matter. *Environmental Science & Technology, 49*(18), 10886-10893.

Chowdhury, S., & Saha, P. D. (2012). Biosorption of methylene blue from aqueous solutions by a waste biomaterial: Hen feathers. *Applied Water Science, 2*(3), 209-219.

Cui, P., Lee, J., Hwang, E., & Lee, H. (2011). One-pot reduction of graphene oxide at subzero temperatures. *Chemical Communications, 47*(45), 12370-12372.

Cui, S., Pu, H., Mattson, E. C., Wen, Z., Chang, J., Hou, Y., Hirschmugl, C. J., & Chen, J. (2014). Ultrasensitive chemical sensing through facile tuning defects and functional groups in reduced graphene oxide. *Analytical Chemistry, 86*(15), 7516-7522.

Dante, R. C. (2015). *Handbook of Friction Materials and Their Applications*. Cambridge: Woodhead Publishing.

Dave, K., Park, K. H., & Dhayal, M. (2015). Two-step process for programmable removal of oxygen functionalities of graphene oxide: Functional, structural and electrical characteristics. *RSC Advances, 5*(116), 95657-95665.

Dawood, S., Sen, T. K., & Phan, C. (2016). Adsorption removal of Methylene Blue (MB) dye from aqueous solution by bio-char prepared from *Eucalyptus sheathiana* bark: Kinetic, equilibrium, mechanism, thermodynamic and process design. *Desalination and Water Treatment, 57*(59), 28964-28980.

De, D., Chakraborty, M., Majumdar, S., & Giri, S. (2014). Bandgap engineering through nanocrystalline magnetic alloy grafting on reduced graphene oxide. *Physical Chemistry Chemical Physics, 16*(36), 19661-19667.

De Laurentis, M., & Irace, A. (2014). Optical measurement techniques of recombination lifetime based on the free carriers absorption effect. *Journal of Solid State Physics, 2014*, 291469.

Delhaès, P. (2000). *Graphite and Precursors*. Amsterdam: Gordon and Breach Science Publishers.

Dreyer, D. R., Murali, S., Zhu, Y., Ruoff, R. S., & Bielawski, C. W. (2011). Reduction of graphite oxide using alcohols. *Journal of Materials Chemistry, 21*(10), 3443-3447.

Dreyer, D. R., Park, S., Bielawski, C. W., & Ruoff, R. S. (2010). The chemistry of graphene oxide. *Chemical Society Reviews, 39*(1), 228-240.

Dutta, S., Bhattacharyya, A., Ganguly, A., Gupta, S., & Basu, S. (2011). Application of response surface methodology for preparation of low-cost adsorbent from citrus fruit peel and for removal of methylene blue. *Desalination, 275*(1-3), 26-36.

Eda, G., Lin, Y. Y., Mattevi, C., Yamaguchi, H., Chen, H.-A., Chen, I.-S., Chen, C.-W., & Chhowalla, M. (2010). Blue photoluminescence from chemically derived graphene oxide. *Advanced Materials, 22*(4), 505-509.

Edison, T. N. J. I., Atchudan, R., Kamal, C., & Lee, Y. R. (2016). *Caulerpa racemosa*: A marine green alga for eco-friendly synthesis of silver nanoparticles and its catalytic degradation of methylene blue. *Bioprocess and Biosystems Engineering, 39*(9), 1401-1408.

Elango, G., & Roopan, S. M. (2016). Efficacy of SnO_2 nanoparticles toward photocatalytic degradation of methylene blue dye. *Journal of Photochemistry and Photobiology B: Biology, 155*, 34-38.

Emiru, T. F., & Ayele, D. W. (2017). Controlled synthesis, characterization and reduction of graphene oxide: A convenient method for large scale production. *Egyptian Journal of Basic and Applied Sciences, 4*(1), 74-79.

Ersan, G., Apul, O. G., Perreault, F., & Karanfil, T. (2017). Adsorption of organic contaminants by graphene nanosheets: A review. *Water Research, 126*, 385-398.

Ersan, G., Kaya, Y., Apul, O. G., & Karanfil, T. (2016). Adsorption of organic contaminants by graphene nanosheets, carbon nanotubes and granular activated carbons under natural organic matter preloading conditions. *Science of the Total Environment, 565*, 811-817.

Eskizeybek, V., Sarı, F., Gülce, H., Gülce, A., & Avcı, A. (2012). Preparation of the new polyaniline/ZnO nanocomposite and its photocatalytic activity for degradation of methylene blue and malachite green dyes under UV and natural sun lights irradiations. *Applied Catalysis B: Environmental, 119-120*, 197-206.

Fan, Z., Wang, K., Wei, T., Yan, J., Song, L., & Shao, B. (2010). An environmentally friendly and efficient route for the reduction of graphene oxide by aluminum powder. *Carbon, 48*(5), 1686-1689.

Fathy, M., Gomaa, A., Taher, F. A., El-Fass, M. M., & Kashyout, A. E.-H. B. (2016). Optimizing the preparation parameters of GO and rGO for large-scale production. *Journal of Materials Science, 51*(12), 5664-5675.

Fil, B. A., Ozmetin, C., & Korkmaz, M. (2012). Cationic dye (methylene blue) removal from aqueous solution by montmorillonite. *Bulletin of the Korean Chemical Society, 33*(10), 3184-3190.

Fradj, A. B., Hamouda, S. B., Ouni, H., Lafi, R., Gzara, L., & Hafiane, A. (2014). Removal of methylene blue from aqueous solutions by poly(acrylic acid) and poly(ammonium acrylate) assisted ultrafiltration. *Separation and Purification Technology, 133*, 76-81.

Gao, Y., Gu, S., Duan, L., Wang, Y.-r., & Gao, G. (2019). Robust and anti-fatigue hydrophobic association hydrogels assisted by titanium dioxide for photocatalytic activity. *Soft Matter, 15*(19), 3897-3905.

Georgakilas, V., Perman, J. A., Tucek, J., & Zboril, R. (2015). Broad family of carbon nanoallotropes: Classification, chemistry, and applications of fullerenes, carbon dots, nanotubes, graphene, nanodiamonds, and combined superstructures. *Chemical Reviews, 115*(11), 4744-4822.

Goldstein, J. I., Newbury, D. E., Michael, J. R., Ritchie, N. W., Scott, J. H. J., & Joy, D. C. (2017). *Scanning Electron Microscopy and X-Ray Microanalysis* (4th ed.). New York: Springer.

Guardia, L., Villar-Rodil, S., Paredes, J., Rozada, R., Martínez-Alonso, A., & Tascón, J. (2012). UV light exposure of aqueous graphene oxide suspensions to promote their direct reduction, formation of graphene–metal nanoparticle hybrids and dye degradation. *Carbon, 50*(3), 1014-1024.

Gupta, K., & Khatri, O. P. (2017). Reduced graphene oxide as an effective adsorbent for removal of malachite green dye: Plausible adsorption pathways. *Journal of Colloid and Interface Science, 501*, 11-21.

Hack, R., Correia, C. H. G., Zanon, R. A. d. S., & Pezzin, S. H. (2018). Characterization of graphene nanosheets obtained by a modified Hummer's method. *Matéria (Rio de Janeiro), 23*(1), e-11988.

Hansora, D., & Mishra, S. (2018). *Graphene Nanomaterials: Fabrication, Properties, and Applications*. Singapore: Pan Stanford Publishing.

He, J., & Fang, L. (2016). Controllable synthesis of reduced graphene oxide. *Current Applied Physics, 16*(9), 1152-1158.

He, S., Hou, P., Petropoulos, E., Feng, Y., Yu, Y., Xue, L., & Yang, L. (2018). High efficient visible-light photocatalytic performance of Cu/ZnO/rGO nanocomposite for decomposing of aqueous ammonia and treatment of domestic wastewater. *Frontiers in Chemistry, 6*, 219.

He, W., Cai, J., Jiang, X., Yin, J., & Meng, Q. (2018). Generation of reactive oxygen species and charge carriers in plasmonic photocatalytic Au@TiO_2 nanostructures with enhanced activity. *Physical Chemistry Chemical Physics, 20*(23), 16117-16125.

Hou, D., Liu, Q., Wang, X., Quan, Y., Qiao, Z., Yu, L., & Ding, S. (2018). Facile synthesis of graphene via reduction of graphene oxide by artemisinin in ethanol. *Journal of Materiomics, 4*(3), 256-265.

Hsu, H.-C., Shown, I., Wei, H.-Y., Chang, Y.-C., Du, H.-Y., Lin, Y.-G., Tseng, C.-A., Wang, C.-H., Chen, L.-C., & Lin, Y.-C. (2013). Graphene oxide as a promising photocatalyst for CO_2 to methanol conversion. *Nanoscale, 5*(1), 262-268.

Hu, C., Lu, T., Chen, F., & Zhang, R. (2013). A brief review of graphene–metal oxide composites synthesis and applications in photocatalysis. *Journal of the Chinese Advanced Materials Society, 1*(1), 21-39.

Huang, H.-H., De Silva, K. K. H., Kumara, G., & Yoshimura, M. (2018). Structural evolution of hydrothermally derived reduced graphene oxide. *Scientific Reports, 8*, 6849.

Huang, T., Yan, M., He, K., Huang, Z., Zeng, G., Chen, A., Peng, M., Li, H., Yuan, L., & Chen, G. (2019). Efficient removal of methylene blue from aqueous solutions using magnetic graphene oxide modified zeolite. *Journal of Colloid and Interface Science, 543*, 43-51.

Jin, Y., Huang, S., Zhang, M., Jia, M., & Hu, D. (2013). A green and efficient method to produce graphene for electrochemical capacitors from graphene oxide using sodium carbonate as a reducing agent. *Applied Surface Science, 268*, 541-546.

Kang, X., Liu, S., Dai, Z., He, Y., Song, X., & Tan, Z. (2019). Titanium dioxide: From engineering to applications. *Catalysts, 9*(2), 191.

Kant, S., Pathania, D., Singh, P., Dhiman, P., & Kumar, A. (2014). Removal of malachite green and methylene blue by $Fe_{0.01}Ni_{0.01}Zn_{0.98}O$/polyacrylamide nanocomposite using coupled adsorption and photocatalysis. *Applied Catalysis B: Environmental, 147*, 340-352.

Karaer, H., & Uzun, İ. (2013). Adsorption of basic dyestuffs from aqueous solution by modified chitosan. *Desalination and Water Treatment, 51*(10-12), 2294-2305.

Kaur, J., Anand, K., Thangaraj, R., & Singh, R. (2016). Synthesis, characterization and photocatalytic activity of visible-light-driven reduced graphene oxide–CeO_2 nanocomposite. *Indian Journal of Physics, 90*(10), 1183-1194.

Khan, M. M., Pradhan, D., & Sohn, Y. (2017). *Nanocomposites for Visible Light-induced Photocatalysis*. Cham: Springer.

Khan, Q. A., Shaur, A., Khan, T. A., Joya, Y. F., & Awan, M. (2017). Characterization of reduced graphene oxide produced through a modified Hoffman method. *Cogent Chemistry, 3*(1), 1298980.

Kharisov, B. I., & Kharissova, O. V. (2019). *Carbon Allotropes: Metal-Complex Chemistry, Properties and Applications*. Cham: Springer.

Kim, D., Yang, S. J., Kim, Y. S., Jung, H., & Park, C. R. (2012). Simple and cost-effective reduction of graphite oxide by sulfuric acid. *Carbon, 50*(9), 3229-3232.

Kim, H., Kang, S.-O., Park, S., & Park, H. S. (2015). Adsorption isotherms and kinetics of cationic and anionic dyes on three-dimensional reduced graphene oxide macrostructure. *Journal of Industrial and Engineering Chemistry, 21*, 1191-1196.

Kim, Y.-B., & Ahn, J.-H. (2014). Microwave-assisted decolorization and decomposition of methylene blue with persulfate. *International Biodeterioration & Biodegradation, 95*, 208-211.

Kitai, A. (2018). *Principles of Solar Cells, LEDs and Related Devices: The Role of the PN Junction* (2nd ed.). Hoboken: Wiley.

Konicki, W., Sibera, D., & Narkiewicz, U. (2018). Adsorptive removal of cationic dye from aqueous solutions by $ZnO/ZnMn_2O_4$ nanocomposite. *Separation Science and Technology, 53*(9), 1295-1306.

Koohi, S. R., Allahyari, S., Kahforooshan, D., Rahemi, N., & Tasbihi, M. (2019). Natural minerals as support of silicotungstic acid for photocatalytic degradation of methylene blue in wastewater. *Journal of Inorganic and Organometallic Polymers and Materials, 29*(2), 365-377.

Krishnamoorthy, K., Mohan, R., & Kim, S.-J. (2011). Graphene oxide as a photocatalytic material. *Applied Physics Letters, 98*(24), 244101.

Kumar, A. J., & Namasivayam, C. (2014). Uptake of endocrine disruptor bisphenol-A onto sulphuric acid activated carbon developed from biomass: Equilibrium and kinetic studies. *Sustainable Environment Research, 24*(1), 73-80.

Kumar, N., & Kumbhat, S. (2016). *Essentials in Nanoscience and Nanotechnology*. New York: John Wiley & Sons.

Kumar, P., Sain, B., & Jain, S. L. (2014). Photocatalytic reduction of carbon dioxide to methanol using a ruthenium trinuclear polyazine complex immobilized on graphene oxide under visible light irradiation. *Journal of Materials Chemistry A, 2*(29), 11246-11253.

Kumarasinghe, A., Samaranayake, L., Bondino, F., Magnano, E., Kottegoda, N., Carlino, E., Ratnayake, U. N., De Alwis, A. A. P., Karunaratne, V., & Amaratunga, G. A. (2013). Self-assembled multilayer graphene oxide membrane and carbon nanotubes synthesized using a rare form of natural graphite. *The Journal of Physical Chemistry C, 117*(18), 9507-9519.

Kumbhakar, P., Pramanik, A., Biswas, S., Kole, A. K., Sarkar, R., & Kumbhakar, P. (2018). In-situ synthesis of rGO-ZnO nanocomposite for demonstration of sunlight driven enhanced photocatalytic and self-cleaning of organic dyes and tea stains of cotton fabrics. *Journal of Hazardous Materials, 360*, 193-203.

Kyzas, G. Z., & Kostoglou, M. (2014). Green adsorbents for wastewaters: A critical review. *Materials, 7*(1), 333-364.

Lee, K. M., Lai, C. W., Ngai, K. S., & Juan, J. C. (2016). Recent developments of zinc oxide based photocatalyst in water treatment technology: A review. *Water Research, 88*, 428-448.

Li, B., Pan, G., Avent, N. D., Islam, K., Awan, S., & Davey, P. (2016). A simple approach to preparation of graphene/reduced graphene oxide/polyallylamine electrode and their electrocatalysis for hydrogen peroxide reduction. *Journal of Nanoscience and Nanotechnology, 16*(12), 12805-12810.

Li, F., Jiang, X., Zhao, J., & Zhang, S. (2015). Graphene oxide: A promising nanomaterial for energy and environmental applications. *Nano Energy, 16*, 488-515.

Li, M.-j., Liu, C.-m., Xie, Y.-b., Cao, H.-b., Zhao, H., & Zhang, Y. (2014). The evolution of surface charge on graphene oxide during the reduction and its application in electroanalysis. *Carbon, 66*, 302-311.

Li, S., Lin, Q., Liu, X., Yang, L., Ding, J., Dong, F., Li, Y., Irfan, M., & Zhang, P. (2018). Fast photocatalytic degradation of dyes using low-power laser-fabricated Cu_2O–Cu nanocomposites. *RSC Advances, 8*(36), 20277-20286.

Li, Y., Du, Q., Liu, T., Peng, X., Wang, J., Sun, J., Wang, Y., Wu, S., Wang, Z., & Xia, Y. (2013). Comparative study of methylene blue dye adsorption onto activated carbon, graphene oxide, and carbon nanotubes. *Chemical Engineering Research and Design, 91*(2), 361-368.

Li, Z., Xu, S. C., Zhang, C., Liu, X. Y., Gao, S. S., Hu, L. T., Guo, J., Ma, Y., Jiang, S. Z., & Si, H. P. (2016). High-performance SERS substrate based on hybrid structure of graphene oxide/AgNPs/Cu film@pyramid Si. *Scientific Reports, 6*, 38539.

Lian, K.-Y., Ji, Y.-F., Li, X.-F., Jin, M.-X., Ding, D.-J., & Luo, Y. (2013). Big bandgap in highly reduced graphene oxides. *The Journal of Physical Chemistry C, 117*(12), 6049-6054.

Lin, Z., Ye, M., & Wang, M. (2018). *Multifunctional Photocatalytic Materials for Energy*. Duxford: Woodhead Publishing.

Liu, C., Wang, X., Ma, P., Chen, J., Jiang, J., Ai, Y., Wang, E., Han, S., & Rong, S. (2015). A new application of oily cold rolling mill sludge for preparing Fe_2O_3/graphene as anodes for lithium-ion batteries. *RSC Advances, 5*(71), 57383-57388.

Liu, T., Wang, L., Lu, X., Fan, J., Cai, X., Gao, B., Miao, R., Wang, J., & Lv, Y. (2017). Comparative study of the photocatalytic performance for the degradation of different dyes by $ZnIn_2S_4$: Adsorption, active species, and pathways. *RSC Advances, 7*(20), 12292-12300.

Loh, K. P., Bao, Q., Eda, G., & Chhowalla, M. (2010). Graphene oxide as a chemically tunable platform for optical applications. *Nature Chemistry, 2*(12), 1015.

Loryuenyong, V., Totepvimarn, K., Eimburanapravat, P., Boonchompoo, W., & Buasri, A. (2013). Preparation and characterization of reduced graphene oxide sheets via water-based exfoliation and reduction methods. *Advances in Materials Science and Engineering, 2013*, 923403.

Lu, C.-S., Chen, C.-C., Huang, L.-K., Tsai, P.-A., & Lai, H.-F. (2013). Photocatalytic degradation of acridine orange over $NaBiO_3$ driven by visible light irradiation. *Catalysts, 3*(2), 501-516.

Lu, G., Yu, K., Wen, Z., & Chen, J. (2013). Semiconducting graphene: Converting graphene from semimetal to semiconductor. *Nanoscale, 5*(4), 1353-1368.

Luo, D., Zhang, G., Liu, J., & Sun, X. (2011). Evaluation criteria for reduced graphene oxide. *The Journal of Physical Chemistry C, 115*(23), 11327-11335.

Luque, F., Huizenga, J., Crespo-Feo, E., Wada, H., Ortega, L., & Barrenechea, J. (2014). Vein graphite deposits: Geological settings, origin, and economic significance. *Mineralium Deposita, 49*(2), 261-277.

Ma, C. M., Lin, Y. J., Shiue, R. W., & Chang, C. T. (2013). Dyes degradation with Fe-doped titanium nanotube photocatalysts prepared from spend steel slag. *International Journal of Photoenergy, 2013*, 350698.

Mahmoodi, N. M., Maroofi, S. M., Mazarji, M., & Nabi-Bidhendi, G. (2017). Preparation of modified reduced graphene oxide nanosheet with cationic surfactant and its dye adsorption ability from colored wastewater. *Journal of Surfactants and Detergents, 20*(5), 1085-1093.

Mansur, A. A., Mansur, H. S., Ramanery, F. P., Oliveira, L. C., & Souza, P. P. (2014). "Green" colloidal ZnS quantum dots/chitosan nano-photocatalysts for advanced oxidation processes: Study of the photodegradation of organic dye pollutants. *Applied Catalysis B: Environmental, 158-159*, 269-279.

Marichy, C., Russo, P. A., Latino, M., Tessonnier, J.-P., Willinger, M.-G., Donato, N., Neri, G., & Pinna, N. (2013). Tin dioxide–carbon heterostructures applied to gas sensing: Structure-dependent properties and general sensing mechanism. *The Journal of Physical Chemistry C, 117*(38), 19729-19739.

Matsumoto, Y., Koinuma, M., Ida, S., Hayami, S., Taniguchi, T., Hatakeyama, K., Tateishi, H., Watanabe, Y., & Amano, S. (2011). Photoreaction of graphene oxide nanosheets in water. *The Journal of Physical Chemistry C, 115*(39), 19280-19286.

Minitha, C., Lalitha, M., Jeyachandran, Y., & Senthilkumar, L. (2017). Adsorption behaviour of reduced graphene oxide towards cationic and anionic dyes: Co-action of electrostatic and π–π interactions. *Materials Chemistry and Physics, 194*, 243-252.

Mitrogiannis, D., Markou, G., Çelekli, A., & Bozkurt, H. (2015). Biosorption of methylene blue onto *Arthrospira platensis* biomass: Kinetic, equilibrium and thermodynamic studies. *Journal of Environmental Chemical Engineering, 3*(2), 670-680.

Mohamed, A., El-Sayed, R., Osman, T., Toprak, M., Muhammed, M., & Uheida, A. (2016). Composite nanofibers for highly efficient photocatalytic degradation of organic dyes from contaminated water. *Environmental Research, 145*, 18-25.

Mohamed, M. J. S., & Bhat, D. K. (2017). Novel $ZnWO_4$/RGO nanocomposite as high performance photocatalyst. *AIMS Materials Science, 4*(1), 158-171.

Moon, I. K., Lee, J., Ruoff, R. S., & Lee, H. (2010). Reduced graphene oxide by chemical graphitization. *Nature Communications, 1*, 73.

Moradi, B., & Botte, G. G. (2016). Recycling of graphite anodes for the next generation of lithium ion batteries. *Journal of Applied Electrochemistry, 46*(2), 123-148.

Morais, A., Longo, C., Araujo, J. R., Barroso, M., Durrant, J. R., & Nogueira, A. F. (2016). Nanocrystalline anatase TiO_2/reduced graphene oxide composite films as photoanodes for photoelectrochemical water splitting studies: The role of reduced graphene oxide. *Physical Chemistry Chemical Physics, 18*(4), 2608-2616.

Morimoto, N., Kubo, T., & Nishina, Y. (2016). Tailoring the oxygen content of graphite and reduced graphene oxide for specific applications. *Scientific Reports, 6*, 21715.

Moussa, H., Girot, E., Mozet, K., Alem, H., Medjahdi, G., & Schneider, R. (2016). ZnO rods/reduced graphene oxide composites prepared via a solvothermal reaction for efficient sunlight-driven photocatalysis. *Applied Catalysis B, 185*, 11-21.

Mukhopadhyay, P., & Gupta, R. K. (2012). *Graphite, Graphene, and Their Polymer Nanocomposites*. Boca Raton: CRC Press.

Naeem, H., Ajmal, M., Muntha, S., Ambreen, J., & Siddiq, M. (2018). Synthesis and characterization of graphene oxide sheets integrated with gold nanoparticles and their applications to adsorptive removal and catalytic reduction of water contaminants. *RSC Advances, 8*(7), 3599-3610.

Nasir, A., Kausar, A., & Younus, A. (2015). Polymer/graphite nanocomposites: Physical features, fabrication and current relevance. *Polymer-Plastics Technology and Engineering, 54*(7), 750-770.

Nasuha, N., Hameed, B., & Din, A. T. M. (2010). Rejected tea as a potential low-cost adsorbent for the removal of methylene blue. *Journal of Hazardous Materials, 175*(1-3), 126-132.

Nejdl, L., Zelnickova, J., Vaneckova, T., Hynek, D., Adam, V., & Vaculovicova, M. (2018). Rapid preparation of self-assembled CdTe quantum dots used for sensing of DNA in urine. *New Journal of Chemistry, 42*(8), 6005-6012.

Nupearachchi, C., Mahatantila, K., & Vithanage, M. (2017). Application of graphene for decontamination of water; Implications for sorptive removal. *Groundwater for Sustainable Development, 5*, 206-215.

Ossonon, B. D., & Bélanger, D. (2017). Synthesis and characterization of sulfophenyl-functionalized reduced graphene oxide sheets. *RSC Advances, 7*(44), 27224-27234.

Oxtoby, D. W., Gillis, H. P., & Butler, L. J. (2015). *Principles of Modern Chemistry* (8th ed.). Mason: Cengage Learning.

Oz, M., Lorke, D. E., & Petroianu, G. A. (2009). Methylene blue and Alzheimer's disease. *Biochemical Pharmacology, 78*(8), 927-932.

Park, S., An, J., Potts, J. R., Velamakanni, A., Murali, S., & Ruoff, R. S. (2011). Hydrazine-reduction of graphite-and graphene oxide. *Carbon, 49*(9), 3019-3023.

Pavia, D. L., Lampman, G. M., Kriz, G. S., & Vyvyan, J. A. (2014). *Introduction to Spectroscopy* (5th ed.). Mason: Cengage Learning.

Pavoski, G., Maraschin, T., Fim, F. d. C., Balzaretti, N. M., Galland, G. B., Moura, C. S., & Basso, N. R. d. S. (2017). Few layer reduced graphene oxide: Evaluation of the best experimental conditions for easy production. *Materials Research, 20*(1), 53-61.

Pham, V. H., Cuong, T. V., Hur, S. H., Shin, E. W., Kim, J. S., Chung, J. S., & Kim, E. J. (2010). Fast and simple fabrication of a large transparent chemically-converted graphene film by spray-coating. *Carbon, 48*(7), 1945-1951.

Phukan, P., Narzary, R., & Sahu, P. P. (2019). A green approach to fast synthesis of reduced graphene oxide using alcohol for tuning semiconductor property. *Materials Science in Semiconductor Processing, 104*, 104670.

Rafatullah, M., Sulaiman, O., Hashim, R., & Ahmad, A. (2010). Adsorption of methylene blue on low-cost adsorbents: A review. *Journal of Hazardous Materials, 177*(1-3), 70-80.

Rajamanickam, D., & Shanthi, M. (2016). Photocatalytic degradation of an organic pollutant by zinc oxide–solar process. *Arabian Journal of Chemistry, 9*, S1858-S1868.

Ramesha, G., Kumara, A. V., Muralidhara, H., & Sampath, S. (2011). Graphene and graphene oxide as effective adsorbents toward anionic and cationic dyes. *Journal of Colloid and Interface Science, 361*(1), 270-277.

Rao, A. N., Sivasankar, B., & Sadasivam, V. (2009). Kinetic studies on the photocatalytic degradation of Direct Yellow 12 in the presence of ZnO catalyst. *Journal of Molecular Catalysis A: Chemical, 306*(1-2), 77-81.

Rauf, M., & Ashraf, S. S. (2009). Radiation induced degradation of dyes—an overview. *Journal of Hazardous Materials, 166*(1), 6-16.

Rauf, M., Meetani, M., & Hisaindee, S. (2011). An overview on the photocatalytic degradation of azo dyes in the presence of TiO_2 doped with selective transition metals. *Desalination, 276*(1-3), 13-27.

Raza, H. (2012). *Graphene Nanoelectronics: Metrology, Synthesis, Properties and Applications*. Berlin: Springer.

Rowley-Neale, S. J., Randviir, E. P., Dena, A. S. A., & Banks, C. E. (2017). An overview of recent applications of reduced graphene oxide as a basis of electroanalytical sensing platforms. *Applied Materials Today, 10*, 218-226.

Saha, P. (2010). Assessment on the removal of methylene blue dye using tamarind fruit shell as biosorbent. *Water, Air, & Soil Pollution, 213*(1-4), 287-299.

Sahraei, R., Hemmati, K., & Ghaemy, M. (2016). Adsorptive removal of toxic metals and cationic dyes by magnetic adsorbent based on functionalized graphene oxide from water. *RSC Advances, 6*(76), 72487-72499.

Samsudin, E. M., Goh, S. N., Wu, T. Y., Ling, T. T., Abd, S., & Juan, J. (2015). Evaluation on the photocatalytic degradation activity of Reactive Blue 4 using pure anatase nano-TiO_2. *Sains Malaysiana, 44*(7), 1011-1019.

Sandoval, A., Hernández-Ventura, C., & Klimova, T. E. (2017). Titanate nanotubes for removal of methylene blue dye by combined adsorption and photocatalysis. *Fuel, 198*, 22-30.

Saxena, S., Tyson, T. A., Shukla, S., Negusse, E., Chen, H., & Bai, J. (2011). Investigation of structural and electronic properties of graphene oxide. *Applied Physics Letters, 99*(1), 013104.

Seddigi, Z. S. (2010). Removal of alizarin yellow dye from water using zinc doped WO_3 catalyst. *Bulletin of Environmental Contamination and Toxicology, 84*(5), 564-567.

Schirmer, R. H., Adler, H., Pickhardt, M., & Mandelkow, E. (2011). "Lest we forget you—methylene blue…". *Neurobiology of Aging, 32*(12), 2325.e2327-2325.e2316.

Shanmugam, M., Alsalme, A., Alghamdi, A., & Jayavel, R. (2015). Enhanced photocatalytic performance of the graphene-V_2O_5 nanocomposite in the degradation of methylene blue dye under direct sunlight. *ACS Applied Materials & Interfaces, 7*(27), 14905-14911.

Sharma, P., Hussain, N., Borah, D. J., & Das, M. R. (2013). Kinetics and adsorption behavior of the methyl blue at the graphene oxide/reduced graphene oxide nanosheet–water interface: A comparative study. *Journal of Chemical & Engineering Data, 58*(12), 3477-3488.

Sharma, R., Bansal, S., & Singhal, S. (2015). Tailoring the photo-Fenton activity of spinel ferrites (MFe_2O_4) by incorporating different cations (M = Cu, Zn, Ni and Co) in the structure. *RSC Advances, 5*(8), 6006-6018.

Sheng, J., Xie, Y., & Zhou, Y. (2009). Adsorption of methylene blue from aqueous solution on pyrophyllite. *Applied Clay Science, 46*(4), 422-424.

Soares, C. P. P., Baptista, R. d. L., & Cesar, D. V. (2017). Solvothermal reduction of graphite oxide using alcohols. *Materials Research, 21*(1), e20170726.

Some, S., Kim, Y., Yoon, Y., Yoo, H., Lee, S., Park, Y., & Lee, H. (2013). High-quality reduced graphene oxide by a dual-function chemical reduction and healing process. *Scientific Reports, 3*, 1929.

Srinivas, G., Burress, J., & Yildirim, T. (2012). Graphene oxide derived carbons (GODCs): Synthesis and gas adsorption properties. *Energy & Environmental Science, 5*(4), 6453-6459.

Stobinski, L., Lesiak, B., Malolepszy, A., Mazurkiewicz, M., Mierzwa, B., Zemek, J., Jiricek, P., & Bieloshapka, I. (2014). Graphene oxide and reduced graphene oxide studied by the XRD, TEM and electron spectroscopy methods. *Journal of Electron Spectroscopy and Related Phenomena, 195*, 145-154.

Su, H., Zhang, C., Li, X., Wu, L., & Chen, Y. (2018). Aggregation prevention: Reduction of graphene oxide in mixed medium of alkylphenol polyoxyethylene (7) ether and 2-methoxyethanol. *RSC Advances, 8*(68), 39140-39148.

Sun, J.-Z., Liao, Z.-H., Si, R.-W., Kingori, G. P., Chang, F.-X., Gao, L., Shen, Y., Xiao, X., Wu, X.-Y., & Yong, Y.-C. (2014). Adsorption and removal of triphenylmethane dyes from water by magnetic reduced graphene oxide. *Water Science and Technology, 70*(10), 1663-1669.

Tai, X. H., Chook, S. W., Lai, C. W., Lee, K. M., Yang, T. C. K., Chong, S., & Juan, J. C. (2019). Effective photoreduction of graphene oxide for photodegradation of volatile organic compounds. *RSC Advances, 9*(31), 18076-18086.

Tan, S. M., Ambrosi, A., Chua, C. K., & Pumera, M. (2014). Electron transfer properties of chemically reduced graphene materials with different oxygen contents. *Journal of Materials Chemistry A, 2*(27), 10668-10675.

Thakur, M., Sharma, G., Ahamad, T., Ghfar, A. A., Pathania, D., & Naushad, M. (2017). Efficient photocatalytic degradation of toxic dyes from aqueous environment using gelatin-Zr(IV) phosphate nanocomposite and its antimicrobial activity. *Colloids and Surfaces B, 157*, 456-463.

Thangavel, S., & Venugopal, G. (2014). Understanding the adsorption property of graphene-oxide with different degrees of oxidation levels. *Powder Technology, 257*, 141-148.

Thommes, M., Kaneko, K., Neimark, A. V., Olivier, J. P., Rodriguez-Reinoso, F., Rouquerol, J., & Sing, K. S. (2015). Physisorption of gases, with special reference to the evaluation of surface area and pore size distribution (IUPAC Technical Report). *Pure and Applied Chemistry, 87*(9-10), 1051-1069.

Tiwari, A., Mishra, Y. K., Kobayashi, H., & Turner, A. P. (2017). *Intelligent Nanomaterials* (2nd ed.). Beverly: Scrivener Publishing.

Tiwari, A., & Syväjärvi, M. (2016). *Advanced 2D Materials*. Beverly: Scrivener Publishing.

Tiwari, J. N., Mahesh, K., Le, N. H., Kemp, K. C., Timilsina, R., Tiwari, R. N., & Kim, K. S. (2013). Reduced graphene oxide-based hydrogels for the efficient capture of dye pollutants from aqueous solutions. *Carbon, 56*, 173-182.

Tofighy, M. A., & Mohammadi, T. (2011). Adsorption of divalent heavy metal ions from water using carbon nanotube sheets. *Journal of Hazardous Materials, 185*(1), 140-147.

Tong, H., Ouyang, S., Bi, Y., Umezawa, N., Oshikiri, M., & Ye, J. (2012). Nano-photocatalytic materials: Possibilities and challenges. *Advanced Materials, 24*(2), 229-251.

Vandenabeele, P. (2013). *Practical Raman Spectroscopy: An Introduction*. Hoboken: John Wiley & Sons.

Wang, C.-C., Li, J.-R., Lv, X.-L., Zhang, Y.-Q., & Guo, G. (2014). Photocatalytic organic pollutants degradation in metal–organic frameworks. *Energy & Environmental Science, 7*(9), 2831-2867.

Wang, F., Haftka, J. J.-H., Sinnige, T. L., Hermens, J. L., & Chen, W. (2014). Adsorption of polar, nonpolar, and substituted aromatics to colloidal graphene oxide nanoparticles. *Environmental Pollution, 186*, 226-233.

Wang, J., Chen, B., & Xing, B. (2016). Wrinkles and folds of activated graphene nanosheets as fast and efficient adsorptive sites for hydrophobic organic contaminants. *Environmental Science & Technology, 50*(7), 3798-3808.

Wang, J., Chen, Z., & Chen, B. (2014). Adsorption of polycyclic aromatic hydrocarbons by graphene and graphene oxide nanosheets. *Environmental Science & Technology, 48*(9), 4817-4825.

Wang, J., Mu, X., & Sun, M. (2019). The thermal, electrical and thermoelectric properties of graphene nanomaterials. *Nanomaterials, 9*(2), 218.

Wang, J., Salihi, E. C., & Šiller, L. (2017). Green reduction of graphene oxide using alanine. *Materials Science and Engineering: C, 72*, 1-6.

Wang, S., Dong, Y., He, C., Gao, Y., Jia, N., Chen, Z., & Song, W. (2017). The role of sp^2/sp^3 hybrid carbon regulation in the nonlinear optical properties of graphene oxide materials. *RSC Advances, 7*(84), 53643-53652.

Wong, C. P. P., Lai, C. W., Lee, K. M., & Hamid, S. B. A. (2015). Advanced chemical reduction of reduced graphene oxide and its photocatalytic activity in degrading Reactive Black 5. *Materials, 8*(10), 7118-7128.

Wu, C. (2017). *Inorganic Two-dimensional Nanomaterials: Fundamental Understanding, Characterizations and Energy Applications*. Cambridge: Royal Society of Chemistry.

Xiang, Q., Yu, J., & Jaroniec, M. (2012). Graphene-based semiconductor photocatalysts. *Chemical Society Reviews, 41*(2), 782-796.

Xu, S., Fu, L., Pham, T. S. H., Yu, A., Han, F., & Chen, L. (2015). Preparation of ZnO flower/reduced graphene oxide composite with enhanced photocatalytic performance under sunlight. *Ceramics International, 41*(3), 4007-4013.

Xu, S., Yong, L., & Wu, P. (2013). One-pot, green, rapid synthesis of flowerlike gold nanoparticles/reduced graphene oxide composite with regenerated silk fibroin as efficient oxygen reduction electrocatalysts. *ACS Applied Materials & Interfaces, 5*(3), 654-662.

Xue, B., & Zou, Y. (2018). High photocatalytic activity of ZnO–graphene composite. *Journal of Colloid and Interface Science, 529*, 306-313.

Yeh, T.-F., Chan, F.-F., Hsieh, C.-T., & Teng, H. (2011). Graphite oxide with different oxygenated levels for hydrogen and oxygen production from water under illumination: The band positions of graphite oxide. *The Journal of Physical Chemistry C, 115*(45), 22587-22597.

Yeh, T. F., Syu, J. M., Cheng, C., Chang, T. H., & Teng, H. (2010). Graphite oxide as a photocatalyst for hydrogen production from water. *Advanced Functional Materials, 20*(14), 2255-2262.

Yu, L., Wang, L., Xu, W., Chen, L., Fu, M., Wu, J., & Ye, D. (2018). Adsorption of VOCs on reduced graphene oxide. *Journal of Environmental Sciences, 67*, 171-178.

Zarrabi, M., Haghighi, M., Alizadeh, R., & Mahboob, S. (2019). Solar-light-driven photodegradation of organic dyes on sono-dispersed ZnO nanoparticles over graphene oxide: Sono vs. conventional catalyst design. *Separation and Purification Technology, 211*, 738-752.

Zhang, M., Yao, Q., Lu, C., Li, Z., & Wang, W. (2014). Layered double hydroxide–carbon dot composite: High-performance adsorbent for removal of anionic organic dye. *ACS Applied Materials & Interfaces, 6*(22), 20225-20233.

Zhang, Q., Zheng, H., Geng, Z., Jiang, S., Ge, J., Fan, K., Duan, S., Chen, Y., Wang, X., & Luo, Y. (2013). The realistic domain structure of as-synthesized graphene oxide from ultrafast spectroscopy. *Journal of the American Chemical Society, 135*(33), 12468-12474.

Zhang, T., Wang, X., & Zhang, X. (2014). Recent progress in TiO_2-mediated solar photocatalysis for industrial wastewater treatment. *International Journal of Photoenergy, 2014*, 607954.

Zhao, B., Liu, P., Jiang, Y., Pan, D., Tao, H., Song, J., Fang, T., & Xu, W. (2012). Supercapacitor performances of thermally reduced graphene oxide. *Journal of Power Sources, 198*, 423-427.

Zhao, C., Wang, Q., Zhang, H., Passerini, S., & Qian, X. (2016). Two-dimensional titanium carbide/RGO composite for high-performance supercapacitors. *ACS Applied Materials & Interfaces, 8*(24), 15661-15667.

Zhao, G., Ren, X., Gao, X., Tan, X., Li, J., Chen, C., Huang, Y., & Wang, X. (2011). Removal of Pb(II) ions from aqueous solutions on few-layered graphene oxide nanosheets. *Dalton Transactions, 40*(41), 10945-10952.

Zhao, Y., Wei, X., Wang, Y., & Luo, F. (2014). One-pot twelve tungsten phosphate acid assisted electrochemical synthesis of WO_3-decorated graphene sheets for high-efficiency UV-light-driven photocatalysis. *Chemical Physics Letters, 607*, 34-38.

Zheng, F., Xu, W.-L., Jin, H.-D., Hao, X.-T., & Ghiggino, K. P. (2015). Charge transfer from poly (3-hexylthiophene) to graphene oxide and reduced graphene oxide. *RSC Advances, 5*(109), 89515-89520.

Zhou, Y., Apul, O. G., & Karanfil, T. (2015). Adsorption of halogenated aliphatic contaminants by graphene nanomaterials. *Water Research, 79*, 57-67.

Zhu, H., Fu, Y., Jiang, R., Yao, J., Liu, L., Chen, Y., Xiao, L., & Zeng, G. (2013). Preparation, characterization and adsorption properties of chitosan modified magnetic graphitized multi-walled carbon nanotubes for highly effective removal of a carcinogenic dye from aqueous solution. *Applied Surface Science, 285*, 865-873.

LIST OF PUBLICATION AND PAPER PRESENTED

ISI-Cited Publication:

1. Siong, V. L. E., Lai, C. W., Juan, J. C., Lee, K. M., Leo, B. F., & Khe, C. S. (2019). One-step solvothermal synthesis of rGO/TiO_2 nanocomposite for efficient solar photocatalytic degradation of methylene blue dye. *Current Nanoscience*, *15*(2), 157-162.
2. Siong, V. L. E., Lee, K. M., Juan, J. C., Lai, C. W., Tai, X. H., & Khe, C. S. (2019). Removal of methylene blue dye by solvothermally reduced graphene oxide: A metal-free adsorption and photodegradation method. *RSC Advances*, *9*(64), 37686-37695.

Conference Proceeding:

1. Siong, V. L. E., Lai, C. W., Juan, J. C., Lee, K. M., Leo, B. F., & Khe, C. S. (2017). One-step solvothermal synthesis of rGO/TiO_2 nanocomposite for efficient solar photocatalytic degradation of methylene blue dye. 3rd International Conference on the Science and Engineering of Materials (ICoSEM 2017), 24-25th October 2017, Kuala Lumpur, Malaysia.